University of Alberta

Library Release Form

Name of Author: Mark D'Andrea

Title of Thesis: Behaviour and Rehabilitation of Distortion-Induced Fatigue Cracks in Bridge Girders

Degree: Master of Science

Year this Degree Granted: Fall 2001

Permission is hereby granted to the University of Alberta Library to reproduce single copies of this thesis and to lend or sell copies for private, scholarly or scientific research purposes only.

The author reserves all other publication and other rights in association with the copyright in the thesis, and except as herein before provided, neither the thesis nor any substantial portion thereof may be printed or otherwise reproduced in any material form whatever without the author's prior written permission.

University of Alberta

Behaviour and Rehabilitation of Distortion-Induced Fatigue Cracks in Bridge Girders

by

Mark D'Andrea ©

A thesis submitted to the Faculty of Graduate Studies and Research in partial fulfillment of the requirements for the degree of Master of Science

in

Structural Engineering

Department of Civil and Environmental Engineering

Edmonton, Alberta

Fall 2001

University of Alberta

Faculty of Graduate Studies and Research

The undersigned certify that they have read, and recommend to the Faculty of Graduate Studies and Research for acceptance, a thesis entitled Behaviour and Rehabilitation of Distortion-Induced Fatigue Cracks in Bridge Girders submitted by Mark D'Andrea in partial fulfillment of the requirements for the degree of Master of Science in Structural Engineering.

ABSTRACT

In many multi-girder bridges distortion-induced fatigue cracking is prevalent in the web gap region of the diaphragm-to-girder connection. CN Railway made available girders from such a bridge, which had over 300 distortion-induced fatigue cracks, for laboratory testing.

Fatigue and fracture tests were performed to assess the behaviour of the fatigue cracks and to assess the effectiveness of rehabilitations. The combination of drilled stop holes and an angle bolted to the transverse stiffener and the tension flange was found to be an effective rehabilitation if performed once the fatigue cracks were detected.

In addition to the experimental program, a finite element analysis was performed to investigate the stresses in the web gap region. Results from the analysis showed that the designation of the web gap detail as a fatigue Category C' detail results in a conservative prediction of the fatigue life.

ACKNOWLEDGEMENTS

TABLE OF CONTENTS

LIST OF TABLES

LIST OF FIGURES

LIST OF SYMBOLS

A_r = half the equivalent crack length after rehabilitation

E = modulus of elasticity

I = moment of inertia

L = length of web gap

M = bending moment

t = web thickness

y = distance from neutral axis to extreme fibre

Δ = web gap distortion

ΔK = stress intensity factor range

$\Delta \sigma$ = nominal stress range

ρ = radius of the drilled stop hole

σ = maximum bending stress

σ_y = yield strength of the material

1. INTRODUCTION

1.1 General Background

Lateral load distribution in multi-girder bridges is achieved by means of diaphragm members connected to the girders through welded transverse stiffeners. In the past it was common practice for transverse stiffeners to be cut short of the flanges in order to facilitate fabrication, thus leaving a gap between the end of the stiffener and the flange. Also, it was considered to be poor practice to connect the stiffeners to the flanges. The distortions resulting in the web gap due to the racking motion of diaphragms quickly initiated fatigue cracks in the web of girders at the weld between the stiffeners and the web. These distortion-induced fatigue cracks are prevalent in skewed bridges that have staggered diaphragms.

The St. Albert Trail Mile 5.09 Edson Subdivision Bridge, which carries CN main line traffic over the St. Albert Trail in Edmonton, Alberta, is a multi-girder skewed bridge with staggered diaphragms. Figures 1–1 and 1–2 show a plan view and a typical section of the bridge structure. The CN Mile 5.09 Edson Subdivision Bridge, constructed in 1965, is comprised of two parallel four span bridges with two end spans of 9.9 m and two middle spans of 17.3 m. Each bridge has eight parallel steel girders interconnected by staggered steel diaphragms and is composite with a 268 mm thick concrete deck. The bridge is on a 28° RHF skew, but the diaphragms are perpendicular to the bridge girders. Therefore, the diaphragms are not continuous at a given location across the width of the bridge. The diaphragm members are connected to the girder through transverse stiffeners that are welded to the girder web and top flange, but cut 51 mm short of the top surface of the bottom flange.

Rehabilitation of the bridge was undertaken in 1985 in order to repair the girders that were damaged from impact of road traffic passing under the bridge and to arrest the growth of fatigue cracks that had initiated in the girder web gaps. In an attempt to halt the fatigue cracks, 24 mm stop holes were drilled at the crack tips to relieve the high stress concentrations present at the crack tips. By 1998 routine inspections had found over 300 web cracks near the base of the transverse stiffeners, including some cracks that

extended beyond the drilled stop holes. Because of the large number of fatigue cracks and the substandard clearance between the roadway and the underside of the bridge, the total superstructure of the bridge was replaced in August 1998.

Prior to removal of the bridge, field testing was performed to measure the deflections and strains in one set of the 9.9 m end spans under the north-east structure (see Figure 1–1). Two CN Rail EF–644a locomotives were used to conduct both static and dynamic tests. At the time of dismantling, the University of Alberta obtained four sets of three girders, from the 9.9 m north spans. The concrete slab and the fascia girder were removed from each set in order to reduce the weight of the specimens for shipping. The field test results were used to design an experimental test setup by Fraser *et al.* (2000) that reproduced the in-situ midspan bottom fibre stress range and the in-situ racking motion at each of the diaphragms of the most heavily loaded girder. The testing program performed by Fraser *et al.* (2000) consisted of fatigue testing of three girders to assess the behaviour of the distortion-induced fatigue cracks in the web gap region. Low temperature tests were also performed to determine the stability of the fatigue cracks at sub-zero temperatures.

1.2 Objectives

The research presented in the following is intended to add to the experimental program conducted by Fraser *et al.* (2000) on the behaviour of distortion-induced fatigue cracks and to assess various distortion induced fatigue crack repair strategies. The investigation described in the following includes an experimental and numerical analysis program. The objectives of the investigation are to:

1. Study the behaviour of the distortion-induced fatigue cracks in four of the girders obtained from the bridge;

2. Expand the database of test results with test specimens loaded at a level 40% larger than that observed in the field and compare with results obtained from the testing program performed by Fraser *et al.* (2000);

3. Confirm the stability of distortion-induced fatigue cracks at -50°C;

4. Determine the effectiveness of repair angles, connecting the transverse stiffener to the girder bottom flange and connecting the girder web to the girder bottom flange, as a rehabilitation for distortion-induced fatigue cracks;

5. Develop and validate finite element models of the tested full-scale test specimens;

6. Analyse the behaviour of the web gap region, including the effect of bottom flange thickness, and the length of the web gap.

1.3 Scope of Research

The research program presented in the following was limited in scope as follows:

1. Four of five test specimens were tested at a bottom fibre stress range of 50 MPa;

2. Three of those four test specimens were repaired after fatigue cracks had propagated to a significant length;

3. The fifth test specimen was repaired prior to testing and then tested at a bottom fibre stress range of 35 MPa;

4. Finite element analysis was performed to investigate the behaviour of the web gap region.
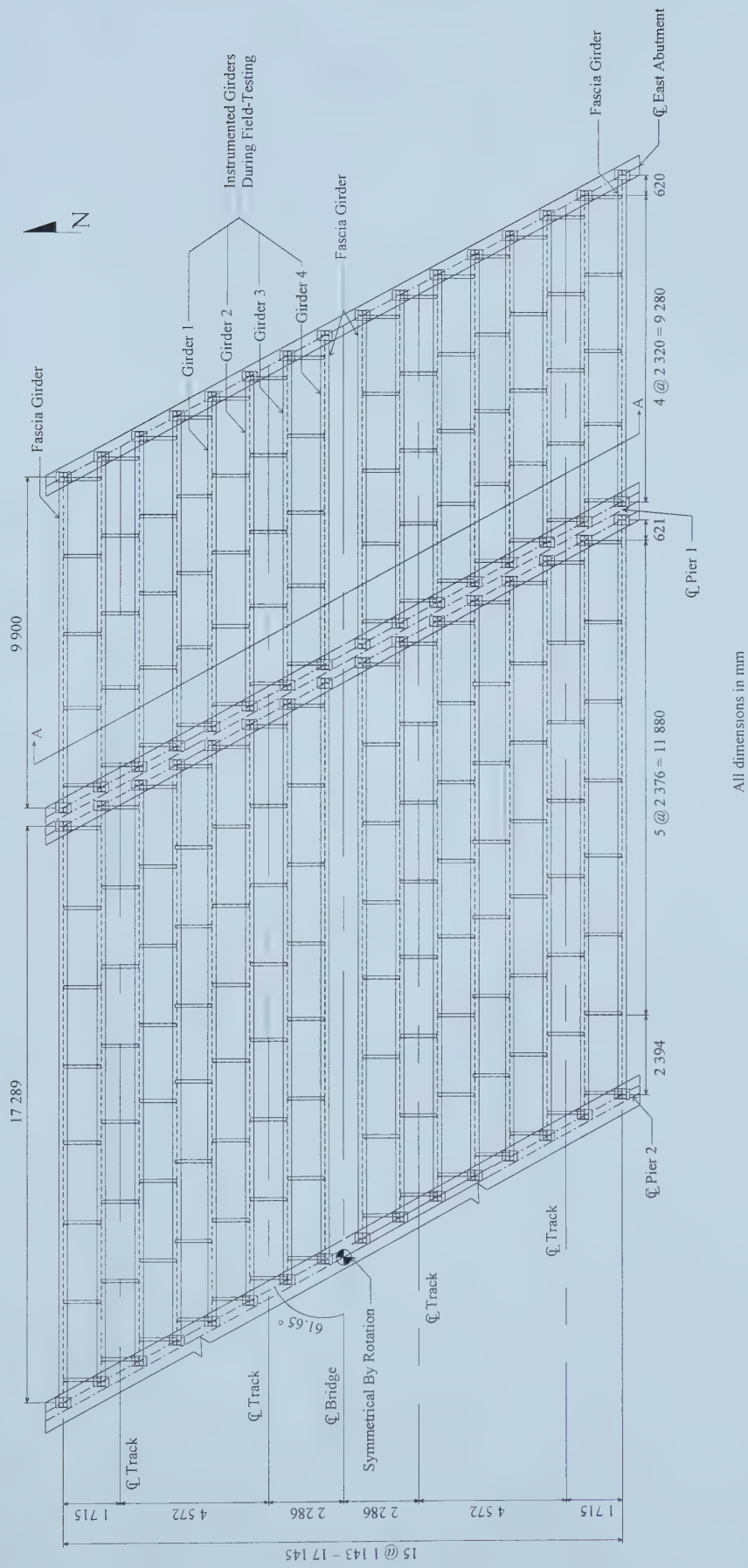
Figure 1–1 Plan View of CN Mile 5.09 Edson Subdivision Bridge (Fraser *et al.*, 2000)

4

Figure 1–2 Typical Cross-Section of CN Mile 5.09 Edson Subdivision Bridge (Fraser *et al.*, 2000)

5

2. LITERATURE REVIEW

2.1 General

Research undertaken in this investigation is focused on two aspects of distortion-induced fatigue of steel bridge girders. The first involves the behaviour of the distortion-induced fatigue cracks that develop in the web gap region. The second aspect involves the effectiveness of possible rehabilitation schemes to arrest distortion-induced fatigue cracking.

A summary of the review provided by Fraser *et al.* (2000) is presented following, with emphasis on the behaviour of distortion-induced fatigue cracks and on rehabilitation schemes. Additional review of research investigating Mode III (tearing mode) fatigue crack propagation is also presented. The experimental program undertaken in this study is an extension of the experiments performed by Fraser *et al.* (2000). Therefore, a review of that research program is presented herein.

2.2 Behaviour of Distortion-Induced Fatigue Cracks in Bridge Girders

In multigirder bridges, diaphragm members are usually connected to the girders using transverse connection stiffeners welded to the web of the girder. Diaphragms are necessary to brace the girders during construction, to aid in the transfer of lateral loads such as wind and earthquake in the completed structure and, to some extent, to distribute live loads among the girders. Prior to the 1983 American Association of State Highway and Transportation Officials (AASHTO) Bridge Specifications (AASHTO, 1983), the transverse stiffeners were often cut short of the girder tension flange to facilitate fitting during fabrication and to avoid a possible fatigue-prone detail resulting from welding the transverse stiffeners to the tension flange. Subsequently, experience has shown that the fatigue life of this detail is independent of whether the stiffener terminates in the web or is extended down to the flange (Fisher *et al.*, 1998). There are many bridges still in service that have transverse stiffeners connected to diaphragms that are not connected to both flanges.

As observed by Fisher and Keating (1989), fatigue cracks resulting from deformations out of the plane of the girder web are common in webs where the gap between the end of the stiffener and the top surface of the tension flange is short. Under live loads, the differential displacement between adjacent girders causes a racking motion in the diaphragms, resulting in a deformation in the flexible web gap location. In the out-of-plane direction, the web gap region is flexible as compared to the region of the web where the transverse stiffener is attached. Figure 2–1 shows the typical deformation at a web gap location due to a differential displacement. Skewed bridges with staggered diaphragms are greatly affected by the differential displacement since the diaphragms are placed on only one side of the girder web at a given location.

Strain measurements taken in the field by Fisher (1978) indicated that the web gap is subjected to double curvature. This was confirmed by Fisher and Keating (1989) and Fraser *et al.* (2000). The deformed shape of the web gap can be approximated as a fix-ended beam subjected to a transverse support displacement, as shown in Figure 2–2 (Fisher *et al.*, 1998). Using the moment-area theorems, the approximate maximum stress in the web gap, assuming a unit width of web, is given as

$$\sigma = \frac{M\,y}{I} = \frac{6\,E\,I\,\Delta}{L^2}\left(\frac{t}{2}\right)\left(\frac{1}{I}\right) = \frac{3\,E\,\Delta\,t}{L^2} \tag{2–1}$$

where: σ = maximum bending stress (*MPa*);

M = bending moment ($N \cdot mm$);

y = distance from neutral axis to extreme fibre (*mm*);

I = moment of inertia (*mm*^{4});

E = modulus of elasticity (*MPa*);

L = length of web gap (*mm*);

Δ = web gap distortion (*mm*);

t = web thickness (*mm*).

Fisher (1978) performed an investigation of distortion-induced fatigue cracking of longitudinal bridge girders at the connection of transverse beams. Distortion-induced fatigue cracks were observed in the negative moment regions and in the positive moment

regions, since transverse stiffeners in both regions were not connected to the tension flange. In the negative moment region the web gap was restrained by the top flange, which was embedded in the concrete slab, while in the positive moment region the web gap was restrained by the bottom flange. The measured stresses from web gap distortions in negative moment regions were larger than the stresses in the positive moment regions. Therefore the amount of lateral restraint to the tension flange seems to affect the web gap stresses, which demonstrates the difficulty in evaluating the maximum web gap stress.

Further complicating the calculation of the web gap stresses is the determination of the small web gap distortion. The magnitude of the distortion is difficult to determine since the true behaviour of the structure, which is dependent on the interaction of all the various components of the structure to the actual loading conditions, must be ascertained (Fisher, 1978). Even a small distortion can produce large stresses. For example, a distortion of only 0.004 mm can cause a significantly large stress of 128 MPa, based on a web thickness of 12 mm and a web gap length of 15 mm (Fisher *et al.*, 1998).

The large stresses that develop in the web gap region cause fatigue cracks to initiate in a relatively short time. These fatigue cracks usually extend across the weld toe at the end of the transverse stiffener and into the web as shown in Figure 2–3. Fisher (1978) investigated distortion-induced fatigue cracking at the ends of transverse stiffeners and found that some cracks propagated further into the web and then turned upwards, perpendicular to the primary stress field. Similar crack patterns were observed by Fraser *et al.* (2000).

The typical crack pattern, shown in Figure 2–3, and the out-of-plane deformation of the web gap, idealized in Figure 2–2, illustrate that fatigue cracks in web gaps are the result of the compound effect of Mode I (crack opening mode) and Mode III (tearing mode) (Fraser *et al.*, 2000). As the web gap deforms, the top surface of the crack will move further out-of-plane than the bottom surface of the crack. Figure 2–4 illustrates Mode I and Mode III crack movement. Under in-plane loading conditions alone, fatigue crack propagation occurs as Mode I.

A better understanding of Mode III fatigue crack propagation can be obtained by looking at the work of Gross (1985) and Tshegg and Stanzl (1988). Mode III loading causes the surfaces of a crack to rub against one another and this rubbing of the rough crack surfaces causes energy to be dissipated through friction and abrasion. The friction along the crack surfaces results in lower stresses at the crack tip than would otherwise be expected. The total amount of friction increases as the crack propagates, thereby decreasing the crack growth rate. Experiments performed by Tshegg and Stanzl (1988) showed that the crack growth rate for a specimen subjected to cyclic Mode III and static Mode I loading causes an increase in the crack growth rate compared to a specimen subjected to cyclic Mode III loading only. The decrease in crack growth rate as the crack propagates becomes much less significant when combined Mode III and Mode I loading occurs. Fraser *et al.* (2000) suggested that Mode III loading governed the crack propagation past the stop holes at distortion-induced fatigue cracks. However, the absence of a decrease in crack growth rate as the crack length increased suggests that the cracks were propagating as a result of combined Mode III and Mode I fatigue loading.

2.3 Current Design Practice

As mentioned previously, the AASHTO (1983) rules required that transverse stiffeners, which were connected to lateral bracing, be connected to both flanges. This requirement was partially based on the work of Fisher (1978), which included the investigation of cracking at the ends of transverse stiffeners cut short of the bottom flange of bridge girders. Current design standards AASHTO (1998) and Canadian Highway Bridge Design Code (CHBDC) (CSA, 2000) require the connection of transverse stiffeners to both the tension and compression flanges when the transverse stiffeners are used as connection plates for diaphragms, cross-frames or floor beams.

For bridges built with transverse stiffeners cut short of the tension flange, fatigue in the web gap was not considered when the bridge was designed. Therefore, the fatigue life of the web gap detail needs to be assessed. To determine the fatigue life of the web gap detail subjected to distortion-induced fatigue, current practice designates the detail as a Category C' detail (AASHTO, 1998) or Category C1 detail (CSA, 2000) (Fisher *et al.*,

1998). The description of the Category C' detail is fillet-welded connections (transverse stiffener-to-web welds) with welds normal to the direction of stress. The Category C' designation and the calculated stress range are then used with the S-N (stress range versus number of stress cycles) curve to determine the allowable number of stress cycles for the web gap detail. It should be noted that the S-N curve and the Category designations were developed for load-induced fatigue not distortion-induced fatigue.

2.4 Rehabilitation of Girders with Distortion-Induced Fatigue Cracks

Three of the most common rehabilitation techniques for distortion-induced fatigue cracking are: (1) drilling of stop holes at the crack tips; (2) increase of the web gap length; and (3) attachment of the transverse stiffener to the tension flange. Another rehabilitation is the removal of the diaphragms, but this is used only infrequently.

Drilling stop holes at the crack tip causes a reduction of the stress intensity at the tip of the crack because the sharp crack tip is replaced by a hole of finite radius. The ability of stop holes to arrest fatigue crack propagation due to in-plane loading conditions led to their use with distortion-induced fatigue cracks. However, the care required to ensure that the crack tip is removed limits the effectiveness of the repair, even for in-plane fatigue crack propagation. Also limiting the effectiveness is the reliability of the criterion commonly used for determining the size of the stop holes to arrest the fatigue cracks. As proposed by Fisher (1980), this is

$$\frac{\Delta K}{\sqrt{\rho}} = \frac{\Delta\sigma\sqrt{\pi\, A_r}}{\sqrt{\rho}} < 10.5\sqrt{\sigma_y} \qquad (2\text{--}2)$$

where: ΔK = stress intensity factor range;

ρ = radius of the drilled stop hole (*mm*);

A_r = half the equivalent crack length after rehabilitation (*mm*), as shown in Figure 2–5;

$\Delta\sigma$ = nominal stress range (*MPa*);

σ_y = yield strength of the material (*MPa*).

Lai (1997) performed a numerical analysis and found that Equation 2–2 would give non-conservative results for the true stress concentration factor when crack lengths are large. Lai also suggested that the deformation at the edge of the stop holes due to the out-of-plane web distortion results from Mode III fatigue. He suggested that Equation 2–2 is not valid for fatigue cracks initiated by out-of-plane web distortions since the equation considers only Mode I loading. The observation of crack re-initiation past stop holes in the experimental program performed by Fraser et al. (2000) confirms this observation. Fisher and Keating (1989) also found that distortion-induced fatigue cracks were difficult to arrest using stop holes alone. It appears that drilling of stop holes should be considered a temporary measure and should be used in conjunction with another rehabilitation to arrest distortion-induced fatigue crack growth.

A numerical investigation of web gap distortions in multigirder steel bridges by Castiglioni *et al.* (1998) showed that the doubling of the web gap length from 50 mm to 100 mm did not significantly change the amount of web gap distortion. Hence, an increase in web gap length can reduce the web gap stresses but does not affect the magnitude of the out-of-plane web distortion. This suggests that an increase in web gap length could be helpful to decrease the distortions that cause the distortion-induced fatigue cracks.

Although both of these rehabilitation schemes attempt to decrease the stresses in the web gap region, they do not affect the root cause of the stresses—the web gap distortion. One way to reduce the distortion would be to use an angle to connect the transverse stiffener to the tension flange. Although welding of the angle may be convenient for this renovation, it is preferable that the angle be bolted to both the stiffener and the flange. As discussed by Fisher and Keating (1989), welded repairs have not been successful in some cases because, under field conditions, the weld quality is likely to be less than ideal. The connection of the transverse stiffener to the tension flange eliminates the abrupt change in out-of-plane stiffness at the web gap.

Eliminating the distortion-induced fatigue stresses could also be achieved by removing the diaphragms (Stallings *et al.*, 1999). Using the results of field tests, these researchers

concluded that the live load distribution in a 76 m, three-span, continuous steel girder bridge was not significantly affected by the removal of the interior diaphragms. However, the removal of diaphragms affects other factors that would have to be investigated. These factors include the lateral loads that would now have to be transferred by the concrete slab only, the increase in differential displacements that would increase the transverse slab moments, and lateral bracing of the girders that would be required if the concrete slab ever needed to be replaced. Stallings *et al.* (1999) also recommended that stop holes be drilled at fatigue cracks to eliminate any further growth from in-plane stresses.

2.5 Summary of Work Reviewed

Further investigation of fatigue cracks at the ends of transverse stiffeners in steel bridge girders is warranted: the recent observations of Lai (1997) and Fraser *et al.* (2000) have shown that Mode III fatigue loading can be a significant factor in the propagation of distortion-induced fatigue cracks. An extension of the experimental program performed by Fraser *et al.* (2000) would accomplish this goal. Further tests are also needed to confirm the results of Fraser *et al.* (2000) that the large fatigue cracks remained stable at temperatures of -50°C since only a small number of tests were performed. A finite element analysis should also be performed to better understand the behaviour of the web gap region.

From the rehabilitation schemes reviewed, the most promising are increasing the web gap lengths and providing a connection between the transverse stiffener and the tension flange. For the experimental program presented in the following, an increase in web gap length was not practical since the bottom of the transverse stiffener extended only a small distance below the bottom of the diaphragm angle (see Figure 1–2). Therefore, the effectiveness of an angle bolted to both the transverse stiffener and the tension flange will be investigated in this experimental program. Other rehabilitation techniques that decrease the amount of web gap distortion will also be considered.
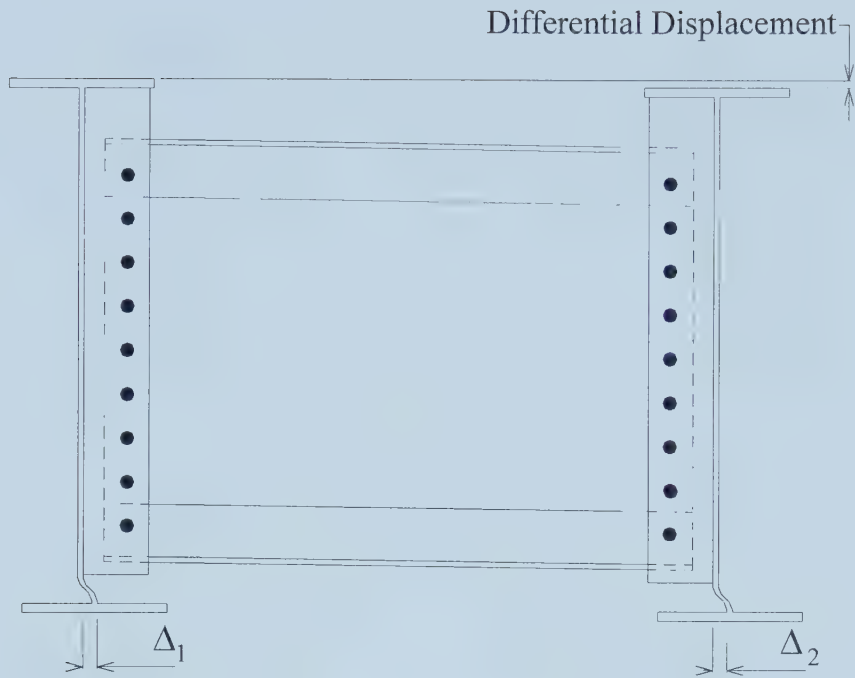
Figure 2–1 Typical Out-of-Plane Distortion of Web Gap
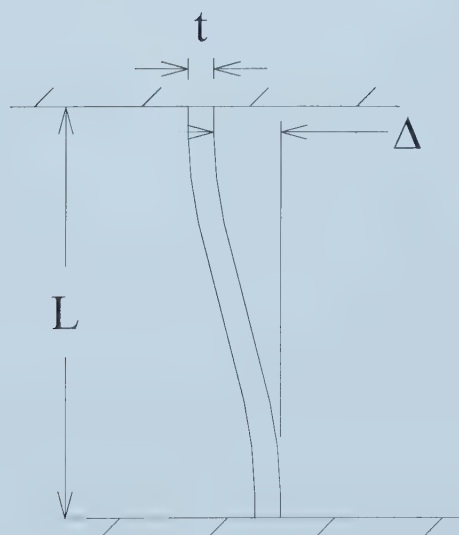
Figure 2–2 Idealization of Web Gap Distortion
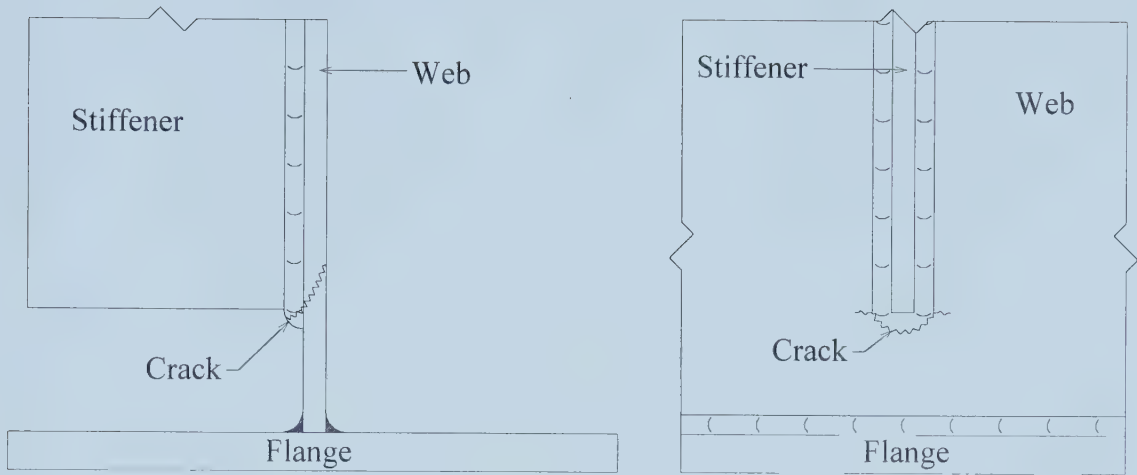
Figure 2–3 Schematic of Web Crack at End of Transverse Stiffener (Fisher, 1978)

MODE I   MODE III
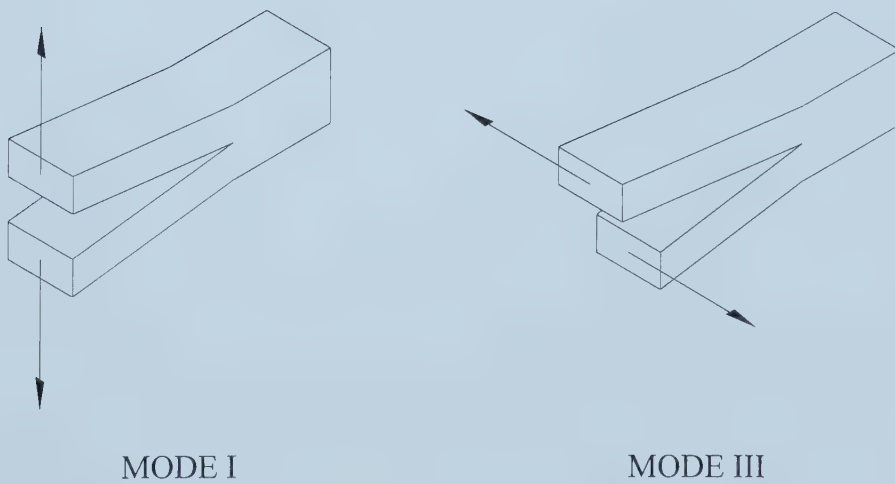
Figure 2–4 Models of Mode I and III Crack Surface Displacements
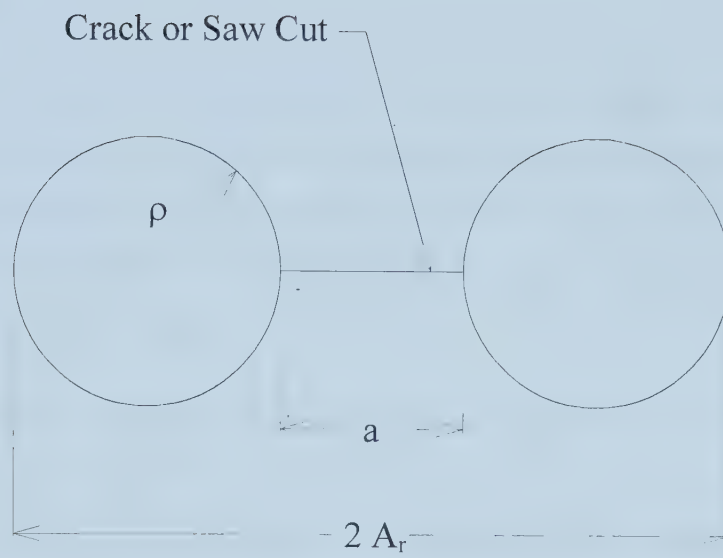
Figure 2–5 Stop Hole Drilling Rehabilitation Proposed by Fisher (1980)

3. EXPERIMENTAL PROGRAM

3.1 Introduction

An experimental program was undertaken to study the remaining fatigue life and the effectiveness of fatigue crack repairs on five girders obtained from the CN Mile 5.09 Edson Subdivision Bridge. The tests on the as-received girders were performed in order to better assess the behaviour of distortion-induced fatigue cracks under both ideal and simulated extreme winter conditions.

Fraser *et al.* (2000) used information obtained from analysis of field test data to design the type of laboratory test set-up used for this experimental program. This experimental program differs from that performed by Fraser *et al.* (2000) in a few ways. The differences include the change of stress range at the midspan extreme bottom fibre, the redesign of the diaphragm spring supports to accommodate a larger load range on the test specimens, and assessment of various fatigue crack repair techniques.

3.2 Test Specimens

The bridge girders obtained for laboratory testing comprised the east and west 9.9 m spans beneath the north service and main lines of the bridge when it had been in service (Figure 1–1). One girder in the set of four girders was a fascia girder, which had diaphragms only on one side. The fascia girder was removed when the bridge was dismantled, leaving the three other girders for laboratory testing. However, the wrong girder was removed in one set allowing for only five girders from two sets available for testing.

In order to recover the test specimens from the bridge for testing, the 250 mm reinforced concrete slab, which was composite with the steel members, had to be removed. The effect of the slab on the stress condition in the test specimens was restored by reinforcing the specimens with a W250×167 steel section bolted to the top flange of the test girder. In order to prepare the top flange for bolting of the reinforcing section, the shear studs had to be removed by flame cutting or abrasive wheel cutting, and this was followed by grinding of the top flange. The W250×167 reinforcing section of G40.21–M92 350W

steel was bolted to the top flange of the test specimens in order to raise the neutral axis to the level that had been measured in the field for the composite section (Fraser *et al.*, 2000). The reinforcing beam was bolted to the top flange of the specimen in the same manner as described by Fraser *et al.* (2000). The location of the bolts between the reinforcing beam and the test specimen is shown in Figures 3–1 to 3–3. The theoretical distance from the bottom flange to the neutral axis of the reinforced section was 819 mm, as compared to 847 mm measured in the bridge during a field test (Fraser *et al.*, 2000).

Repaired Specimens

As discussed in Chapter 2, the practice of drilling stop holes at the crack tips to arrest crack growth resulting from distortion-induced fatigue was found to be ineffective (Fraser *et al.*, 2000). The combination of Mode I and Mode III fatigue loading present in the web gap region, resulting from the combined in-plane bending of the girder and the out-of-plane deformation of the web, requires a different repair scheme. The practice of cutting back the stiffener to increase the length of the web gap and decrease the out-of-plane bending stresses in the web gap was not considered practical with these girders because the bottom of the diaphragm was close to the bottom of the stiffener. Therefore, the main objective of the repair was to reduce the out-of-plane deformation in the web gap region.

The use of bolted angles was investigated as a way of bridging a crack. Two different repair angle orientations, as shown in Figures 3–5 and 3–6, were considered. The first repair attempted, shown in Figure 3–7, was based on the current design method of connecting the transverse stiffener to the bottom flange. A 12.5 mm bent plate, referred to as the repair angle, was used to connect the stiffener to the bottom flange (see Figures 3–5 and 3–7). It was anticipated that by connecting the stiffener to the bottom flange, the web gap distortions would be significantly reduced, thereby decreasing the fatigue stresses. Before bolting the repair angle, the paint was removed from the stiffener and the bottom flange to increase the friction resistance between the girder and the repair angle. The repair angle was connected to the stiffener by first removing the bottom two bolts of the stiffener-to-diaphragm connection. The bolt holes on the stiffener were used

to mark the centre position of the holes that were punched through the repair angle. The stiffener and repair angle were then snug tightened together. Next, the bolt holes in the repair angle and the bottom flange were match drilled, and all bolts were tightened using the turn-of-nut method. Since the repair angle was slightly different for each specimen, the dimensions of the repair angles are presented in Chapter 4. (If slotted holes should be selected to ensure proper fit of a shop-prepared repair angle with the bolt holes of the transverse stiffener, proper bolt preload would be required. This can be achieved through the use of structural plate washers.)

The second repair scheme was designed to increase the thickness of the material in the web gap, thereby reducing web gap distortion and web gap stresses. Again, a 12.5 mm bent plate was utilised. However, as shown in Figures 3–6 and 3–8, the repair angle was connected to the web and the bottom flange of the girder on the opposite side of the transverse stiffener. This repair scheme increased the web out-of-plane stiffness, thus reducing the out-of-plane distortion and resulting stresses. The repair angle was clamped in place after removing paint and cleaning the contact surfaces of the web and bottom flange. Bolt holes were then match drilled through the repair angle and the bottom flange of the girder. After snug-tightening the bolts on the bottom flange. bolt holes were match drilled through the angle and the web. All bolts were then tightened using the turn-of-nut method. Refer to Chapter 4 for dimensions of repair angles.

Repairs were made to specimens 2. 3 and 4 after the most severe fatigue crack had reached a length of approximately 150 mm. (In practice. it is likely that girders with such large cracks would have been repaired or taken out of service prior to this point.) This is similar to the criterion used by Fraser *et al.* (2000) to determine when fatigue testing could be stopped. The repairs were made only at the joints with fatigue cracks that showed significant growth.

Repairs to the fifth specimen were made after the correct cyclic behaviour was obtained and the extent of fatigue cracking was confirmed. that is. after 10 000 load cycles. All four joint locations in the constant moment region with fatigue cracks were repaired. The repair consisted of drilling stop holes to blunt the crack tips that did not have pre-existing

stop holes, followed by bolting repair angles at all four joint locations. Two joints were repaired by connecting the repair angle to the stiffener and the bottom flange, similar to the scheme shown in Figure 3–7. The other two joints were repaired by connecting the web and bottom flange to the repair angle, similar to Figure 3–8. Chapter 4 presents details of all the repairs made. These early repairs were implemented to illustrate the effectiveness of a typical repair performed when fatigue cracks are first detected in the bridge girders.

The repair angle was considered effective if there was little or no crack growth up to at least 2 million cycles. This limit was considered adequate since the cracks that first re-initiated past the stop holes, grew by about 50 mm within 2 million cycles in the tests conducted at the same stress range (Fraser *et al.*, 2000).

3.3   Test Setup

The specimens were tested in a four-point bending configuration. Two 530 kN actuators were used to apply the cyclic loads on the test specimens, creating a constant moment region of 4000 mm at the centre of the span. The shear spans were 2950 mm. The applied loads and the reaction forces were measured using four load cells.

Roller supports were provided at the end reactions of the test specimen and lateral bracing was provided to the top and bottom flanges of the girder at the two locations indicated in Figure 3–4. The lateral bracing on the top flange was provided to simulate the lateral support of the concrete slab. Since the diaphragm end supports were not designed to provide the lateral support that was present in service by the diaphragms and adjacent girders, bottom flange lateral bracing was provided. Figure 3–4 shows the orientation of the test specimen in the load frame and the positions of the lateral bracing along the girder span.

The diaphragm sections were connected to the test specimen using the original 7/8 in. diameter A325 bolts. All diaphragm-to-stiffener bolts were preloaded using the turn-of-nut method. The end of each diaphragm was then mounted on HSS end supports as shown in Figures 3–2 and 3–3. These supports, which simulated springs, were used to

obtain the desired differential displacement between the ends of the diaphragms. Work by Fraser et al. (2000) indicated that different support stiffness was required for each diaphragm in order to replicate field conditions. Figure 3–9 and Figure 3–10 show different views of the overall test set-up. Test specimens 1 and 2 were tested using diaphragm end supports similar to those used by Fraser *et al.* (2000) and illustrated in Figure 3–2. Because both the maximum stress and the stress range used for the first four tests were considerably larger than those used by Fraser *et al.* (2000), significant wear was observed on the bottom HSS section at a few joint locations. New diaphragm spring supports were therefore needed for the remaining test specimens as shown in Figure 3–3. Fraser *et al.* (2000) used two HSS 51×25×3.2 members oriented so as to produce weak axis bending of the sections and loaded at midspan through the vertical HSS member. In order to provide the desired spring stiffness for the diaphragm end supports, the span lengths used during those tests ranged from 700 mm to 830 mm for Joints 3, 4, 5, 18, 19, and 20 (see Figure 3–4 for the joint locations), and span lengths ranging from 490 mm to 520 mm were used for joints 6 and 17.

Connection of the HSS beam sections to the HSS verticals in the diaphragm support arrangement was made through pin connections, which penetrated through the HSS beam member webs above the neutral axis position in the compression zone.

In order to carry out the low temperature tests, insulated chambers were built around the test specimens at selected diaphragm locations. The chambers enclosed full depth of the reinforced test specimen over a girder length of 460 mm. Each chamber consisted of 51 mm Styrofoam SM–C sheets and all joints were sealed using an all-purpose silicone epoxy rated to –54°C. The chambers enclosed the full depth of the built-up test section over a 460 mm length of the girder. Figure 3–11 shows the insulated chamber mounted around test specimen 1 at Joint 10. In order to decrease the temperature inside the insulated chambers to –50°C, CO_2 dry-ice pellets were placed on shelves within the chambers. Fans were used to circulate the cold air throughout the insulated chambers that surrounded the crack locations.

3.4 Instrumentation

The applied loads were measured using load cells that were mounted to each actuator. The support reactions at the north and south ends of the test specimens were also measured using load cells.

Twelve 120 ohm, 5 mm gauge length electrical resistance strain gauges were mounted on each test specimen at midspan (see Figure 3–12) to monitor the strain distribution over the depth of the section and possible out-of-plane displacements of the test specimen. From the strain gauge data, the specimen properties and load effects at midspan were assessed during laboratory testing.

Six 120 ohm, 2 mm gauge length strain rosettes were mounted around the bottom of one transverse stiffener. Three rosettes were mounted on both the east and west faces of the girder to measure the strain field around the end of the stiffeners prior to the formation of cracks. Test specimen 2 was not instrumented with strain rosettes because cracking and stop holes were present at all joints within the constant moment region prior to testing. Strain rosettes were mounted at Joint 11 on specimen 1 and at Joint 12 on the last three specimens. It should be noted that Joint 12 of specimen 4 was instrumented even though stop holes were present. The orientation of the strain rosettes is shown in Figures 3–13, 3–14 and 3–15. The measured strains in the web gap area will be compared with the results of a finite element analysis in Chapter 5.

Displacement transducers (LVDTs) were mounted beneath the web of the girder and beneath the spring-supported end of the diaphragm to measure the differential displacements at each diaphragm. Figure 3–16 shows the orientation of the LVDTs at a typical diaphragm location.

The out-of-plane web distortions were measured at the diaphragms located within the constant moment region with two LVDTs, as shown in Figure 3–17.

All instrumentation was monitored using National Instruments SCXI–1100 high-speed data acquisition system. All gauges and instruments were sampled at a rate of 1000 Hz and data were collected using Lab View® software.

The temperature distribution on the test specimens within the insulated chambers was measured using 330 kilo-ohm thermistors mounted over the girder depth. Thermistor resistance readings were measured using an ohmmeter and were converted to temperature using the calibration tables provided with the thermistors. The locations of the thermistors on each test specimen tested at low temperature are shown in Figure 3–18.

3.5 Test Procedure

The bottom fibre stress range chosen for testing purposes by Fraser *et al.* (2000) was equal to the maximum in-situ stress range of 35 MPa measured during a field test conducted with two Class EF–644a locomotives. At the time, this stress range was considered to be an upper bound service stress range since the Class EF–644a locomotive used for the field test is currently one of the heaviest locomotives. Further consultation with CN Rail revealed that the Class EF–644a locomotive might not have been properly fuelled. CN Rail officials also expressed concern that future service loads will increase in both load and frequency; therefore, a larger stress range was desired. Hence, it was decided that the 35 MPa stress range used by Fraser *et al.* (2000) would be the lowest stress range used in the overall testing program. A stress range of 50 MPa was used for the first four tests in this testing program. After completing the first four tests, it was decided that the final test would be conducted at a stress range of 35 MPa and that the pre-existing cracks that had been field repaired with stop hole drilling would be rehabilitated with angles prior to testing. It should be noted that all the other specimens were repaired after the pre-existing cracks had propagated deep into the web during the first part of the test. See Section 3.2 for further details of the repairs.

The minimum stress of 12 MPa used by Fraser *et al.* (2000) was also used in this testing program. This minimum stress is enough to ensure that the loading jacks do not lift away from the girder. The maximum stress for the first four specimens was 62 MPa and was 47 MPa for the last specimen. To determine the loads required for these stresses, the correct differential displacements at the diaphragm positions due to the 47 MPa maximum stress were first needed. The differential displacements of each specimen were compared to the values from the field tests for a bottom fibre stress of 47 MPa, as shown

in Table 3–1. After the desired differential displacements were established, the loads required for the 62 MPa bottom fibre stress were obtained for the first four specimens only.

The procedure adopted for testing of each bridge girder was as follows:

1. The reinforcing section was secured to the top flange of each girder and the specimen was placed into the load frame and positioned beneath the actuators.

2. The end and lateral supports were mounted and the diaphragms were bolted to the test specimen.

3. The spring supports were mounted at the free ends of each diaphragm.

4. All instrumentation was mounted and the specimen areas around the diaphragm positions were cleaned of paint and brushed with whitewash so that cracks could be readily observed and measured.

5. A static test was performed to determine the actuator load and spring member span lengths required to develop the 47 MPa bottom fibre stresses at midspan and differential displacements similar to those presented in Table 3–1. Once the spring member span lengths were obtained, the loads required to obtain the 62 MPa bottom fibre stress (maximum stress during fatigue testing) for the first four specimens were then determined. The resulting load magnitudes and spring member span lengths are presented for each specimen in Chapter 4.

6. Cyclic testing was started using a sinusoidal wave shape. In order to compensate for inertia forces, the maximum dynamic loads were increased, the minimum loads were decreased and the load frequency was adjusted until the maximum and minimum test stresses and the 50 MPa stress range (first four specimens), or the 35 MPa stress range (fifth specimen) were achieved. The revised dynamic test load values are presented in Chapter 4. With the dynamic loads set to values that achieved the target maximum and minimum test stresses, the displacements at the ends of each diaphragm were monitored. Once the displacement measurements were obtained, all the LVDTs were removed. Load control was used during fatigue testing; since, the

girder would be subjected to imposed loads in service rather than imposed displacements.

7. Monitoring of the cracks at each diaphragm location was carried out during fatigue testing in order to determine the crack patterns and the crack growth rates at each location.

8. For the first three specimens an insulated chamber was mounted around the diaphragm location where extensive cracking of the girder web had taken place and a low temperature test was performed. During the freeze test, the specimen was loaded statically and the cracks were monitored. Two static load tests were performed while the temperature in the chambers was maintained at −50°C. The first of two load tests was performed with two equal loads and a midspan bottom fibre stress of 62 MPa. The other static load test was performed while loading the specimen with only one actuator, again targeting a midspan bottom fibre stress of 62 MPa. This second load case was selected in order to observe the effect of combined shear and moment at the crack location. In each case, the static loads were maintained for approximately 10 minutes and strain readings were recorded before, after, and during load application. For the third specimen, dynamic testing was continued for several hours while the temperature inside the chamber surrounding the crack at Joint 12 was held close to −50°C. The crack length at this location was measured before and after the test to see if the crack growth rate changed as a result of the low temperature conditions.

9. Once the fatigue cracks had grown to a length of approximately 150 mm, fatigue testing was stopped to allow for repairing of the specimen. Prior to repairing the specimen, a static test was performed. Another static test was performed after completion of the repair. During both static tests the midspan strain gauges and the LVDT measurements were monitored.

10. Fatigue testing and monitoring of the cracks was resumed.

11. The criterion used to determine whether or not the repair was adequate was based on further fatigue crack growth. If crack growth continued after the repair, then the

crack was allowed to grow to about 200 mm at which point the fatigue test was concluded. However, if no significant crack growth was observed after approximately 2 million cycles, the repair was considered effective and fatigue testing was stopped. It should be noted that steps 9 to 11 were not performed on the first specimen.

12. Before dismantling a girder, a final static test was performed while monitoring the strain gauges at midspan and the diaphragm LVDTs.

The testing procedure was modified for the last specimen. Steps 1 to 6 were followed as above, but fatigue loading of the specimen was stopped after 10,000 cycles. During the initial 10,000 cycles the existing fatigue cracks were monitored. Afterwards, 24 mm diameter stop holes were drilled at the crack tips at all joint locations that did not have pre-existing stop holes. At locations with pre-existing stop holes, the holes were ground to ensure that cracks too small to be observed were removed. Steps 9 to 12 were then followed.

3.6 Ancillary Tests

Tension coupon tests and Charpy V-notch impact tests were used to determine the material properties of the girder steel. Two tension coupons from the web of each of the test specimens were tested to evaluate the steel used for the girders. The tension coupon tests were conducted in accordance with ASTM Standard A370–97a (ASTM, 1992). The tension coupon tests were performed at a strain rate of approximately 10 $\mu\varepsilon$/s in the elastic range and 50 $\mu\varepsilon$/s in the inelastic range. Static stress values were obtained at regular intervals during the tests.

Charpy V-notch specimens were also obtained from the web of each girder near the web gap regions. Subsized specimens were used because the web thickness of the girder was less than the 10 mm standard cross-sectional dimension. The subsize specimens had cross-sectional dimensions of 7.5 mm x 10 mm and conformed to ASTM Standard A370–97a (ASTM, 1997) for three-quarter size Charpy specimens. In accordance with A370–97a, the notch was oriented so that the notch front was in the direction of the

minimum dimension, i.e. the through thickness dimension. Two impact tests were performed at each of +20°C, −25°C, and −50°C. Required test temperatures for railway bridge steel are specified in Chapter 15 of the AREA (1994) code and vary from +20°C to −23°C for grades of steel similar to the one used in the Edson Subdivision Bridge (G40.8 Grade B is specified on as-built drawings). The −50°C test temperature was used to match the temperature used in the low temperature tests performed on the full-scale specimens. A commercial laboratory performed the Charpy V-notch impact tests.

Table 3–1

Girder Displacements at Diaphragm Locations
(Fraser *et al.*, 2000)

| Joint | Vertical Displacement (mm) | Differential Displacements | |
		Designation	Displacement (mm)
2	-0.27		
		Δ_{7-2}	0.27
7	0.00		
3	-1.13		
		Δ_{9-3}	-0.00
9	-1.13		
4	-1.43		
		Δ_{11-4}	-0.25
11	-1.68		
5	-0.98		
		Δ_{13-5}	-0.37
13	-1.36		
6	0.00		
		Δ_{15-6}	-0.33
15	-0.33		
8	-0.33		
		Δ_{8-17}	-0.33
17	0.00		
10	-1.36		
		Δ_{10-18}	-0.38
18	-0.97		
12	-1.68		
		Δ_{12-19}	-0.27
19	-1.41		
14	-1.13		
		Δ_{14-20}	-0.01
20	-1.12		
16	0.00		
		Δ_{16-21}	0.27
21	-0.27		

* Refer to Figure 3-4 for joint locations.

Typical Test Girder Section
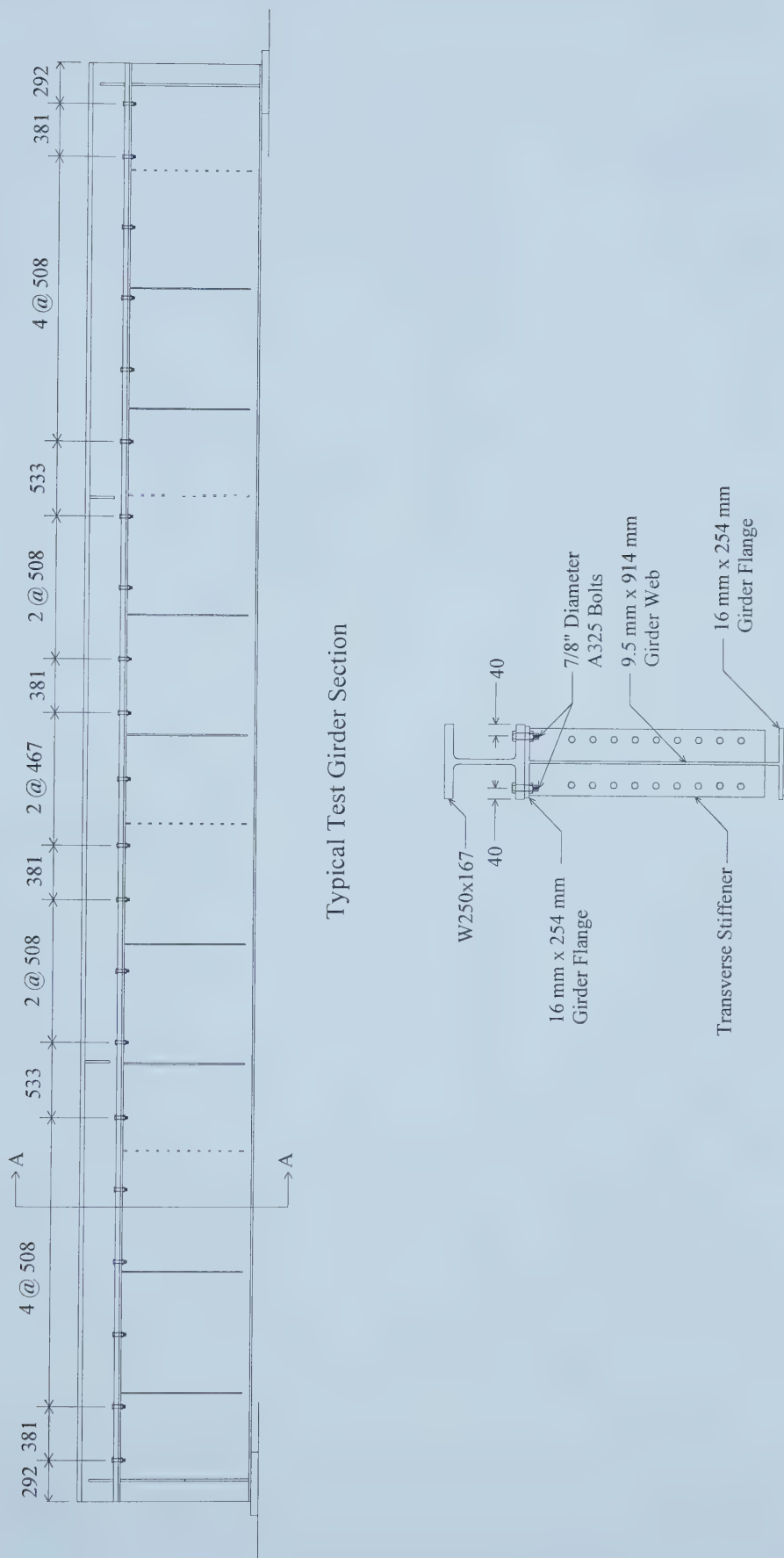
Section A-A

All dimensions in mm

Figure 3–1 Built-Up Test Section (Fraser *et al.*, 2000)

28

Cross-Section

9.5 mm x 686 mm
Diaphragm Web Plate

6 ⟍ 75

L 102 x 102 x 9.5 Diaphragm
Flange Sections

Connector Plates (NS & FS)

HSS 38 x 38 x 3.2
Spring Members

Angle Supports

EQ   EQ

Varies
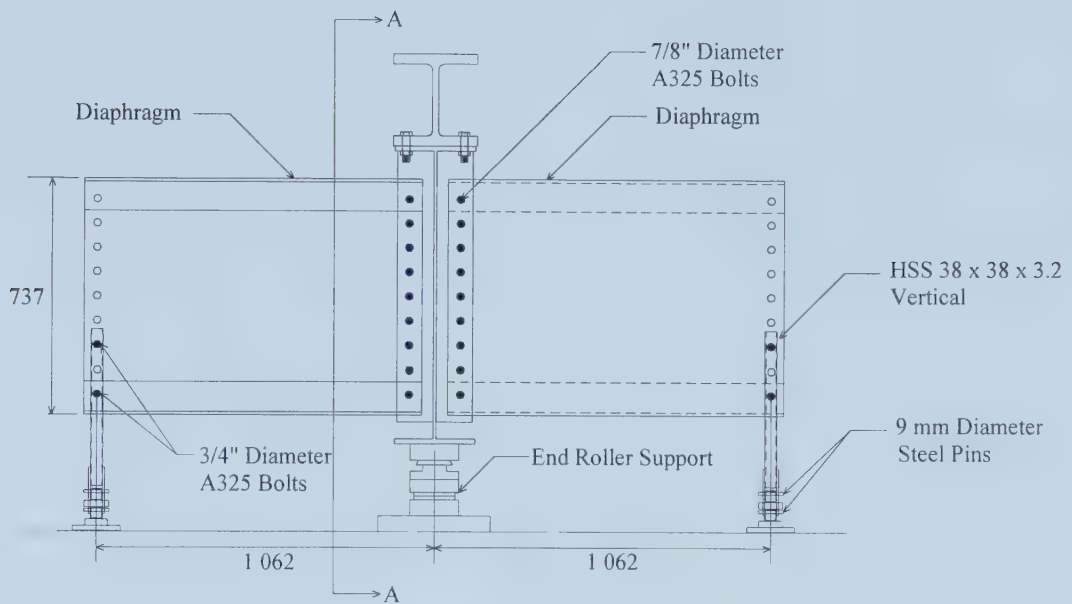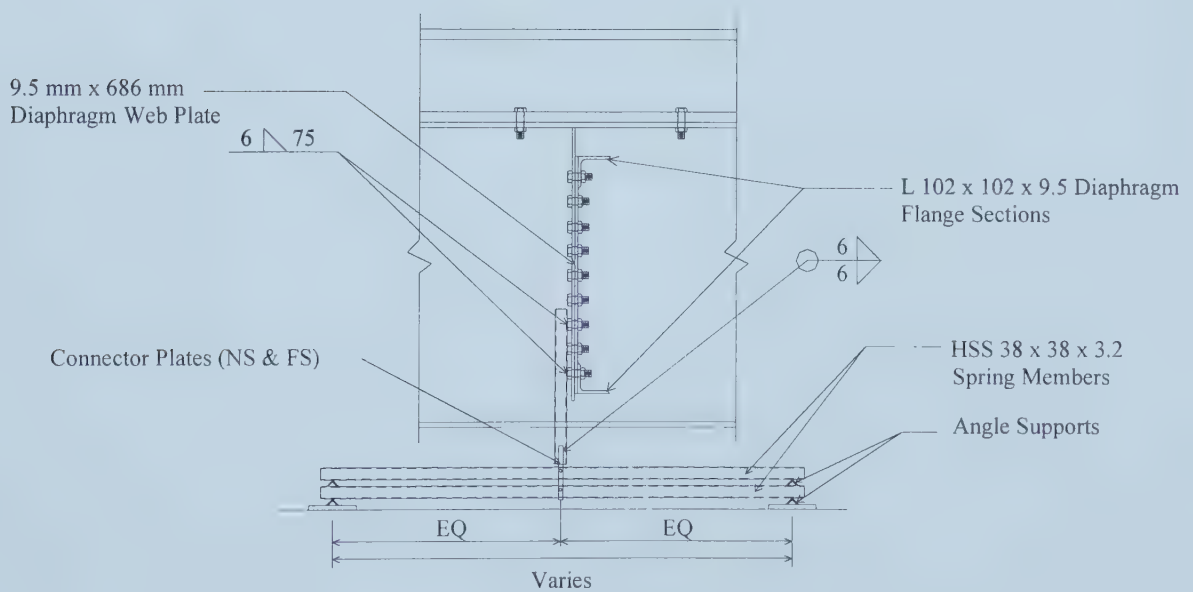
Section A-A

All dimensions in mm

Figure 3–2 Typical Cross-Section and Spring Support Details for Specimens 1 and 2
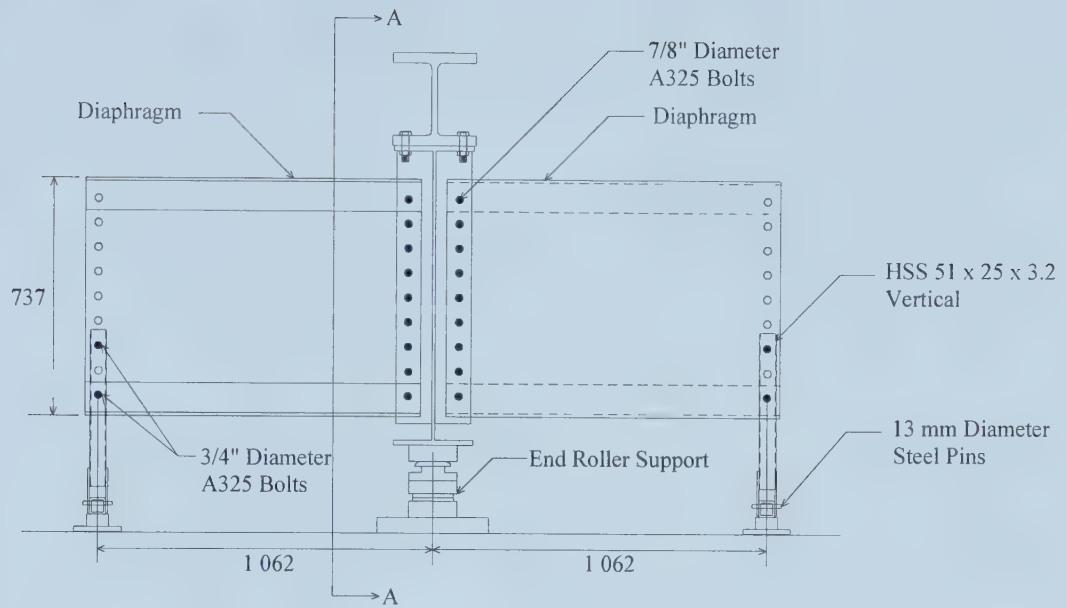
Cross-Section
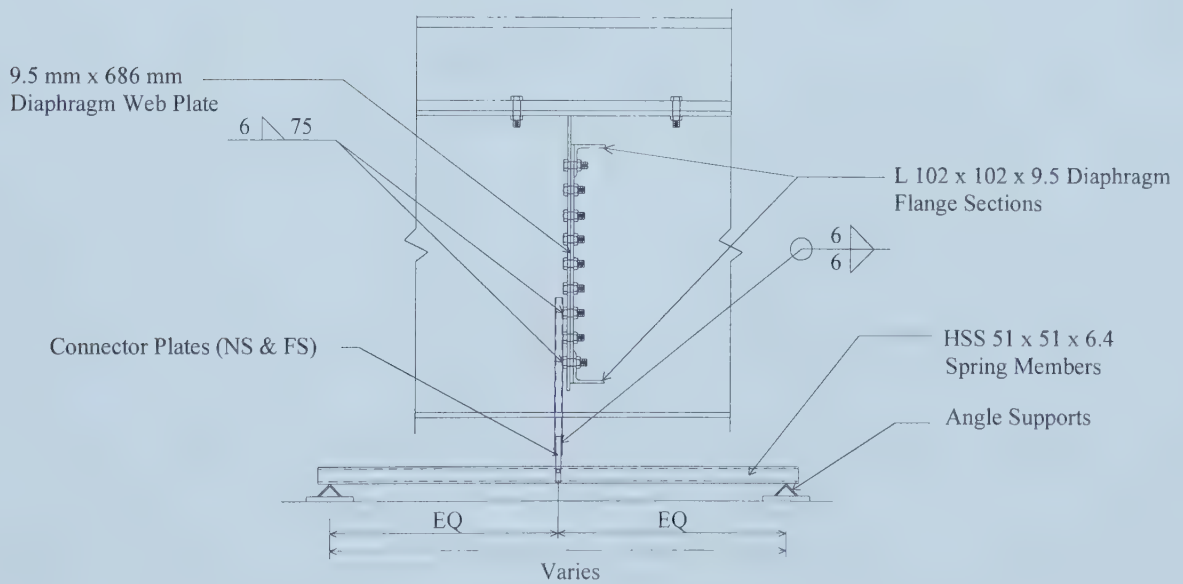
Section A-A

All dimensions in mm

Figure 3–3 Typical Cross-Section and Spring Support Details for Specimens 3, 4, and 5
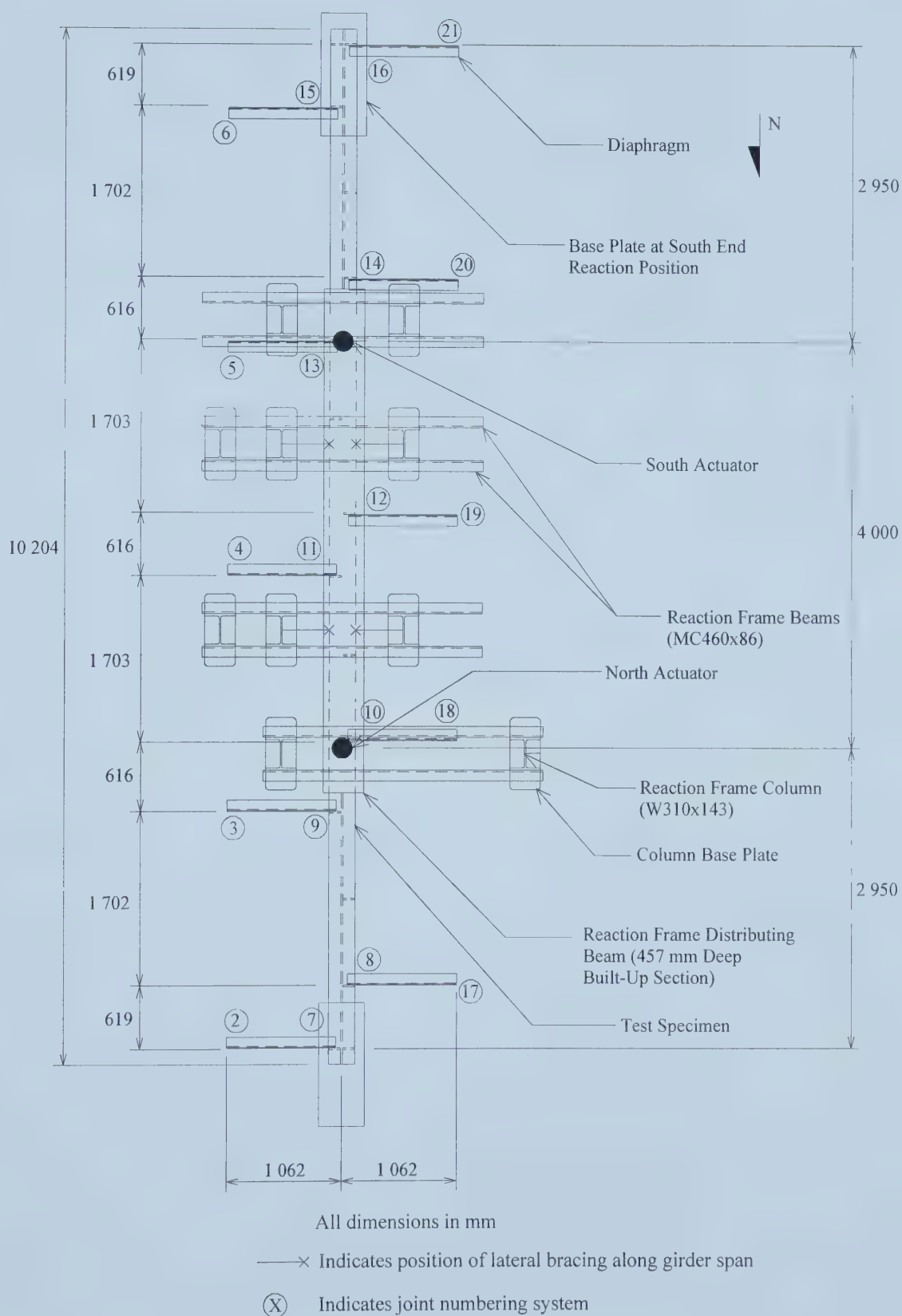
Figure 3–4 Plan View of Test Setup (Fraser *et al.*, 2000)
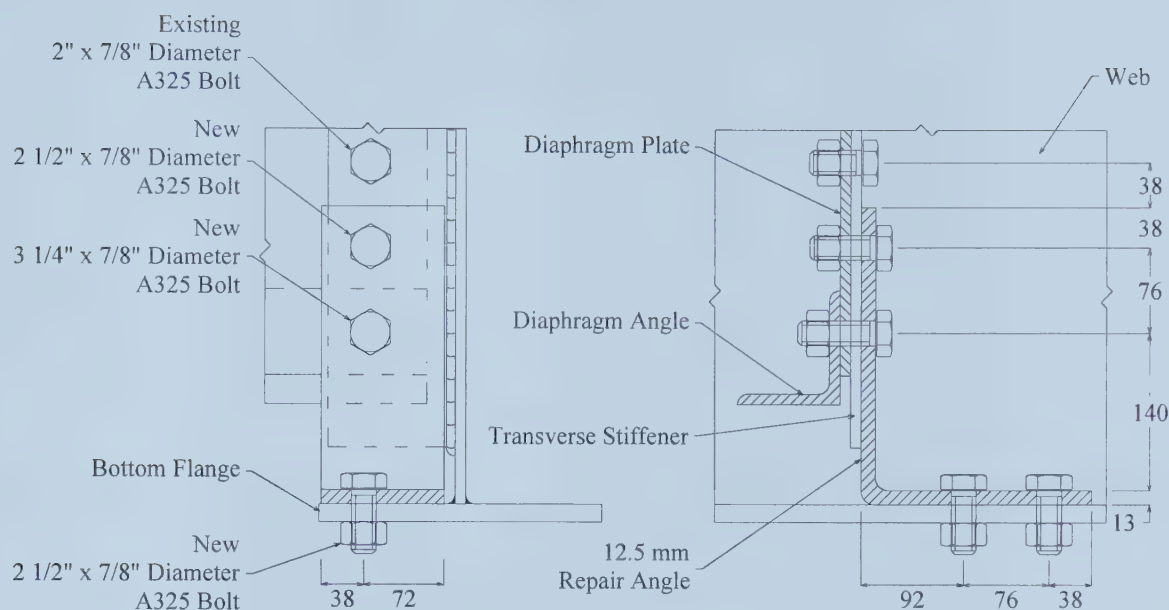
Figure 3–5 Orientation of Typical Repair Angle Connected to Transverse Stiffener and Bottom Flange
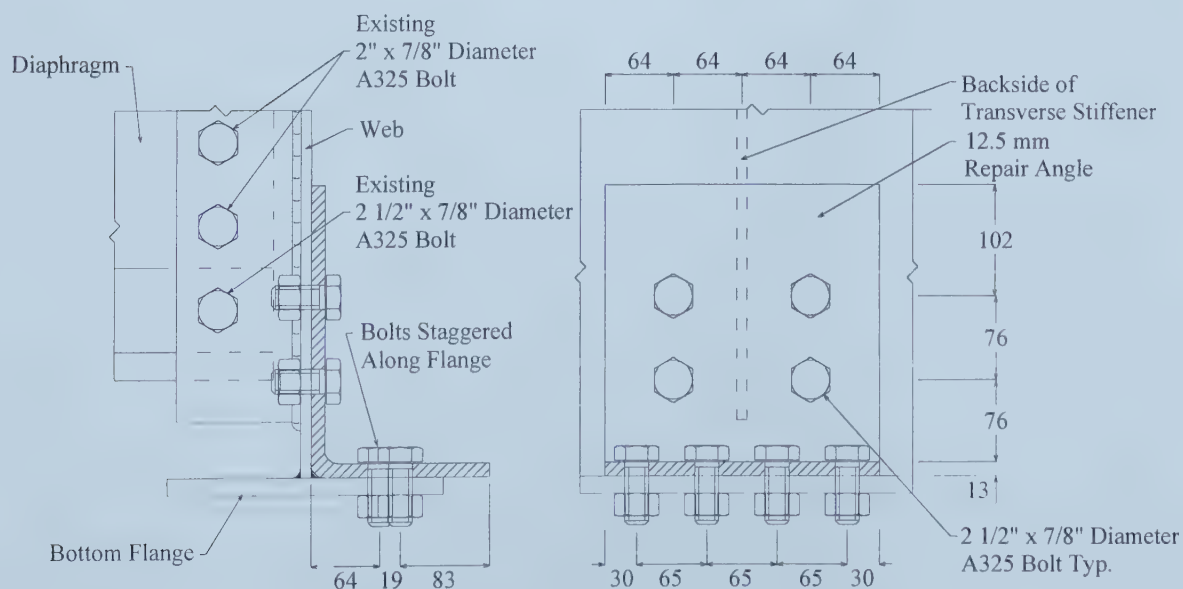
Figure 3–6 Orientation of Typical Repair Angle Connected to Web and Bottom Flange

32
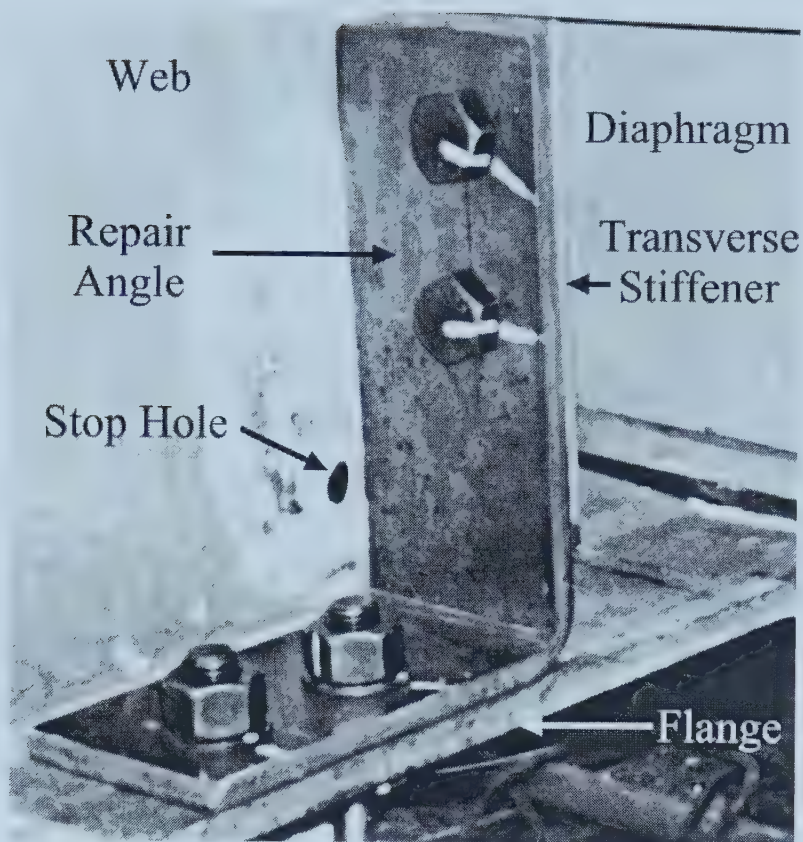
Figure 3–7 Typical Repair Angle Connected to Transverse Stiffener and Bottom Flange

Figure 3–8 Typical Repair Angle Connected to Web and Bottom Flange
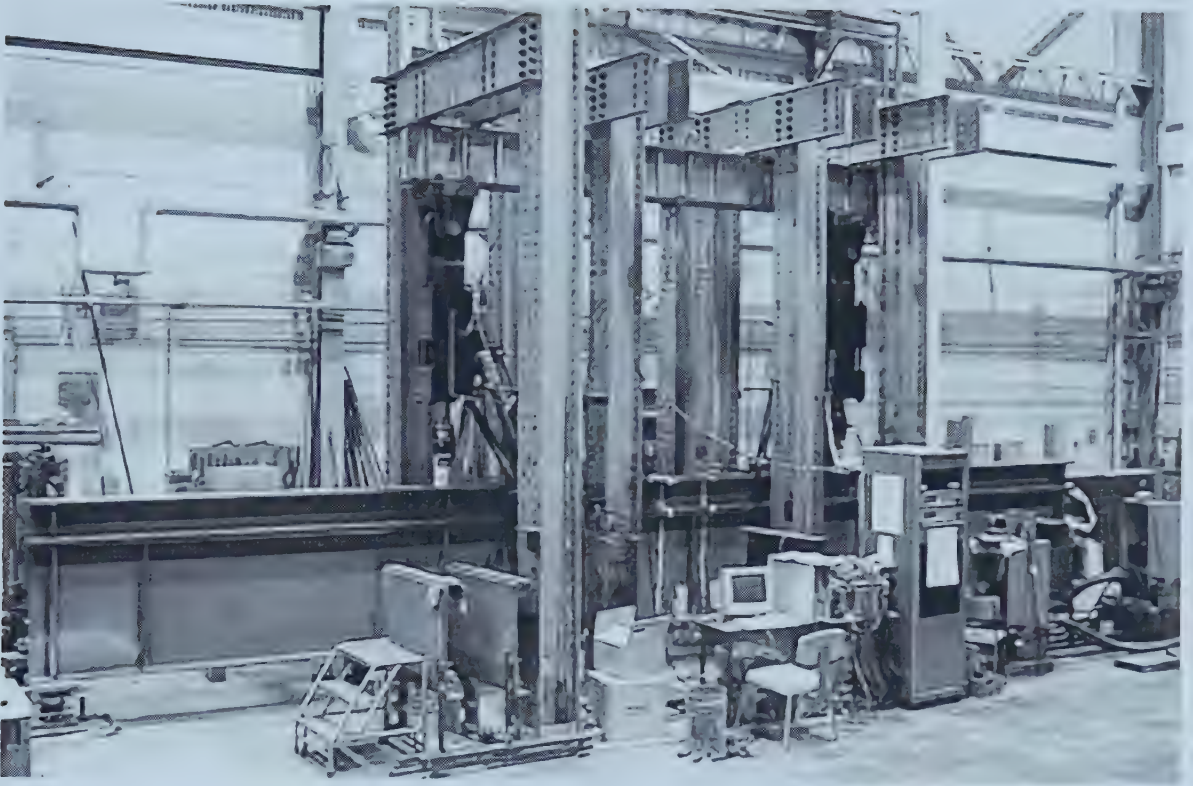
Figure 3–9 Specimen 1 Looking East
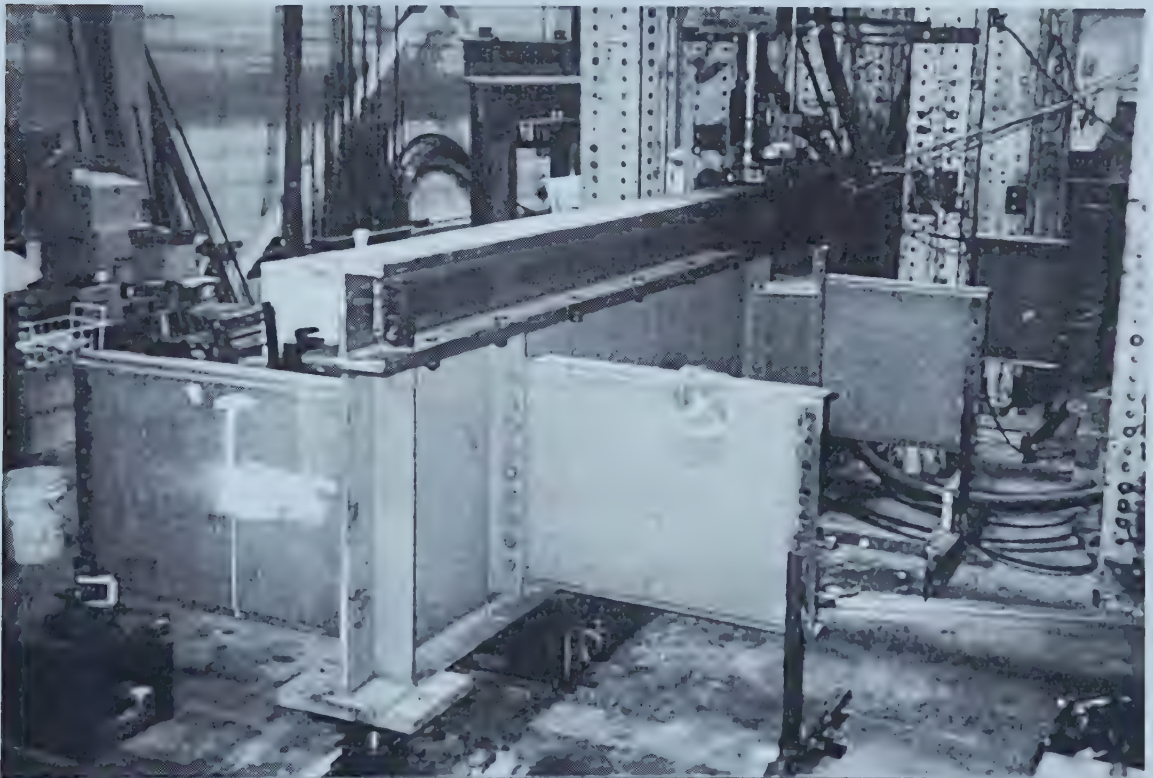
Figure 3–10 Specimen 1 Looking South

Figure 3–11 West Side of Insulated Chamber Surrounding Joint 10, Specimen 1
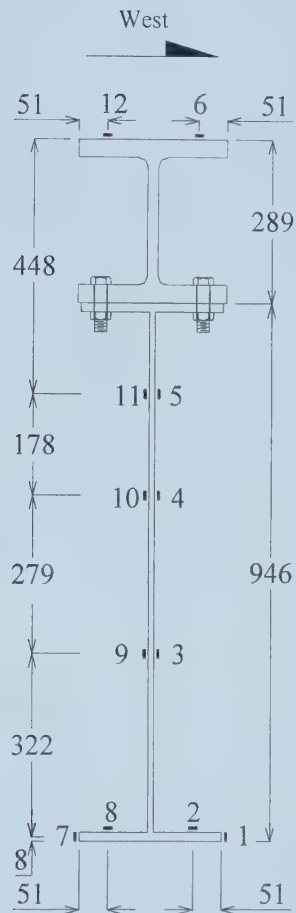
All dimensions in mm

Figure 3–12 Location of Strain Gauges Mounted at Midspan of Test Specimen
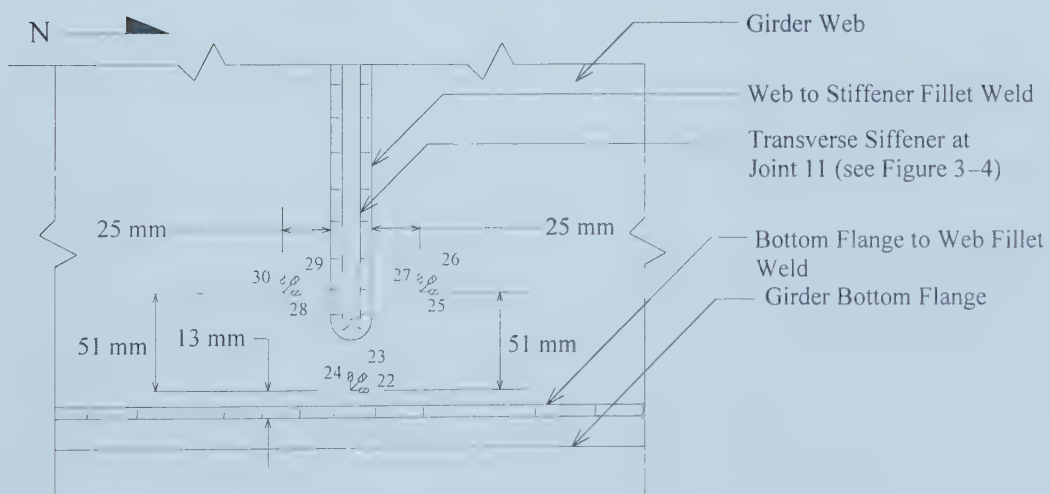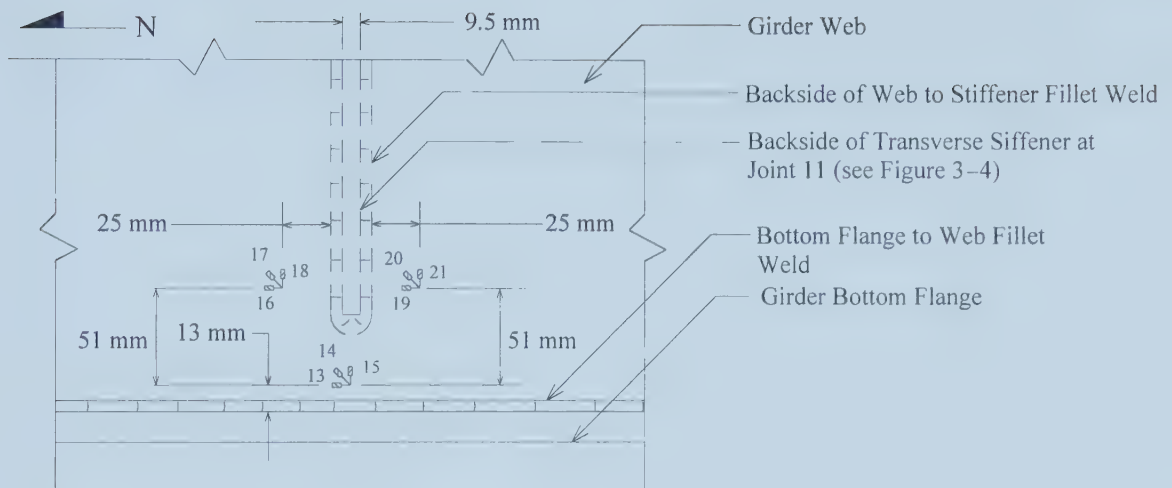
Figure 3–13 Orientation of Strain Rosettes at Joint 11 of Specimen 1

West Face

N

9.5 mm — Girder Web

Web to Stiffener Fillet Weld

Transverse Siffener at
Joint 12 (see Figure 3–4)

25 mm — 25 mm

Bottom Flange to Web Fillet
Weld
Girder Bottom Flange

17 20
18 21
16 19

51 mm 13 mm 51 mm

14
13 15

West Face

N

Girder Web

Backside of Web to Stiffener Fillet Weld

Backside of Transverse Siffener at
Joint 12 (see Figure 3–4)

25 mm — 25 mm

Bottom Flange to Web Fillet
Weld
Girder Bottom Flange

29 26
30 27
28 25

51 mm 13 mm 51 mm

23
24 22

East Face

Figure 3–14 Orientation of Strain Rosettes at Joint 12 of Specimens 3 and 5
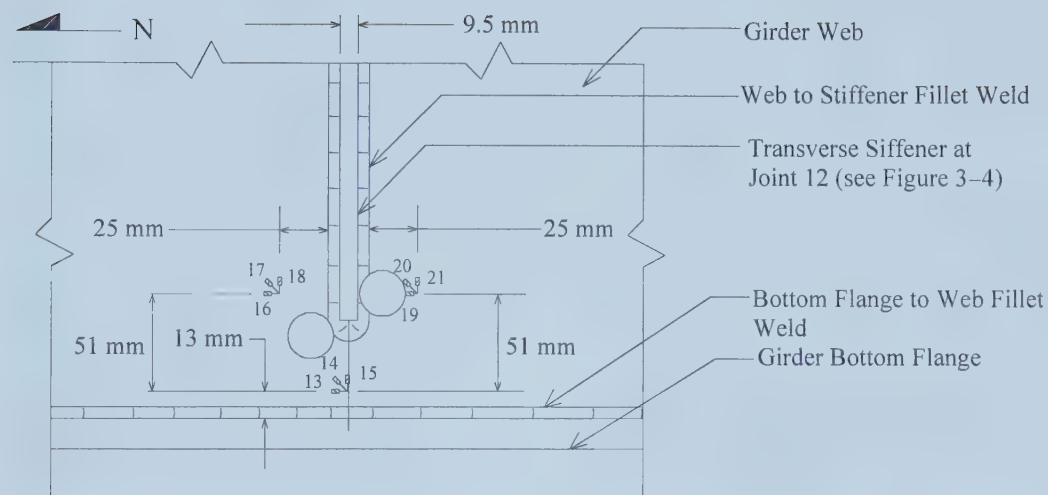
West Face
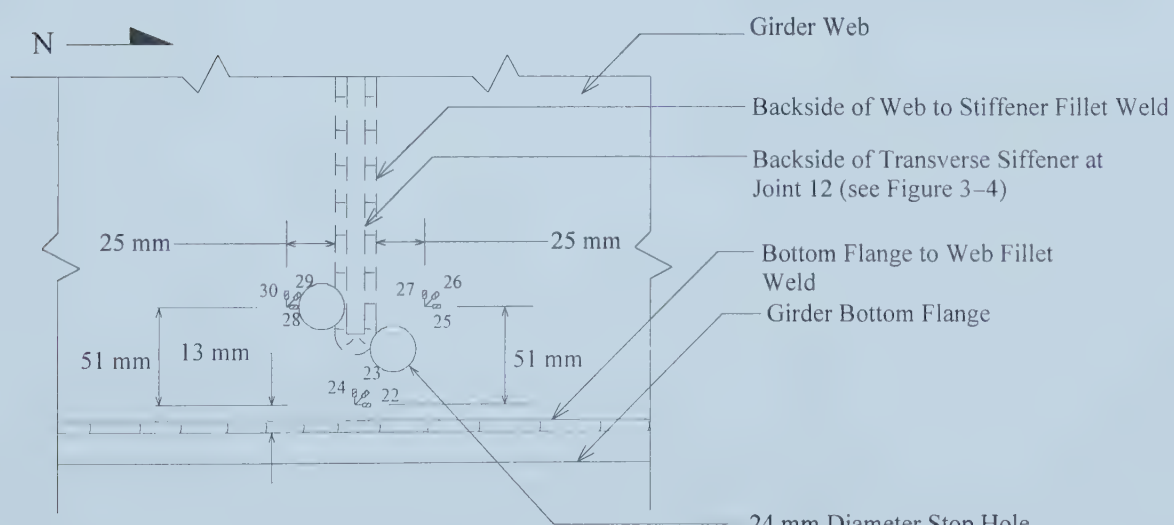
East Face

Figure 3–15 Orientation of Strain Rosettes at Joint 12 of Specimen 4
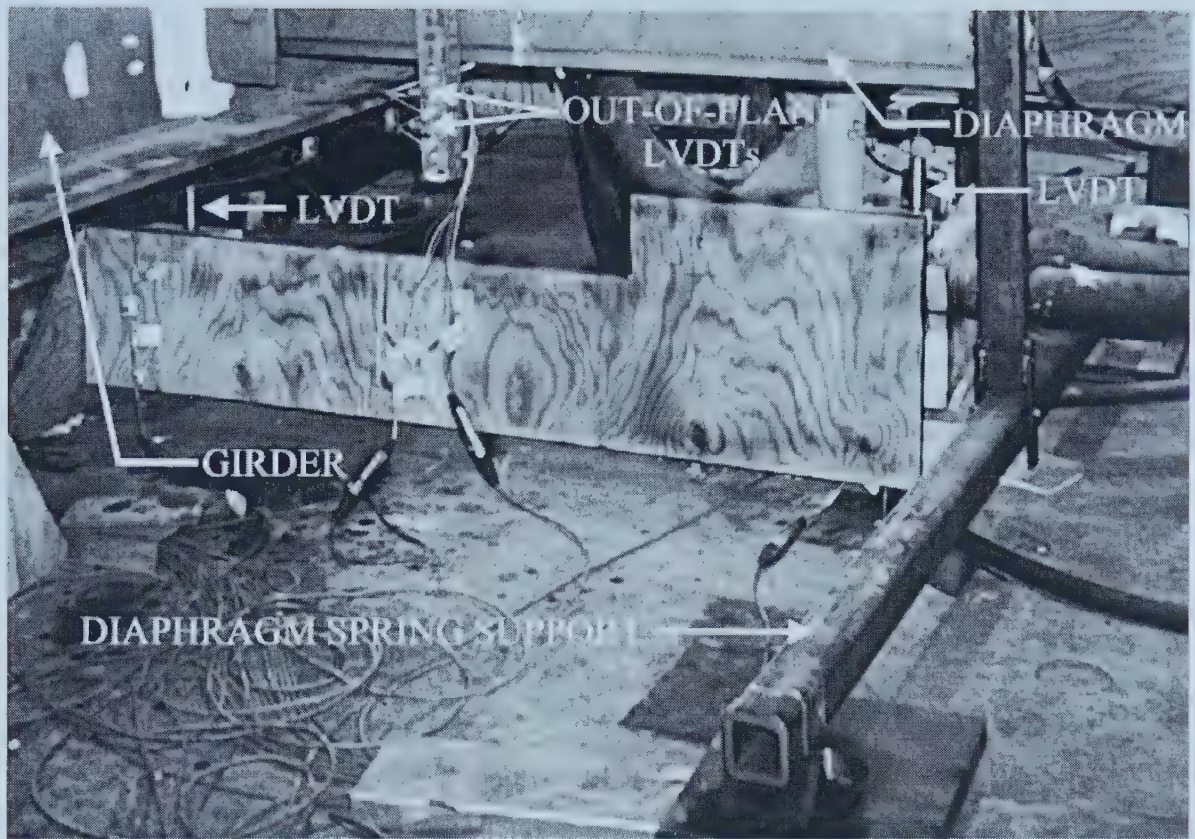
Figure 3–16 Typical Orientation of LVDT's Mounted Beneath Diaphragm Locations
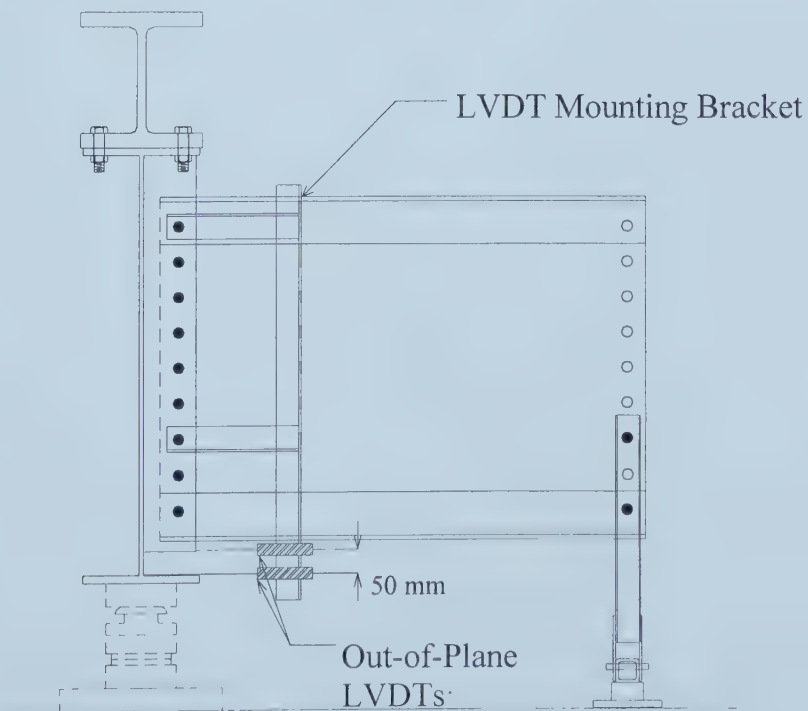
Figure 3–17 Instruments Used to Measure Out-of-Plane Web Distortion
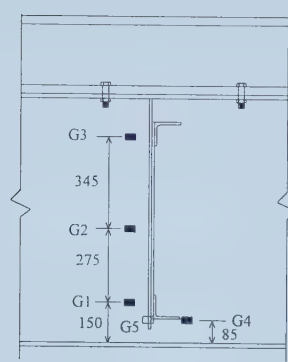
Joint 10

Specimen 1
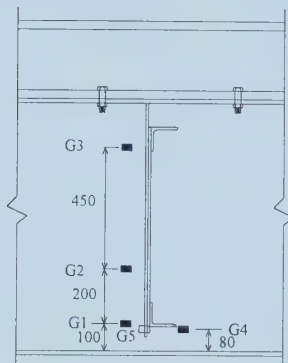
Joint 10

Specimen 2
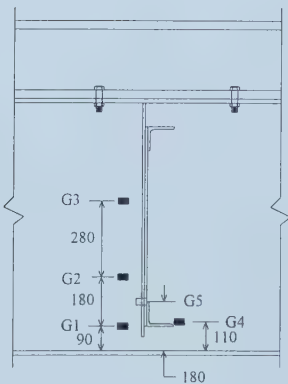
Joint 12

Specimen 3

■ Thermistor on West Face

▫ Thermistor on East Face

All dimensions in mm

Figure 3–18 Location of Thermistors in Insulated Chambers

41

4. TEST RESULTS

4.1 Results of Fatigue Tests

4.1.1 Visual Inspection of Test Specimens

Test specimens were visually inspected with a magnifying glass prior to and during the initial 20 000 load cycles of fatigue testing in order to determine the extent of existing cracks and to identify any stop holes that had been drilled in the girder web at each diaphragm location. The determination of existing cracking was most effective if performed while cyclic loads were being applied. The results from that inspection are summarized in Tables 4–1 through 4–5 and the joint numbers used in the tables are shown in Figure 3–4. Figure 4–1 describes the dimensions L1 to L4 used to detail the location of the stop holes (Tables 4–1 through 4–5). Typical cracks and stop holes on the east and west faces of a girder are presented in Figures 4–2 and 4–3. Figure 4–4 shows a repair that involved two stop holes drilled on one side of the stiffener. The inspection for cracks did not reveal any cases where a crack had extended past the drilled holes.

4.1.2 Initial Test Conditions and Specimen Behaviour

Static tests were performed at the beginning of each test to establish the applied loads and the diaphragm end support conditions required to produce the desired bottom fibre stress in the test specimen and the racking motion in the diaphragms. The results of the initial static tests performed on each of the test specimens are presented following. The results include the measurements of the girder end reactions, the distortions in several of the web gap regions, and measured strains at one of the web gap locations.

Test Specimen 1

Figure 4–5 shows a typical plot of the normal flexural strain distribution over the depth of the cross-section on the east and west faces of the specimen (see Figure 3–12 for the location of strain gauges). The regression lines obtained from the test data recorded at a load level of 146 kN per actuator are also shown in the figure. The position of the neutral axis, calculated from the regression line, was determined to be 810 mm on the east face

of the specimen and 812 mm on the west face. The bottom fibre strain of 235 με (at mid-width of flange) was also determined from the regression analysis. Using the measured modulus of elasticity, the bottom fibre stress at mid-width of the flange was calculated as 47 MPa. The position of the neutral axis was within 5% of the field-measured value obtained by Fraser *et al.* (2000). Both the neutral axis position and the bottom fibre stress were also in good agreement with the experimental design values of 819 mm and 47 MPa, respectively. The differential displacements due to the 146 kN actuator loads were within 10% of the differential displacements determined from the analysis, calibrated from field test results, performed by Fraser *et al.* (2000) (see Table 3–1).

Table 4–6 shows the differential displacements resulting from the maximum static load of 193 kN per actuator, which was required to achieve the maximum midspan bottom fibre stress of 62 MPa used during cyclic testing. Also tabulated in Table 4–7 are the actual span lengths of the spring support members used to support the ends of the diaphragms.

For static test loads of 193 kN per actuator, the north and south girder end reactions were measured as 170 kN and 168 kN, respectively. The reaction force at each diaphragm support was calculated using the displacements measured at each diaphragm end support and the tabulated moment of inertia for the HSS used for the diaphragm supports (see Table 4–7). The total load transferred through the diaphragms and into the diaphragm end supports was determined to be 43 kN. Adding these diaphragm end reactions to the measured beam end reactions yields a total reaction of 381 kN, compared to 386 kN measured at the actuators. The measured and calculated reactions are therefore in good agreement with the applied loads.

The stresses in the web gap region at Joint 11 are presented in Table 4–8. The stresses were obtained by multiplying the measured strains by the measured modulus of elasticity (see Figure 3–13 for the orientation of the rosettes). Table 4–8 also presents the principal stresses and direction of the major principal plane at each strain rosette location. The results presented in Table 4–8 show that the vertical stresses near the top of the web gap (gauge 30 on the east face and gauges 18 and 21 on the west face) are tensile on the east face (stiffener side) and compressive on the west face. Near the bottom of the web gap

43

(13 mm up from the bottom flange of the girder) the calculated east and west face vertical stresses were 63.2 MPa in compression (gauge 24) and 32.7 MPa in tension (gauge 15), respectively. The change from compression to tension along the height of the web gap on each face of the web indicates that the web gap region was in double curvature.

The web gap distortion was measured at joints 10, 11, 12, and 13. The measurements at Joint 11 were later found to be unreliable. Therefore, these measurements are not reported here.

At the maximum static load level (193 kN per actuator), the web gap distortion at Joint 13 was 0.09 mm. The measured web distortion was consistent with the observed beam and diaphragms displacements. This web distortion should give rise to tensile strains on the east face of the web at the top of the web gap and compressive strains on the east face at the bottom of the gap. The direction of the strains at Joint 13 are the same as those obtained from the strain measurements at Joint 11, since the diaphragm is on the same side of the web at both joints. The resulting distorted shape is similar to the distortion shown in the web gap of the girders shown in Figure 2–1. The web gap distortions at joints 10 and 12 were 0.12 mm and 0.16 mm, respectively.

Test Specimen 2

Figure 4–6 shows the normal strain distribution at midspan measured at a load level of 145 kN per actuator. The position of the neutral axis was found to be 827 mm on the east face of the girder and 821 mm on the west face. Again, these values are in good agreement with the position of the neutral axis (847 mm) determined in the field. The bottom fibre stress at mid-width of the flange was 47 MPa. The differential displacements due to the 145 kN actuator loads were similar to the differential displacements of the first girder and within 10% of the differential displacements determined from the analysis performed by Fraser *et al.* (2000), shown in Table 3–1.

A load of 188 kN in each actuator was required to obtain the required 62 MPa maximum bottom fibre stress. The displacements and the resulting differential displacements at each diaphragm position for this load level are listed in Table 4–9. At the maximum static

load level of 188 kN per actuator, the north and south girder end reactions were 168 kN and 167 kN, respectively. Table 4–10 summarises the diaphragm end support reactions calculated from the measured deformations at the maximum static load level. Equilibrium of forces is satisfied to within less than 2%, since the total reaction load is 371 kN and the total test load is 376 kN.

The measured web gap distortions at joints 10 and 13 were 0.21 mm and 0.11 mm, respectively. Once again, the measured distortions fit the theoretical model shown in Figure 2–1 since the top of the gap was being pulled towards the diaphragm and the bottom of the web gap region was restrained by the girder flange.

Test Specimen 3

Figure 4–7 shows the measured strains and linear regression lines from a static test performed on the third test specimen at 150 kN per actuator. The neutral axis position obtained from the strain gauges on the east and west faces of the girder web was 827 mm and 808 mm, respectively. The bottom fibre stress at the centre of the flange was calculated to be 48 MPa. The position of the neutral axis, the bottom fibre stress, and the differential displacements were in good agreement with the values obtained from the initial static tests performed on the first two test specimens.

Table 4–11 lists the displacements and the resulting differential displacements at each diaphragm position at 196 kN per actuator, required to achieve a midspan bottom fibre stress of 62 MPa. At this static load level, the north and south girder end reactions were measured to be 173 kN and 172 kN, respectively. Table 4–12 summarises the calculated diaphragm end support reactions at the maximum static load level. As for the previous specimens, equilibrium of forces is satisfied to within less than 2%.

The stresses in the web gap region at a load of 196 kN per actuator are presented in Table 4–13 for Joint 12, along with principal stresses and direction of the major principal plane at each strain rosette location. The stresses were obtained by multiplying the measured strains by the measured modulus of elasticity (see Figure 3–15 for the orientation of the rosettes). The strain data indicate strains that are consistent with

observed deformations. The web gap distortions at joints 10 and 13 were 0.14 mm and 0.11 mm, respectively. These distortion measurements were within the range of values obtained from the first two girders.

Test Specimen 4

Figure 4–8 shows the normal strain distribution at midspan measured at a static load level of 147 kN per actuator. The neutral axis positions were 828 mm and 806 mm, obtained from the strain gauges on the east and west face of the girder web, respectively. From extrapolation of the regression curves, the midspan bottom fibre stress was calculated as 47 MPa. The differential displacements due to the 147 kN actuator loads were in good agreement with the differential displacements from initial static tests of the first three specimens and those determined from the analysis presented by Fraser *et al.* (2000), shown in Table 3–1.

Table 4–14 lists the displacements and the resulting differential displacements at each diaphragm position at a load of 194 kN per actuator, which is the load required to develop a bottom fibre stress of 62 MPa. At the maximum static load level, the north and south girder end reactions were measured to be 169 kN and 171 kN, respectively. Calculated diaphragm end support reactions at the maximum static load level are presented in Table 4–15. Equilibrium of forces is satisfied again to within less than 2%.

The stresses in the web gap region at Joint 12 of specimen 4 are presented in Table 4–16. The stresses in the web gap region are higher than those in the first and third specimens because of the presence of stop holes and the proximity of the strain gauges to the stop holes (see Table 4–4 and Figure 3–15). At Joint 13, the web gap distortion was 0.12 mm.

Test Specimen 5

Figure 4–9 shows the normal strain distribution at midspan measured at a static load level of 152 kN per actuator. The neutral axis position obtained from the strain gauges on the east and west faces of the girder web was 820 mm and 794 mm, respectively. The bottom fibre stress at the centre of the flange was determined to be 47 MPa. The position of the neutral axis, the bottom fibre stress, and the differential displacements are representative

of the values obtained from the initial static tests performed on the other test specimens. Table 4–17 presents the span lengths of the diaphragm end supports and the deflections and differential displacements at each diaphragm position.

At the maximum static load level, the girder end reactions were measured as 128 kN and 130 kN for the north and south reactions, respectively. The calculated loads in the spring supports at the ends of the diaphragm members are summarised in Table 4–18 and equilibrium of forces is satisfied to within less than 3%. It should be noted that the maximum static load level for this final specimen was less than the other four specimens because this specimen was tested at a stress range of 35 MPa, as compared to 50 MPa for the previous specimens.

The stresses in the web gap region at Joint 12 are presented in Table 4–19, along with principal stresses and direction of the major principal plane at each strain rosette location (see Figure 3–14 for the orientation of the rosettes). The maximum value of major principal stress determined from the strain rosettes (gauges 16 through 18) was 64.1 MPa, which is approximately equal to the maximum major principal stress obtained from at Joint 12 of specimen 1 tested by Fraser *et al.* (2000). Out-of-plane displacement measurements were not available for this test specimen.

Static tests, similar to the initial static tests, were repeated before repairs were mounted on the first four specimens. The results of the tests are summarized in Appendix A. No significant change in behaviour was observed in any of the specimens.

Comparison of Web Gap Stresses

Using the major principal stresses from specimen 5 and from Fraser *et al.* (2000) for the gauges at the top of the web gap on the stiffener side of the web yields an average major principal stress of 55 MPa for a 47 MPa midspan bottom fibre stress. Test specimens 1 and 3 yield an average major principal stress of 76 MPa for a bottom fibre stress of 62 MPa. Therefore, a 32% increase in midspan bottom fibre stress results in a 39% increase in web gap stress. For the gauges at the bottom of the web gap a 34% increase in the average major principal stress results from a 32% increase in midspan bottom fibre

stress. Considering that the amount of cracking in each specimen varied and that differences in the measured web gap stresses result from small variations in the mounting position of the strain rosettes, the increase in measured web gap stress is more or less the same as the increase in bottom fibre stress. The major principal stresses presented are not the maximum principal stresses in the web gap. The maximum stresses in the web gap would occur at the web-to-flange and web-to-stiffener junctions. Although the strain gauges were mounted close to these locations, they were not mounted at the junctions between plates.

4.1.3 Fatigue Testing

Fatigue testing was started after it was established that the condition of each test specimen was representative of field conditions. As explained in Chapter 3, the maximum and minimum actuator loads and the cycling frequency had to be adjusted to achieve the desired stress range without reversal of stress. After the cyclic frequency and loads were set, the displacements and resulting end displacements of the diaphragms were checked to ensure that they remained unchanged from those determined during initial static tests. In each test, the end displacements of the diaphragms were observed to be similar to the static values presented in Tables 4–6, 4–9, 4–11, 4–14, and 4–17.

The fatigue crack growth rates and the location and orientation of the observed fatigue cracks for each of the test specimens are presented below. During each test, multiple fatigue cracks were observed in the girder web at the diaphragms located between the actuators (Joints 10 through 13). Only the results for the significant cracks are presented in this chapter. The use of "significant cracks" and "significant crack length" refers to cracks that approach a length of about 150 mm. The crack growth rate curves for the shorter cracks are presented in Appendix B.

Test Specimen 1

Fatigue testing of the first specimen was conducted at a frequency of 1.45 Hz. The maximum and minimum actuator loads were established as 215 kN and 10 kN, respectively, which corresponds to bottom fibre stresses of 62 MPa and 12 MPa.

Although the fatigue crack at Joint 12 had been repaired by stop hole drilling, the crack initiated past the stop holes at approximately 600 000 load cycles.

Figure 4–10 shows a plot of crack length versus load cycle at Joint 12 measured on the east and west faces of the web. It should be noted that the first point on each of the crack growth curves corresponds to the last inspection where no cracks were detected. At about 600 000 cycles, it was observed that the crack at Joint 12 began to propagate past the drilled stop holes and up the web on the west face of the girder. This crack is referred to as the "upward" crack. (An upward crack is a crack that initiates from the top of a stop hole and continues up the web of the girder, while a downward crack is one that initiates from the bottom of a stop hole and continues down the web of the girder towards the bottom flange.) Up to approximately 1.5 million load cycles the upward crack was a part-through-thickness crack. The crack growth rate at Joint 12 determined to be about 45×10^{-6} mm/cycle. This was obtained from a from a regression analysis of the first portion of the crack length versus load cycle plots, i.e. from 0.6 to 2.2 million load cycles. At about 1.5 million cycles, the crack at Joint 12 became a through-thickness crack. From a regression analysis, it was found that the crack growth rate had increased to approximately 85×10^{-6} mm/cycle over the final 600 000 load cycles. A comparison of the crack growth rates measured from the east and west sides of the upward crack indicates that the rates are similar, but the east side of the crack is shorter than the west side of the crack. This confirms the observations of Fraser *et al.* (2000) that the crack fronts were inclined through the web thickness. A through-thickness crack was observed below a stop hole at Joint 12 at 1.7 million cycles. Figure 4–10 shows the length of this downward moving crack on both faces of the web to be equal. The crack growth rate of the downward crack was 42×10^{-6} mm/cycle. The orientation of the fatigue cracks on the west face of Joint 12 is shown in Figure 4–11.

The crack lengths reported in Figure 4–10 were measured from the nearest edge of the stop holes. The origin of the fatigue cracks past the stop hole is indicated in Figure 4–11 as the "0" position. At 2.8 million cycles, the upward crack had grown to 152 mm on the west face of the web. Since the crack length met the significant crack length criterion outlined in Section 3.5, fatigue testing was stopped and low temperature tests were

performed. At 2.8 million cycles the downward crack had grown 15 mm into the bottom flange on both sides of the web, resulting in an overall length of approximately 65 mm.

Test Specimen 2

The maximum and minimum actuator loads and the cyclic frequency for this specimen were the same as for the first test specimen. At 1.2 million cycles a fatigue crack was detected at Joint 10. The crack did not become a through-thickness crack and the crack growth rate at the time it was detected was only about 17×10^{-6} mm/cycle, as shown in Figure 4–12. From 3.6 to 4.7 million cycles the crack growth rate was about 23×10^{-6} mm/cycle. At 4.7 million cycles the part-through-thickness crack had grown to approximately 95 mm. Figure 4–13 shows the location of the crack on the west face of Joint 10. Because of the amount of time this test had run, it was decided to perform a low temperature test and then to repair the crack at Joint 10.

A new crack was observed emanating from the stop hole at Joint 12 at 3.6 million cycles. At approximately 4.6 million cycles the crack became a through-thickness crack, as shown from the origin of the crack growth curves presented in Figure 4–14. The length of the crack measured on the west face remained longer than the length of the crack measured on the east face throughout the fatigue test. This illustrates that the crack front was not at a right angle to the web surface. From 3.6 to 6.1 million load cycles, the crack growth rate measured on the west face was determined to be about 30×10^{-6} mm/cycle, whereas the growth rate measured on the east face was approximately 40×10^{-6} mm/cycle. After 6.1 million cycles the crack growth rate was 77×10^{-6} mm/cycle on both faces of the web and the west side of the crack remained about 10 mm longer than the east side of the crack.

At approximately 6.1 million cycles, a through-thickness crack was observed propagating downwards at Joint 12. Figure 4–14 shows that the length of this downward crack and the crack growth rate (77×10^{-6} mm/cycle) on both faces of the web are equal. Figures 4–15 and 4–16 show the orientation of all cracks at Joint 12.

At 6.8 million cycles the upward crack on the west side of the web was 135 mm long and 130 mm on the east side of the web. The downward crack grew 5 mm into the bottom flange on both sides of the web, reaching an overall length of approximately 57 mm. The test was stopped at this point since 2.1 million load cycles had now been applied to the specimen after the repair of Joint 10.

A possible reason why the cracks in this girder required a relatively long time to propagate compared to cracks in the other girders from this test program is that the steel from girder 2 was different than the steel from the other girders (see Section 4.2). The possibility of an overload causing the slow growth rate is not plausible because an overload typically affects the growth rate over a short extension of the crack from the time the overload is applied (Broek, 1989). The crack would eventually grow past the area affected by the overload and the growth rate would increase.

Test Specimen 3

The maximum and minimum actuator loads were set to 227 kN and 9 kN, respectively, at a cyclic frequency of 1.6 Hz. This corresponded to maximum and minimum bottom fibre stresses of 62 MPa and 12 MPa.

As shown in Table 4–3, a crack was detected along the weld at the bottom of the stiffener at Joint 12 where no stop holes had been drilled. The approximate crack initiation site is identified in Figure 4–17 as the "0" position. A fatigue crack was detected at one million load cycles. Cracks were observed to be moving both up and down the web from the bottom of the stiffener. Figure 4–18 shows the crack length versus load cycle plots for the crack at Joint 12. The crack propagation curves indicate that the crack became a through-thickness crack between 1.6 million and 1.9 million cycles. At 1.6 million cycles the crack had not surfaced on the east face of the web, but at 1.9 million cycles the east side of the crack had already reached a length of 32 mm. Therefore, the zero position for the east side of the crack, as shown in Figure 4–19, was taken as halfway between the bottom and top crack tips at 1.9 million cycles. The crack growth rate of the west side of the upward moving crack at Joint 12 increased from a crack growth rate of approximately 45×10^{-6} mm/cycle to approximately 200×10^{-6} mm/cycle, the same rate as on the east

face. Figure 4–18 shows that the crack growth on the west and east sides of the downward crack was similar. The crack growth rate of the downward crack was approximately 35×10^{-6} mm/cycle.

Test Specimen 4

Test specimen 4 was tested at a bottom fibre stress range of 50 MPa, corresponding to a maximum stress of 62 MPa and a minimum stress of 12 MPa. Figure 4–20 shows crack length versus load cycle plots for the cracks at joints 11 and 13. A fatigue crack was detected at the stop hole on the east face of the web at Joint 11 after approximately 800 000 load cycles. The crack remained a part-through-thickness crack throughout the test. The crack growth rate increased from an initial rate of about 45×10^{-6} mm/cycle to 125×10^{-6} mm/cycle before the joint was repaired. At 1.4 million cycles another crack was detected at Joint 13. The crack growth rate remained more-or-less constant at 42×10^{-6} mm/cycle until the joint was repaired. (The crack growth after repairs will be discussed in Section 4.1.5.) The crack at Joint 13 also remained a part-through-thickness crack. Figures 4–21 and 4–22 show the location of all the cracks at Joints 11 and 13, respectively.

A repair of the fatigue crack at Joint 11 was performed at 2.4 million cycles. At that time the crack had reached a length of 125 mm and was progressing at a relatively fast rate, as can been seen from Figure 4–20. The fatigue crack at Joint 13 was repaired 100 000 cycles later.

Test Specimen 5

Test specimen 5 was tested at a bottom fibre stress range of 35 MPa, corresponding to a maximum stress of 45 MPa and a minimum stress of 12 MPa. In order to assess the effectiveness of a fatigue crack repair that combined hole drilling and web gap closure, repair angles were bolted to the test specimens to close the web gap at the locations where repairs by stop hole drilling had been performed in the field and in the laboratory. This simulated the condition where both repairs would typically be performed at the same

time. Since the fatigue test of the fifth specimen was conducted entirely in the repaired condition, this test is discussed only in Section 4.1.5.

Comparison of Fatigue Test Results

The following features are common to the first, third, and fourth test specimens:
1. All test specimens were tested at a stress range of 50 MPa.
2. The initial crack growth rate was approximately 50×10^{-6} mm/cycle;
3. The crack growth rate increased to approximately three times the initial rate after about 2.2 million load cycles;
4. The significant crack length of 150 mm (chosen repair criterion) was not reached until after 2.6 million load cycles.
5. The cracks grew along the toe of the web-to-stiffener fillet weld.
6. A comparison of the test results at a stress range of 50 MPa with test results presented by Fraser *et al.* (2000) for a stress range of 35 MPa indicates that 1) the crack growth rates at a bottom fibre stress range of 50 MPa were approximately twice the crack growth rates at a bottom fibre stress range of 35 MPa, and 2) the significant crack length was reached approximately 1.5 million cycles sooner than was observed by Fraser *et al.* (2000).

Differences in the behaviour of the cracks in the first, third, and fourth test specimens were also observed. The largest crack in the fourth test remained a part-through-thickness crack during testing, whereas the largest cracks in the first and third girders became through-thickness cracks at approximately the same number of load cycles after crack initiation was observed. Another difference between specimen 4 and specimens 1 and 3 is that the first and third specimens had cracks that propagated from the bottom of a stop hole down towards the bottom flange of the girder, while the fourth girder did not. The downward cracks in the first and fourth test specimens grew at essentially the same rate. The fourth specimen also differed from the other two specimens in that a second large crack formed in the girder at Joint 13. This crack propagated at the same rate as the one at Joint 11.

A comparison of the results of the first four tests shows that there were a few differences in the behaviour of specimen 2 compared to the other test specimens. These differences are outlined below.

1. The initial crack growth rate at Joint 10 was approximately three times slower than the initial crack growth rate observed in the other three tests even though the differential displacement at this joint was similar to the differential displacements at the joints with significant cracks in the other specimens;

2. The crack that developed at Joint 12 behaved in a similar manner to the significant cracks in the other three specimens. However, the crack re-initiated at the stop hole after 3.5 million load cycles as compared to observed crack re-initiation after less than one million load cycles in the other specimens.

These differences in the second test specimen can be attributed to the difference in the material properties between this girder and the remainder of the girders, as mentioned previously. Near the end of the fatigue test, after repair angles had been installed, a crack was detected along the bottom flange-to-web weld at the north end of the girder. The crack had initiated at the bearing stiffener and was moving southwards along the weld. This crack is not believed to have had any effect on the test results.

Some similarities in crack growth behaviour in all four specimens were observed. Although not all significant fatigue cracks occurred at joints where repair holes had been drilled, they did propagate from stop holes in three of the four girders. This confirms the observation by Fraser *et al.* (2000) that hole drilling is not effective at arresting distortion-induced fatigue cracks in this type of girder. Crack initiation and propagation was observed to be the result of combined Mode I and Mode III loading.

4.1.4 Fatigue Crack Behaviour at Low Temperature

Low temperature static and cyclic tests were performed before repair of the fatigue cracks in order to assess the stability of fatigue cracks at low temperature. Low temperature tests were performed on Joint 12 of specimen 1 and on Joint 10 of specimen 2 once the largest fatigue cracks approached a length of about 150 mm. The loading and temperature conditions used during each low temperature test are summarised in Table 4–20. The

cracks in both specimens remained stable during the low temperature tests. This was expected since the tests performed by Fraser *et al.* (2000), which were similar to the ones performed in this testing program, indicated that similar fatigue cracks remained stable at extreme temperature conditions and extreme loading conditions.

Low temperature tests were performed at Joint 12 on the third specimen before the fatigue cracks were repaired. Before the two static low temperature tests were performed, the temperature in the chamber was maintained near –50°C while fatigue testing was performed at the same load range as was used for the room temperature fatigue tests. Fatigue testing was continued at low temperature for 6 hours, and the upward crack on the east face of the web at Joint 12 was monitored during testing. (The west side of the upward crack and both sides of the downward crack could not be monitored due to the configuration of the chamber.) The fatigue crack propagated approximately 10 mm during the low temperature fatigue test, which corresponds to an average crack growth rate of 286×10^{-6} mm/cycle. This rate is slightly greater than the room temperature crack growth rate of 200×10^{-6} mm/cycle, which was recorded just before the low temperature test. Both the 145 mm long upward crack in the girder web and the downward crack that extended to the flange-to-web junction remained stable under the two static low temperature tests.

4.1.5 Repair of Test Specimens

Except for the first test specimen, all test specimens were repaired using a combination of bolted angles to bridge the web gap opening and stop hole drilling. The effectiveness of a number of repair strategies was assessed. The repairs were performed as outlined in Chapter 3 once the static tests were completed and after the fatigue cracks had reached the desired length. After completing the repair of the specimens, a static test was performed at the maximum initial static load in order to determine the effectiveness of the bridging angles at preventing web gap distortions. Fatigue testing was then resumed under the same loading conditions as the initial fatigue test. Once it was determined that the repair was effective or ineffective, fatigue testing was concluded and a final static test was performed.

Test Specimen 2

A repair angle, consisting of a 12.5 mm bent plate, was connected to the girder transverse stiffener and to the bottom flange of the girder at Joint 10, as shown in Figures 4–23 and 4–24. The orientation and dimensions of a typical repair angle connecting the stiffener to the bottom flange are shown in Figure 4–23, whereas Figure 4–24 shows the actual repair at Joint 10 of specimen 2. It should be noted that the repair strategy was to prevent web gap distortion and stop holes were not drilled at the tips of the existing crack. The repair had a significant effect on the differential displacement and the web gap distortion at Joint 10. Table 4–21 shows the decrease of differential displacement and web gap distortion as compared to the conditions before repair. In this case, the repair angle was effective in eliminating the out-of-plane displacement in the web gap. The decrease in differential displacement was mainly due to an increase in rotational stiffness at the diaphragm-to-girder connections. The decrease in diaphragm rotation was accompanied by an increase in diaphragm end support reaction.

Fatigue testing of the specimen was resumed after the static test was complete. Fatigue testing was continued for 2.1 million cycles after Joint 10 was repaired. No crack growth at Joint 10 was observed during the load cycles applied after repair. It should be noted that no out-of-plane displacement at Joint 10 was visible during the fatigue testing after repair; however, a small amount of crack opening, from Mode I loading, was visible with a magnifying glass at the base of the crack, near the stop hole. Since no fatigue crack growth was observed at Joint 10, the repair was considered effective and fatigue testing was stopped 2.1 million cycles after repair.

At the end of the fatigue test a final static test was performed. The differential displacement and the web gap distortion, –0.54 mm and 0.00 mm, respectively, at Joint 10 remained relatively unchanged from the values obtained after the repair was made (see Table 4–21). Therefore it was concluded that the repair remained effective in stiffening the web gap region. The lack of crack growth after the repair of the second girder, as compared to the next two girders, may also be due to two other factors. The first is the fatigue crack at the time of repair of Joint 10 was not a through-thickness

crack. A possible second factor is the differences in the material properties of the girder web compared to the other girders (see Section 4.2 for details).

Test Specimen 3

Figure 4–25 shows the repair angle that was attached to the stiffener and bottom flange of the girder at Joint 12. This repair angle was 45 mm wider than the repair angle used for test specimen 2; otherwise this repair angle was similar in orientation as shown in Figure 4–23. The length of the repair angle was increased to investigate the effectiveness of a wider angle, protruding past the edge of the bottom flange. As observed in specimen 2, the repair at Joint 12 in this specimen had a significant effect on the differential displacement of the diaphragm and the web gap distortion. Table 4–22 presents a comparison of the differential displacements and the web gap distortions before and after repair of Joint 12. After the repair, the vertical displacement at the end of the diaphragm increased significantly, thereby causing a decrease in the differential displacement at Joint 12. The decrease in web gap distortion at Joint 12 is documented in Table 4–22. The repair was effective in decreasing the web gap distortion at Joint 12. Compared to the repair performed on the second test specimen, there was no apparent difference in the effectiveness of the repair using a wider repair angle.

Although the repair angle had considerably reduced the web gap distortion, fatigue crack growth was observed after only 100 000 load cycles after the repair angle was installed. Figure 4–18 shows the crack length versus load cycle plot for the cracks at Joint 12. The repair had no effect on slowing down either the upward or downward cracks, which continued growing under the in-plane cyclic stresses. A large increase in crack growth rate, from approximately 35×10^{-6} mm/cycle to 350×10^{-6} mm/cycle, of the downward crack occurred when the crack reached the bottom flange and became a through-thickness crack. Fatigue testing was stopped 400 000 load cycles after the repair since the repair was not effective in stopping the crack and the crack was propagating quickly through the bottom flange.

A static test was performed after fatigue testing was completed. The differential displacement and the web gap distortion did not change significantly from the values measured prior to fatigue testing the repaired specimen (see Table 4–22).

Test Specimen 4

The repair scheme of this specimen differed from the previous repairs in that stop holes were drilled the crack tips before mounting the repair angles and two joints locations were repaired. At Joint 11 a repair angle was bolted to the web and flange of the specimen, as shown in Figure 4–26. Joint 13 was repaired using an angle bolted to the stiffener and bottom flange as shown in Figure 4–23 and drilling a 16 mm diameter stop hole at the tip of the large fatigue crack that propagated up from the existing stop hole. A 16 mm diameter stop hole was drilled at the fatigue crack tip at Joint 11, 200 000 load cycles after the repair was installed at that joint. The size of the stop hole was relatively small because of the restricted access at the joints. The restricted access meant that the holes had to be drilled using a hand drill. Therefore, both stop holes were approximately half the diameter predicted using Equation 2–2. The large stop hole diameter (30 mm) required according to Equation 2–2 reflects the large crack length present at the time of repair. Figures 4–27 and 4–28 show the actual repairs made at each joint.

A static test was performed after the repair at Joint 13 was completed. Table 4–23 presents a comparison of the differential displacements and the web gap distortions before and after the repairs. As mentioned previously, the LVDT measurements at Joint 11 were not reliable. However, based on the decrease in web gap distortion and differential displacement at Joint 13, the repair appeared to have adequately stiffened the web gap region.

Fatigue testing of the specimen resumed under the same loading conditions as were used in the fatigue test before the repairs were made. Fatigue propagation past the stop holes was observed at both joints. At Joint 13 a new crack initiated past the 16 mm stop hole 800 000 cycles after the new stop hole was drilled at that joint. Similarly, a fatigue crack initiated at Joint 11 one million cycles after the 16 mm stop hole was drilled at Joint 11. Figure 4–20 shows the crack length versus load cycle plots for the cracks at joints 11 and

13. Crack growth rate calculations indicated that the combination of the repair angle and the stop hole slowed down the fatigue crack growth rate from 125×10^{-6} mm/cycle to 33×10^{-6} mm/cycle at Joint 11. The fatigue crack growth rate at Joint 13 also slowed down to 33×10^{-6} mm/cycle after the repair was made. The fatigue crack at Joint 13 became a through-thickness crack 1.4 million cycles after the repair was made, but did not join the pre-existing stop hole as shown on the back surface of the weld in Figure 4–29. Fatigue testing was concluded 2.1 million cycles after the repair at Joint 11 was performed (about 4.5 million cycles from the start of the test on this specimen). The crack at Joint 11 had reached a length of 202 mm, approximately 75 mm greater than the length at the time of repair. The crack at Joint 13 grew also by approximately 75 mm after repair, namely, to a total length of 142 mm.

A final static test on the test specimen indicated that the web gap distortion remained relatively unchanged during the cyclic loading applied after the repair (see Table 4–23). However, the differential displacement did increase from the value obtained before repair. This is likely due to the presence of a much larger fatigue crack, which decreased the stiffness of the web at the diaphragm.

Test Specimen 5

Repair of the test specimen consisted of a combination of hole drilling and gap bridging in order to try to stop both Mode I and Mode III load action. Repair of joints 10, 11, 12, and 13 was performed at the beginning of the test to investigate the effectiveness of a typical field repair that would consist of drilling a hole at the crack tip and bridging the web gap. Before any repair angles were attached to the girder, 24 mm diameter stop holes were drilled at the observed fatigue crack tips at joints 11, 12, and 13, none of which had been field repaired (see Table 4–5). The tips of the fatigue cracks were found visually using the magnifying glass during the initial load cycling period. The stop holes were drilled with a portable drill press. No cracks were detected past the existing drilled stop holes at Joint 10. Repair angles were then attached to the stiffener and bottom flange of the girder at joints 10 and 13, similar to Figure 4–23, whereas at joints 11 and 12 the repair angles were attached to the web and bottom flange. The repair angle at Joint 11

was similar to Figure 4–26, whereas Figure 4–30 illustrates the dimensions and orientation of the repair angle at Joint 12. Figures 4–31 to 4–36 show the repair angles at the repaired joints from test specimen 5.

A static test was performed after all repairs were in place. Table 4–24 presents the comparison of the differential displacements before and after the repairs. As mentioned previously, the web gap distortion measurements were not available for this test specimen. The differential displacements did decrease by 0.06 mm, 0.04 mm, and 0.09 mm for joints 11, 12, and 13, respectively, whereas Joint 10 remained relatively unchanged (0.02 mm increase). The large reduction in differential displacement at Joint 13 can be attributed to the presence of a through-thickness crack between the stop holes (see Table 4–5). The decrease in differential displacements illustrates the effectiveness of the repair angles at reducing the web gap distortion.

Less than 200 000 load cycles after fatigue testing was started, fatigue cracks were detected past the laboratory drilled stop holes at Joint 11 and at Joint 12. These were along the toe of the web-to-stiffener weld. The crack at Joint 11 had propagated 65 mm from the stop hole on the east face of the web, as shown in Figure 4–33, and on the west face of the web at Joint 12 a crack had propagated approximately 35 mm from the north stop hole, as can be seen in Figure 4–35. Figures 4–33 and 4–35 show the fatigue cracks at the end of testing. Since the cracks were quite long when first detected past the stop holes, it is suspected that the stop holes missed the actual crack tips.

Fatigue testing was continued for 3.5 million cycles after the repairs were made. No fatigue crack propagation was observed past the stop holes at Joints 10 and 13. The 65 mm long crack at Joint 11 had no significant crack growth over the 3.5 million cycles. As observed in the previous specimens, some "working" of the cracks due to Mode I loading was observed. At Joint 12 a fatigue crack was observed past the south stop hole after 2.1 million cycles. However the crack was approximately 8 mm long when first observed and only grew 3 mm over the next 600 000 cycles and no significant crack growth was observed over the remaining 800 000 cycles to fatigue testing completion. A possible explanation for the lack of significant fatigue crack growth after the initial crack

growth is that the crack tip had propagated into an area of lower in-plane stress, since the in-plane stress decreases with height above the bottom flange. This did not occur in the previous specimens because the fatigue cracks at the time of the repair were large. The initial 35 mm crack detected at the start of the test at the north stop hole of Joint 12 grew to a length of 50 mm after 2.1 million cycles, but crack growth afterwards was the same as the crack south of the stiffener. Therefore, the initial observed length of 35 mm might have been incorrect.

A final static test was performed at the conclusion of fatigue testing. The differential displacements remained relatively unchanged except for a 0.09 mm increase at Joint 10. The combination of drilling stop holes at the crack tip and attaching repair angles once fatigue cracking is noticed is significantly more effective than the repair angles attached after the fatigue cracks have propagated to a significant length. Both repair angles, the one connected to the stiffener and the bottom flange as well as the angle connected to the web and the bottom flange, appeared adequate in decreasing the amount of fatigue crack growth past the stop holes, but only the ones bolted to the stiffeners were found to be effective at stopping crack growth.

4.2 Ancillary Tests

Tension coupon tests were performed on material obtained from the web of the girders. Table 4–25 shows the results obtained from the two coupons that were tested from each girder. The variation of yield and ultimate strength within each girder is small; however, there is a significant difference in yield and ultimate strength between girder 2 and the rest of the girders. The as-built drawings for the bridge specify CSA G40.8 Grade B (CSA, 1960) steel, which has nominal yield strength of 276 MPa (40 ksi), for the girder webs. Girders 1, 3, 4, and 5 have mean yield strengths of approximately 303 MPa that is consistent with the mean yield strength of 315 MPa typical of CSA G40.8 steel. However, girder 2 has a yield strength of 263 MPa that is consistent with the mean yield strength of 265 MPa typical of CSA G40.5 (CSA, 1950).

Charpy V-notch (CVN) impact tests were performed on material obtained from the web of the test girders near the location of the critical fatigue cracks. The results of the CVN

impact tests are presented in Table 4–26 and Figure 4–37 shows the appearance of the fracture surface of all the CVN specimens. The tests were conducted at three different temperatures, varying from room temperature to –50°C. Both the energy absorbed and the percent shear fracture are reported in the table. The minimum energy absorption requirement set by the American Railway Engineering Association is 34 J at various test temperatures down to –25°C, measured using full-size specimens. The equivalent energy absorption requirement for a three-quarter sized specimen is 26 J, as specified by ASTM A370-97a. As shown in Table 4–26 the specimens from the first four girders, which were three-quarter sized specimens, met this requirement even at the –50°C test temperature. The results of the CVN impact tests and the fracture surface of the specimens for girder 5 indicate the possibility that the CVN specimens were made with the notch perpendicular to the direction of the notch in the other specimens. The notch in the specimens from girder 5 appears to be parallel to the grain of the steel, whereas the notch in the other specimens appears to be perpendicular to the steel grain (Figure 4–37). It should be noted that girder 2 shows a large scatter in the measured CVN values. The source of this large variability is unknown.

4.3 Examination of Fatigue Crack Surfaces

Fatigue crack surfaces from each test specimen were examined with a low magnification stereomicroscope and a scanning electron microscope. The objectives of these examinations were to establish the origin of the fatigue cracks, to determine whether there were any unusual features on the crack surfaces, and to assess whether or not the crack tips had been missed when the stop holes were drilled.

The amount of corrosion on the fatigue crack surface from specimen 1 was typical for all specimens, as shown at high magnification in Figure 4–38. Significant amounts of corrosion were observed at the crack initiation sites of the upward cracks near the edge of the stop holes in specimens 1 through 4. At some distance from the crack origin, the crack surface was virtually free from corrosion products. On the other hand, little corrosion was found on the entire surface of the downward cracks from specimens 1 and 2. This suggests that, although the upward cracks were not observed past the stop holes

until more than 600 000 load cycles were applied, cracks were present at the edge of the stop holes before testing started. The corrosion on the upward crack surfaces and the friction, caused by the rubbing of the crack surfaces, obscured most fatigue striations. Typical fatigue striations on the downward fatigue crack surface of test specimen 1 are shown in Figure 4–39.

Examinations of fatigue crack surfaces propagating from stop holes confirmed that the fatigue cracks had initiated at the edge of the stop holes except for the examination of the upward crack surface at Joint 10 in the second specimen, shown in Figure 4–40. Figures 4–41 and 4–42 are close-up views of two locations of the crack surface shown in Figure 4–40. The ridge observed 1.5 mm from the edge of the stop hole might have been the crack tip when the stop hole was drilled. The significant corrosion observed below the ridge and the fact that the ridge is parallel to the edge of the stop hole and through most of the thickness of the web are evidence that the stop hole was drilled below the crack tip. When a fatigue crack starts from a hole, it is typical that the crack origin would be either at the corner (edge of the hole at the surface of the plate) or at a flaw along the edge of the hole. In this case, none of these features were present, indicating that the crack has grown a good distance from its origin, becoming a near through-thickness crack. The initiation site of a second crack was found approximately 11 to 12 mm from the edge of the stop hole, as shown in Figures 4–40 and 4–42. The second initiation site suggests that a surface flaw, possibly due to an imperfection caused by the stiffener-to-web weld, was the cause of the initiation at this location.

The origin of the significant fatigue crack at Joint 12 in the third specimen as shown in Figure 4–17, where no stop holes were drilled, was confirmed by the examination of the crack surface. No evidence was found on the crack surfaces taken from specimens 4 and 5 to indicate whether or not the laboratory drilled stop holes missed the crack tips.

Table 4–1

Results of Visual Inspection of Test Specimen 1

Joint**	Distances to Stop Holes (mm) (see Figure 4–1)				Comments
	L1	L2	L3	L4	
9	N/A*	N/A	N/A	N/A	No apparent cracking.
11	N/A	N/A	N/A	N/A	No apparent cracking.
13	63	58	17	10	*East Face*[†]: crack extends across bottom of stiffener similar to cracks in Figure 4–2. *West Face:* no apparent cracking
15	N/A	N/A	N/A	N/A	No apparent cracking.
8	N/A	N/A	N/A	N/A	Small crack in weld at bottom of transverse stiffener.
10	46	46	5	5	*West Face:* crack extends across bottom of stiffener similar to cracks in Figure 4–2. *East Face:* crack extends laterally across holes similar to crack shown in Figure 4–3.
12	42	45	7	-6	*West Face:* crack extends across bottom of stiffener similar to cracks in Figure 4–2. *East Face:* no apparent cracking.
14	43	43	10	-6	*West Face:* crack extends across bottom of stiffener similar to cracks in Figure 4–2 *East Face:* no apparent cracking.

* N/A indicates that no holes were drilled at the joint.

** Refer to Figure 3–4 for joint location.

[†] The east face of odd numbered joints is on the web surface on the diaphragm side and vice-versa for even numbered joints.

Table 4–2

Results of Visual Inspection of Test Specimen 2

Joint**	L1	L2	L3	L4	Comments
	Distances to Stop Holes (mm) (see Figure 4–1)				
9	N/A*	N/A	N/A	N/A	No apparent cracking.
11	32	29	7	11	*East Face†:* crack extends across bottom of stiffener similar to cracks in Figure 4–2. *West Face:* no apparent cracking
13	47	50	8	-2	*East Face:* crack extends across bottom of stiffener similar to cracks in Figure 4–2. *West Face:* crack extends laterally across holes similar to crack shown in Figure 4–3.
15	N/A	N/A	N/A	N/A	No apparent cracking.
8	N/A	N/A	N/A	N/A	No apparent cracking.
10	51	54	2	6	*West Face:* crack extends across bottom of stiffener similar to cracks in Figure 4–2. *East Face:* crack extends laterally across holes similar to crack shown in Figure 4–3.
12	45	48 (69)***	17	15 (8)	*West Face:* crack extends across bottom of stiffener similar to cracks in Figure 4–2. *East Face:* crack extends laterally across holes similar to crack shown in Figure 4–3.
14	56	54	17	4	*West Face:* crack extends across bottom of stiffener similar to cracks in Figure 4–2. *East Face:* no apparent cracking.

* N/A indicates that no holes were drilled at the joint.

** Refer to Figure 3–4 for joint location.

*** Dimensions in brackets indicate that a third hole was drilled near the web gap, similar to Figure 4–4.

† The east face of odd numbered joints is on the web surface on the diaphragm side and vice-versa for even numbered joints.

Table 4–3

Results of Visual Inspection of Test Specimen 3

Joint**	Distances to Stop Holes (mm) (see Figure 4–1)				Comments
	L1	L2	L3	L4	
9	52 (59)***	53	-6 (-4)	2	*East Face*†: crack extends across bottom of stiffener similar to cracks in Figure 4–2. *West Face:* no apparent cracking.
11	55	46 (48)	22	13 (26)	*East Face:* crack extends across bottom of stiffener similar to cracks in Figure 4–2. *West Face:* crack extends laterally across holes similar to crack shown in Figure 4–3.
13	N/A*	N/A	N/A	N/A	Small crack in weld at bottom of transverse stiffener.
15	N/A	N/A	N/A	N/A	No apparent cracking.
8	N/A	N/A	N/A	N/A	No apparent cracking.
10	36	42	4	7	*West Face:* crack extends across bottom of stiffener similar to cracks in Figure 4–2. *East Face:* crack extends laterally across holes similar to crack shown in Figure 4–3.
12	N/A	N/A	N/A	N/A	Small crack in weld at bottom of transverse stiffener.
14	40	31	11	-3	*West Face:* crack extends across bottom of stiffener similar to cracks in Figure 4–2 *East Face:* no apparent cracking.

* N/A indicates that no holes were drilled at the joint.

** Refer to Figure 3–4 for joint location.

*** Dimensions in brackets indicate that a third hole was drilled near the web gap, similar to Figure 4–4.

† The east face of odd numbered joints is on the web surface on the diaphragm side and vice-versa for even numbered joints.

Table 4–4

Results of Visual Inspection of Test Specimen 4

Joint**	Distances to Stop Holes (mm) (see Figure 4–1)				Comments
	L1	L2	L3	L4	
9	N/A*	N/A	N/A	N/A	Small cracks in welds at bottom of transverse stiffener.
11	34	32	2	1	*East Face*[†]*:* crack extends across bottom of stiffener similar to cracks in Figure 4–2. *West Face:* crack extends laterally across holes similar to crack shown in Figure 4–3.
13	32	30	6	7	*East Face:* crack extends across bottom of stiffener similar to cracks in Figure 4–2. *West Face:* no apparent cracking
15	N/A	N/A	N/A	N/A	No apparent cracking.
8	N/A	N/A	N/A	N/A	No apparent cracking.
10	N/A	N/A	N/A	N/A	Small crack in weld at bottom of transverse stiffener.
12	31	53	3	1	*West Face:* crack extends across bottom of stiffener similar to cracks in Figure 4–2. *East Face:* no apparent cracking.
14	39	47	10	-5	*West Face:* crack extends across bottom of stiffener similar to cracks in Figure 4–2 *East Face:* crack extends laterally across holes similar to crack shown in Figure 4–3.

* N/A indicates that no holes were drilled at the joint.

** Refer to Figure 3–4 for joint location.

[†] The east face of odd numbered joints is on the web surface on the diaphragm side and vice-versa for even numbered joints.

Table 4–5

Results of Visual Inspection of Test Specimen 5

Joint**	Distances to Stop Holes (mm) (see Figure 4–1)				Comments
	L1	L2	L3	L4	
9	N/A*	N/A	N/A	N/A	No apparent cracking.
11	**48***	**39**	**1**	**3**	Small crack in weld at bottom of transverse stiffener.
13	38	41	7	13	*East Face*[†]*:* crack extends across bottom of stiffener similar to cracks in Figure 4–2. *West Face:* crack extends laterally across holes similar to crack shown in Figure 4–3.
15	N/A	N/A	N/A	N/A	No apparent cracking.
8	N/A	N/A	N/A	N/A	No apparent cracking.
10	**47**	**50**	**0**	**1**	Small crack in weld at bottom of transverse stiffener.
12	**46**	**43**	**-1**	**0**	Small crack in weld at bottom of transverse stiffener.
14	34	43	0	7	*West Face:* crack extends across bottom of stiffener similar to cracks in Figure 4–2. *East Face:* crack extends laterally across holes similar to crack shown in Figure 4–3.

* N/A indicates that no holes were drilled at the joint.

** Refer to Figure 3–4 for joint location.

*** Dimensions in bold indicate that the stop hole was drilled in the laboratory.

[†] The east face of odd numbered joints is on the web surface on the diaphragm side and vice-versa for even numbered joints.

Table 4–6

Diaphragm End Support Details and Specimen Displacements,
Test Specimen 1
(193 kN/actuator)

Joint*	Length of Diaphragm End Support (mm)	Vertical Displacement (mm)	Differential Displacement	
			Designation	Displacement (mm)
3	1150	-4.02		
			$\Delta_{9\text{-}3}$	-0.09
9		-4.12		
4	1060	-5.18		
			$\Delta_{11\text{-}4}$	-0.31
11		-5.49		
5	925	-4.08		
			$\Delta_{13\text{-}5}$	-0.56
13		-4.64		
6	855	-1.51		
			$\Delta_{15\text{-}6}$	-0.10
15		-1.61		
8		-1.98		
			$\Delta_{8\text{-}17}$	-0.11
17	870	-1.87		
10		-5.07		
			$\Delta_{10\text{-}18}$	-0.56
18	1115	-4.50		
12		-5.68		
			$\Delta_{12\text{-}19}$	-0.41
19	1060	-5.26		
14		-4.01		
			$\Delta_{14\text{-}20}$	-0.29
20	1160	-3.72		

* Refer to Figure 3–4 for joint location.

Table 4–7

Diaphragm End Reactions at Maximum Static Load, Test Specimen 1
(193 kN/actuator)

Joint	Span Length (mm)	Diaphragm End Deflection (mm)	Support Reaction Force (kN)
3	1150	-4.02	4.2
4	1060	-5.18	6.8
5	924	-4.08	8.2
6	855	-1.51	3.8
17	870	-1.87	4.5
18	1114	-4.50	5.1
19	1060	-5.26	7.0
20	1160	-3.72	3.8
		Total Load (kN):	43.3

Table 4–8

Web Gap Stresses at Maximum Static Load
on the East and West Face of Joint 11, Test Specimen 1
(193 kN/actuator)

Gauge**	Stress (MPa)	Major Principal Stress (MPa)	Minor Principal Stress (MPa)	Angle to Major Principal Axis[†] (degrees)
13	52.6			
14	39.8	83.7	1.6	38.0
15	32.7			
16	52.1			
17	N/R*	—	—	—
18	-46.1			
19	28.6			
20	-10.0	29.7	-62.8	-6.2
21	-61.8			
22	-4.4			
23	4.8	-4.0	-63.6	4.7
24	-63.2			
25	39.8			
26	5.1	—	—	—
27	N/R*			
28	10.3			
29	32.9	81.3	-4.9	8.8
30	66.1			

* N/R denotes gauge not functioning.

[†] Angle from horizontal (counter clockwise rotation positive).

** See Figure 3–13 for gauges location.

Table 4–9

Diaphragm End Support Details and Specimen Displacements, Test Specimen 2
(188 kN/actuator)

Joint*	Length of Diaphragm End Support (mm)	Vertical Displacement (mm)	Differential Displacements Designation	Displacement (mm)
3	1165	-3.78		
			Δ_{9-3}	-0.15
9		-3.93		
4	1130	-5.07		
			Δ_{11-4}	-0.28
11		-5.34		
5	992	-3.95		
			Δ_{13-5}	-0.47
13		-4.42		
6	840	-1.45		
			Δ_{15-6}	-0.18
15		-1.63		
8		-1.68		
			Δ_{8-17}	-0.17
17	830	-1.51		
10		-4.78		
			Δ_{10-18}	-0.67
18	1190	-4.12		
12		-5.48		
			Δ_{12-19}	-0.67
19	1210	-4.81		
14		-3.93		
			Δ_{14-20}	-0.13
20	1170	-3.80		

* Refer to Figure 3–4 for joint location.

Table 4–10

Diaphragm End Reactions at Maximum Static Load, Test Specimen 2
(188 kN/actuator)

Joint	Span Length (mm)	Diaphragm End Deflection (mm)	Support Reaction Force (kN)
3	1165	-3.78	3.8
4	1130	-5.07	5.5
5	990	-3.95	6.4
6	840	-1.45	3.9
17	830	-1.51	4.2
18	1190	-4.12	3.9
19	1210	-4.82	4.3
20	1170	-3.80	3.7
		Total Load (kN):	35.6

Table 4–11

Diaphragm End Support Details and Specimen Displacements, Test Specimen 3
(196 kN/actuator)

Joint*	Length of Diaphragm End Support (mm)	Vertical Displacement (mm)	Differential Displacements	
			Designation	Displacement (mm)
3	1420	-3.70		
			Δ_{9-3}	-0.23
9		-3.93		
4	1370	-5.04		
			Δ_{11-4}	-0.32
11		-5.36		
5	1220	-3.87		
			Δ_{13-5}	-0.39
13		-4.26		
6	915	-1.27		
			Δ_{15-6}	-0.35
15		-1.62		
8		-1.77		
			Δ_{8-17}	-0.38
17	945	-1.39		
10		-4.94		
			Δ_{10-18}	-0.50
18	1510	-4.44		
12		-5.48		
			Δ_{12-19}	-0.32
19	1330	-5.15		
14		-3.94		
			Δ_{14-20}	-0.00
20	1450	-3.93		

* Refer to Figure 3–4 for joint location.

Table 4–12

Diaphragm End Reactions at Maximum Static Load, Test Specimen 3
(196 kN/actuator)

Joint	Span Length (mm)	Diaphragm End Deflection (mm)	Support Reaction Force (kN)
3	1420	-3.70	4.0
4	1370	-5.04	6.0
5	1220	-3.87	6.5
6	915	-1.27	5.1
17	945	-1.39	5.1
18	1510	-4.44	4.0
19	1330	-5.15	6.7
20	1450	-3.93	3.9
		Total Load (kN):	41.2

Table 4–13

Web Gap Stresses at Maximum Static Load
on the East and West Face of Joint 12, Test Specimen 3
(196 kN/actuator)

Gauge**	Stress (MPa)	Major Principal Stress (MPa)	Minor Principal Stress (MPa)	Angle to Major Principal Axis[†] (degrees)
13	65.0			
14	5.5	65.3	-55.9	2.6
15	-55.7			
16	61.2			
17	14.7	68.0	29.1	24.6
18	35.9			
19	71.2			
20	14.6	78.9	43.6	27.9
21	51.3			
22	49.8			
23	25.0	69.3	17.8	38.0
24	37.3			
25	51.0			
26	4.0	51.1	-53.8	2.2
27	-53.6			
28	41.3			
29	-18.3	44.7	-56.3	-10.6
30	-52.9			

* N/R denotes gauge not responding.

[†] Angle from horizontal (counter clockwise rotation positive).

** See Figure 3–14 for gauges location.

Table 4–14

Diaphragm End Support Details and Specimen Displacements,
Test Specimen 4
(194 kN/actuator)

| Joint* | Length of Diaphragm End Support (mm) | Vertical Displacement (mm) | Differential Displacements | |
			Designation	Displacement (mm)
3	1420	-3.91		
			Δ_{9-3}	0.01
9		-3.90		
4	1500	-5.13		
			Δ_{11-4}	-0.25
11		-5.38		
5	1215	-3.88		
			Δ_{13-5}	-0.46
13		-4.35		
6	940	-1.18		
			Δ_{15-6}	-0.42
15		-1.60		
8		-1.65		
			Δ_{8-17}	-0.46
17	920	-1.19		
10		-4.88		
			Δ_{10-18}	-0.58
18	1430	-4.30		
12		-5.46		
			Δ_{12-19}	-0.42
19	1335	-5.04		
14		-3.85		
			Δ_{14-20}	-0.01
20	1260	-3.85		

* Refer to Figure 3–4 for joint location.

Table 4–15

Diaphragm End Reactions at Maximum Static Load, Test Specimen 4
(194 kN/actuator)

Joint	Span Length (mm)	Diaphragm End Deflection (mm)	Support Reaction Force (kN)
3	1420	-3.91	4.2
4	1500	-5.13	4.7
5	1215	-3.88	6.6
6	940	-1.18	4.4
17	820	-1.19	6.6
18	1430	-4.30	4.5
19	1335	-5.04	6.5
20	1260	-3.85	5.9
		Total Load (kN):	43.3

Table 4–16

Web Gap Stresses at Maximum Static Load
on the East and West Face of Joint 12, Test Specimen 4
(194 kN/actuator)

Gauge**	Stress (MPa)	Major Principal Stress (MPa)	Minor Principal Stress (MPa)	Angle to Major Principal Axis[†] (degrees)
13	81.4			
14	-10.1	81.9	-124.7	-2.8
15	-124.2			
16	135.9			
17	20.7	139.5	17.8	10.0
18	21.5			
19	N/R*			
20	37.1	—	—	—
21	62.3			
22	44.9			
23	48.7	88.8	-9.1	42.0
24	34.8			
25	68.9			
26	7.3	69.3	-63.8	3.1
27	-63.4			
28	16.3			
29	-58.3	55.0	-71.5	-33.6
30	-32.8			

* N/R denotes gauge not responding.

[†] Angle from horizontal (counter clockwise rotation positive).

** See Figure 3–15 for gauges location.

Table 4–17

Diaphragm End Support Details and Specimen Displacements, Test Specimen 5
(152 kN/actuator)

Joint*	Length of Diaphragm End Support (mm)	Vertical Displacement (mm)	Differential Displacements Designation	Differential Displacements Displacement (mm)
3	1380	-3.06		
			Δ_{9-3}	-0.04
9		-3.10		
4	1370	-4.04		
			Δ_{11-4}	-0.23
11		-4.27		
5	1290	-3.17		
			Δ_{13-5}	-0.38
13		-3.56		
6	840	-1.05		
			Δ_{15-6}	-0.30
15		-1.35		
8		-1.38		
			Δ_{8-17}	-0.36
17	780	-1.02		
10		-3.88		
			Δ_{10-18}	-0.36
18	1430	-3.51		
12		-4.29		
			Δ_{12-19}	-0.26
19	1380	-4.03		
14		-3.09		
			Δ_{14-20}	-0.02
20	1280	-3.07		

* Refer to Figure 3–4 for joint location.

Table 4–18

Diaphragm End Reactions at Maximum Static Load, Test Specimen 5
(152 kN/actuator)

Joint	Span Length (mm)	Diaphragm End Deflection (mm)	Support Reaction Force (kN)
3	1380	-3.06	3.6
4	1370	-4.04	4.8
5	1290	-3.14	4.5
6	840	-1.05	5.4
17	780	-1.02	6.6
18	1430	-3.51	3.7
19	1380	-4.03	4.7
20	1280	-3.07	4.5
		Total Load (kN):	37.7

Table 4–19

Web Gap Stresses at Maximum Static Load
on the East and West Face of Joint 12, Test Specimen 5
(152 kN/actuator)

Gauge**	Stress (MPa)	Major Principal Stress (MPa)	Minor Principal Stress (MPa)	Angle to Major Principal Axis[†] (degrees)
13	51.1			
14	3.4	51.2	-50.8	1.9
15	-50.7			
16	47.3			
17	16.2	57.2	20.7	31.4
18	30.6			
19	51.6			
20	16.7	64.1	29.2	36.7
21	41.6			
22	37.6			
23	21.3	55.7	12.5	40.3
24	30.6			
25	43.5			
26	2.5	43.5	-41.6	1.7
27	-41.5			
28	38.7			
29	-9.1	39.7	-43.0	-6.4
30	-42.0			

* N/R denotes gauge not responding.

[†] Angle from horizontal (counter clockwise rotation positive).

** See Figure 3–14 for gauges location.

Table 4–20

Conditions for the Low Temperature Tests

Specimen	Low Temp. Test	Joint	Cycle (×10⁶)	Crack Length (mm)	Actuator Load (kN)		Midspan Bottom Fibre Stress (MPa)	Temperature Readings (°C)†				
					North	South		Gauge 1	Gauge 2	Gauge 3	Gauge 4	Gauge 5
1	1	12	2.83	152	193	-- 193	62	-47	-40	-37	-46	-50
	2				1	360	63					
2	1	10	4.65	95	188	188	62	-50	-48	-30	-49	-50
	2				372	1	62					
3	1	12	2.63	145	196	196	61	-50	-44	-38	-46	-38
	2				1	375	60					

† See Figure 3–18 for orientation of thermistors in insulated chamber.

Table 4–21

Comparison of Differential Displacements and Web Gap Distortions
before and after Repair of Joint 10, Test Specimen 2

(188 kN/actuator)

| | Joint* | Vertical Displacement (mm) | Differential Displacements | | Web Gap Distortion (mm) |
			Designation	Displacement (mm)	
Before Repair	10	-5.04	$\Delta_{10\text{-}18}$	-0.81	0.22
	18	-4.23			
After Repair	10	-5.01	$\Delta_{10\text{-}18}$	-0.56	0.00
	18	-4.45			
Completion of Fatigue Testing	10	-5.05	$\Delta_{10\text{-}18}$	-0.54	0.00
	18	-4.51			

* Refer to Figure 3–4 for joint location.

Table 4–22

Comparison of Differential Displacements and Web Gap Distortions
before and after Repair of Joint 12, Test Specimen 3

(196 kN/actuator)

| | Joint* | Vertical Displacement (mm) | Differential Displacements | | Web Gap Distortion (mm) |
			Designation	Displacement (mm)	
Before Repair	12	-5.30	$\Delta_{12\text{-}19}$	-0.27	0.14
	19	-5.03			
After Repair	12	-5.33	$\Delta_{12\text{-}19}$	-0.05	0.02
	19	-5.27			
Completion of Fatigue Testing	12	-5.48	$\Delta_{12\text{-}19}$	0.00	0.00
	19	-5.48			

* Refer to Figure 3–4 for joint location.

Table 4–23

Comparison of Differential Displacements and Web Gap Distortions
before and after Repair of Joint 13, Test Specimen 4

(194 kN/actuator)

	Joint*	Vertical Displacement (mm)	Differential Displacements Designation	Displacement (mm)	Web Gap Distortion (mm)
Before Repair	5	-3.91	Δ_{13-5}	-0.42	
	13	-4.34			0.17
After Repair	5	-3.88	Δ_{13-5}	-0.37	
	13	-4.25			0.00
Completion of Fatigue Testing	5	-3.96	Δ_{13-5}	-0.48	
	13	-4.44			0.01

* Refer to Figure 3–4 for joint location.

Table 4–24

Comparison of Differential Displacements before and after repair of
Joints 10, 11, 12, and 13, Test Specimen 5

(152 kN/actuator)

	Joint*	Vertical Displacement (mm)	Differential Displacements	
			Designation	Displacement (mm)
	4	-4.04		
			$\Delta_{11\text{-}4}$	-0.23
	11	-4.27		
	5	-3.17		
			$\Delta_{13\text{-}5}$	-0.38
	13	-3.56		
Before Repair	10	-3.88		
			$\Delta_{10\text{-}18}$	-0.36
	18	-3.51		
	12	-4.29		
			$\Delta_{12\text{-}19}$	-0.26
	19	-4.03		
	4	-4.08		
			$\Delta_{11\text{-}4}$	-0.17
	11	-4.25		
	5	-3.22		
			$\Delta_{13\text{-}5}$	-0.29
	13	-3.51		
After Repair	10	-3.90		
			$\Delta_{10\text{-}18}$	-0.38
	18	-3.52		
	12	-4.27		
			$\Delta_{12\text{-}19}$	-0.22
	19	-4.04		
	4	-4.08		
			$\Delta_{11\text{-}4}$	-0.12
	11	-4.20		
	5	-3.23		
			$\Delta_{13\text{-}5}$	-0.25
Completion of Fatigue Testing	13	-3.47		
	10	-3.83		
			$\Delta_{10\text{-}18}$	-0.47
	18	-3.36		
	12	-4.20		
			$\Delta_{12\text{-}19}$	-0.22
	19	-3.98		

* Refer to Figure 3–4 for joint location.

Table 4–25

Tension Coupon Test Results

	Coupon	Modulus of Elasticity (MPa)	Static Yield Strength (MPa)	Static Ultimate Strength (MPa)
Girder 1	1	199000	307	454
	2	198000	307	453
Girder 2	1	195000	261	434
	2	195000	265	433
Girder 3	1	199000	303	459
	2	201000	303	460
Girder 4	1	198000	303	457
	2	203000	305	455
Girder 5	1	201000	298	450
	2	199000	297	448

Table 4–26

Charpy V-Notch Impact Test Results

Sample	Test Temperature (°C)	Girder 1 CVN Value (J) (% Shear Fracture)	Girder 2 CVN Value (J) (% Shear Fracture)	Girder 3 CVN Value (J) (% Shear Fracture)	Girder 4 CVN Value (J) (% Shear Fracture)	Girder 5 CVN Value (J) (% Shear Fracture)
1	+20	107 (95-100%)	106 (95-100%)	96 (95-100%)	77 (95-100%)	22 (50-55%)
2	+20	100 (95-100%)	132 (95-100%)	96 (95-100%)	76 (95-100%)	23 (60-65%)
3	-25	77 (75-80%)	100 (65-70%)	98 (75-80%)	57 (80-85%)	22 (20-25%)
4	-25	84 (75-80%)	68 (60-65%)	84 (80-85%)	72 (80-85%)	22 (15-20%)
5	-50	52 (60-65%)	53 (30-35%)	60 (65-70%)	61 (65-70%)	19 (10-15%)
6	-50	57 (60-65%)	65 (45-50%)	60 (75-80%)	57 (70-75%)	16 (10-15%)
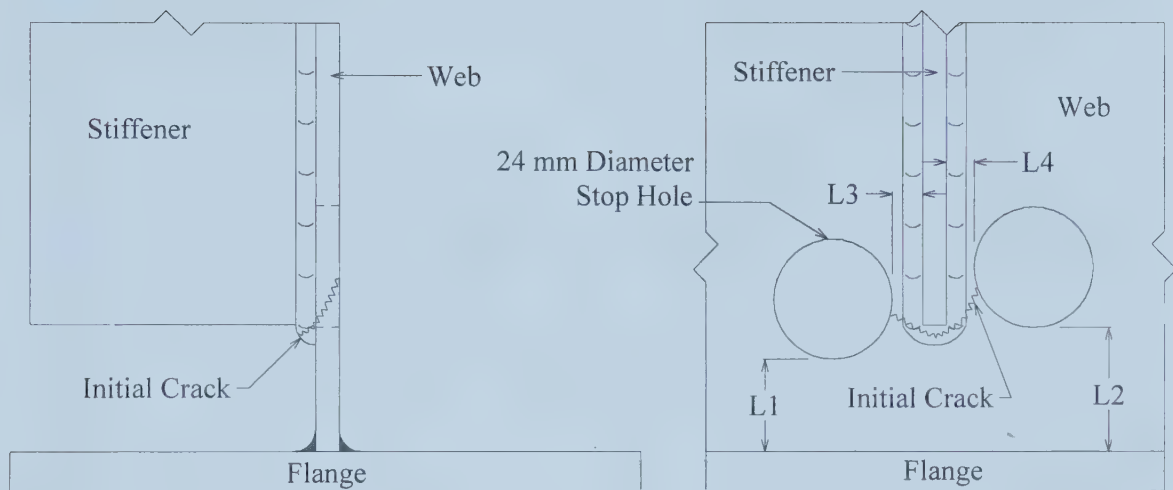
Figure 4–1 Typical Location of Stop Holes and Initial Cracks in Test Specimens
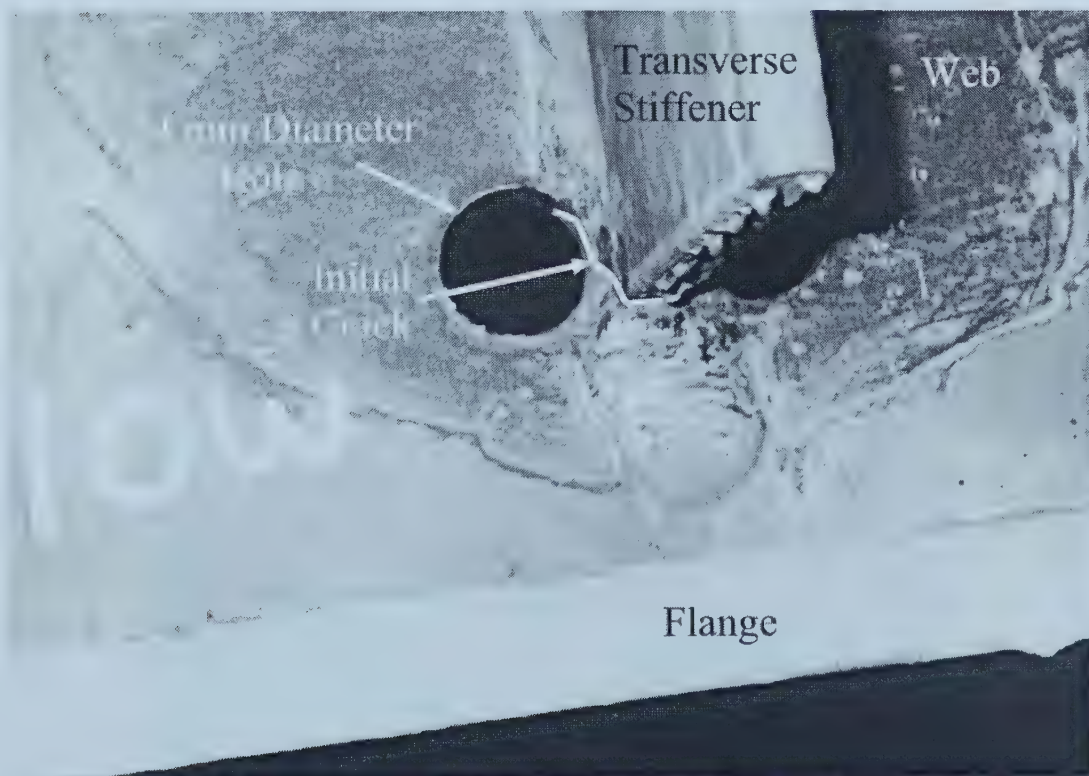
Figure 4–2 Initial Crack and Stop Holes on West Face of Joint 10, Specimen 1

84
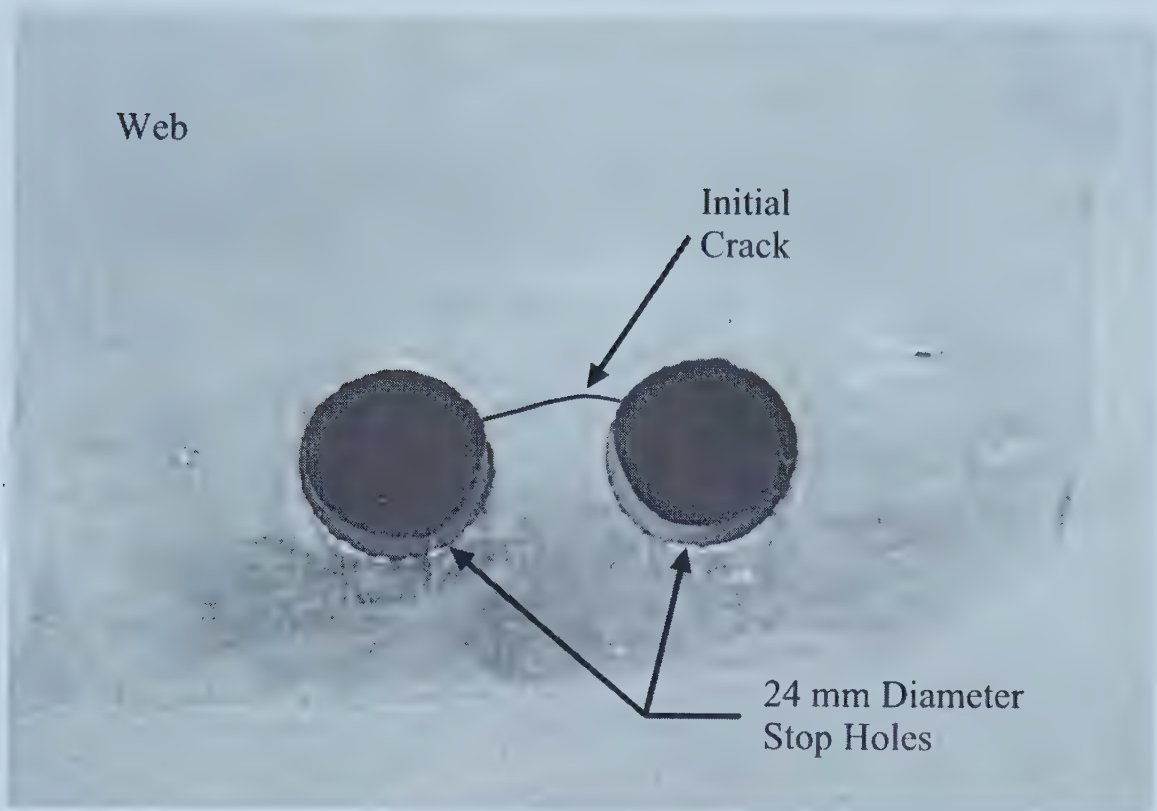
Figure 4–3 Initial Crack and Stop Holes on East Face of Joint 10, Specimen 1
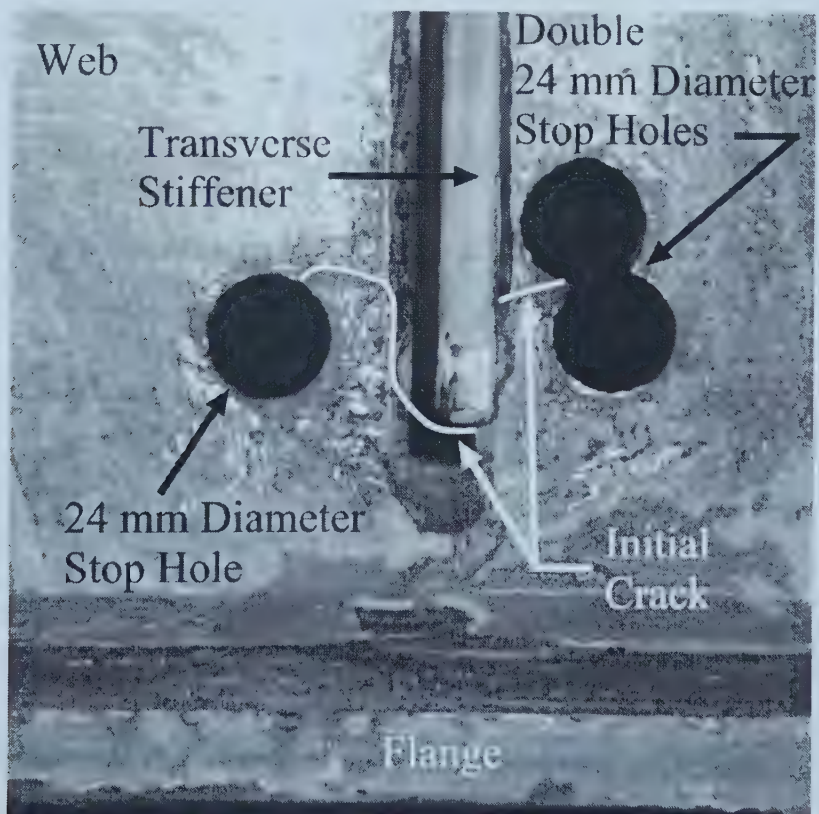
Figure 4–4 Initial Crack and Stop Holes on West Face of Joint 12, Specimen 2

85
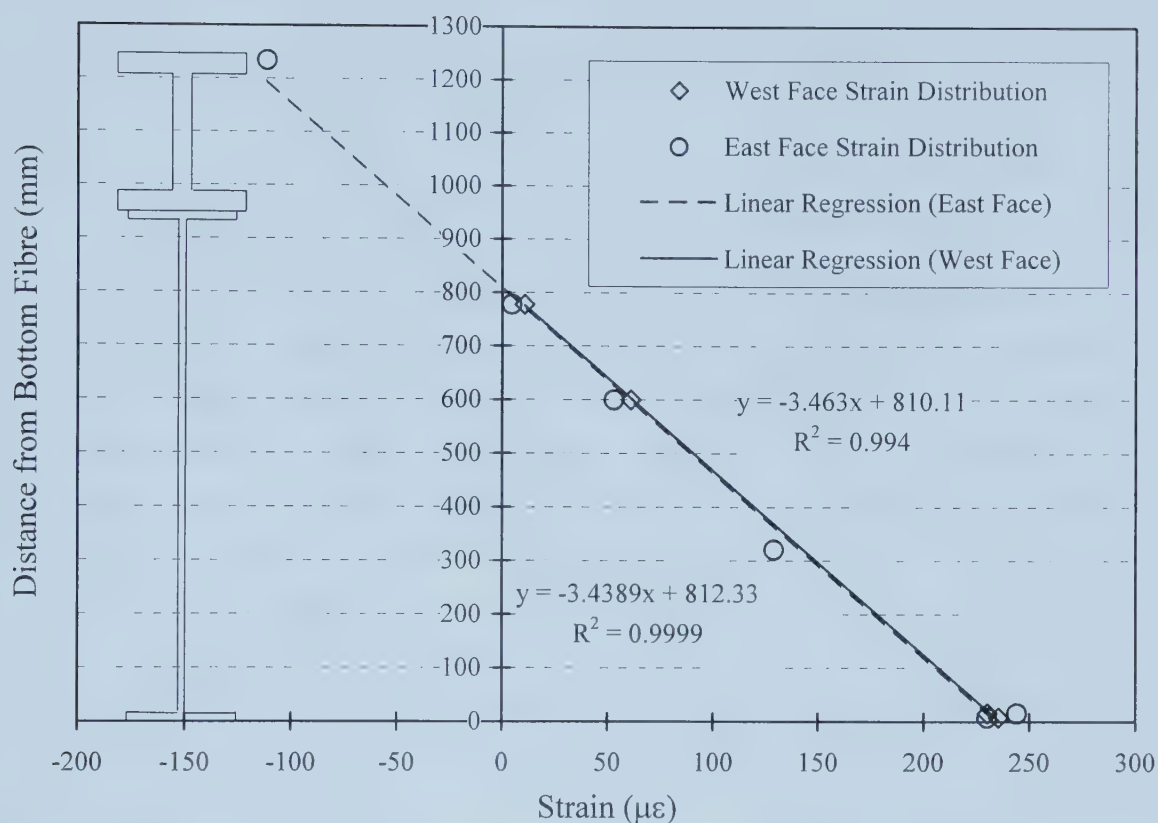
Figure 4–5 Strain Distribution at Midspan of Test Specimen 1 (P_{static}= 146 kN/actuator)
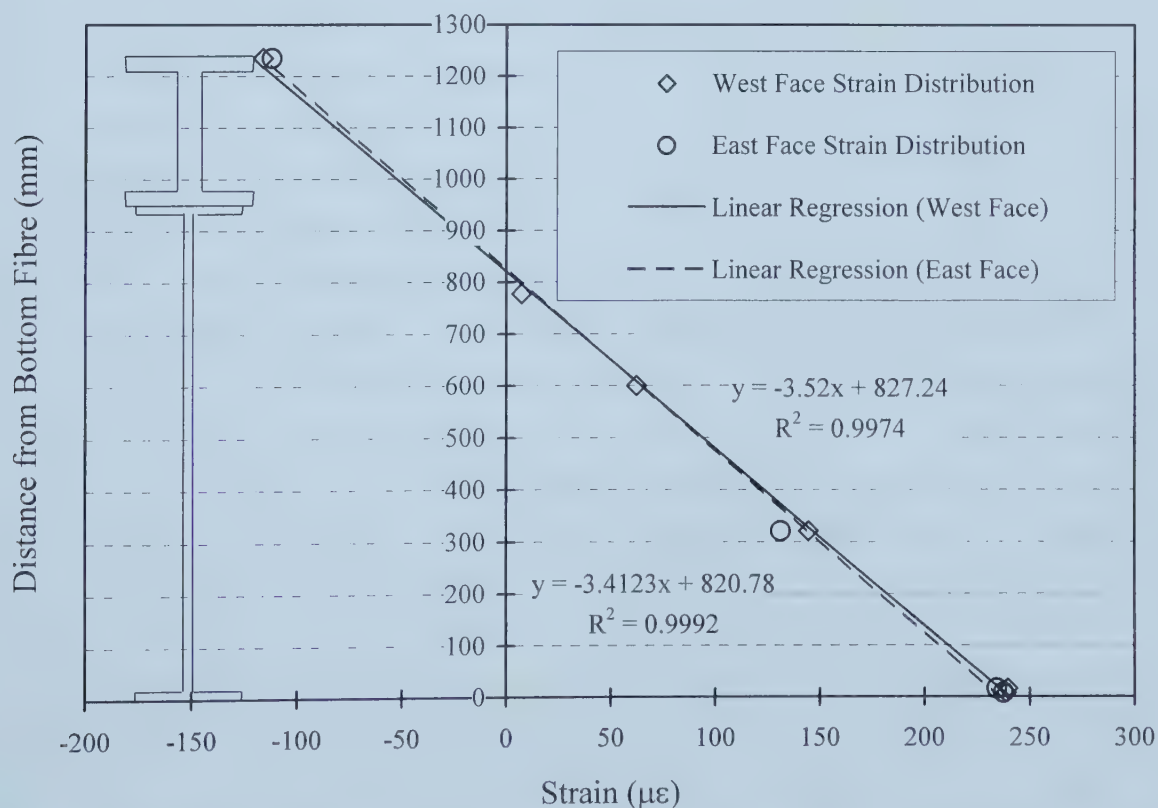
Figure 4–6 Strain Distribution at Midspan of Test Specimen 2 (P_{static}= 145 kN/actuator)

86
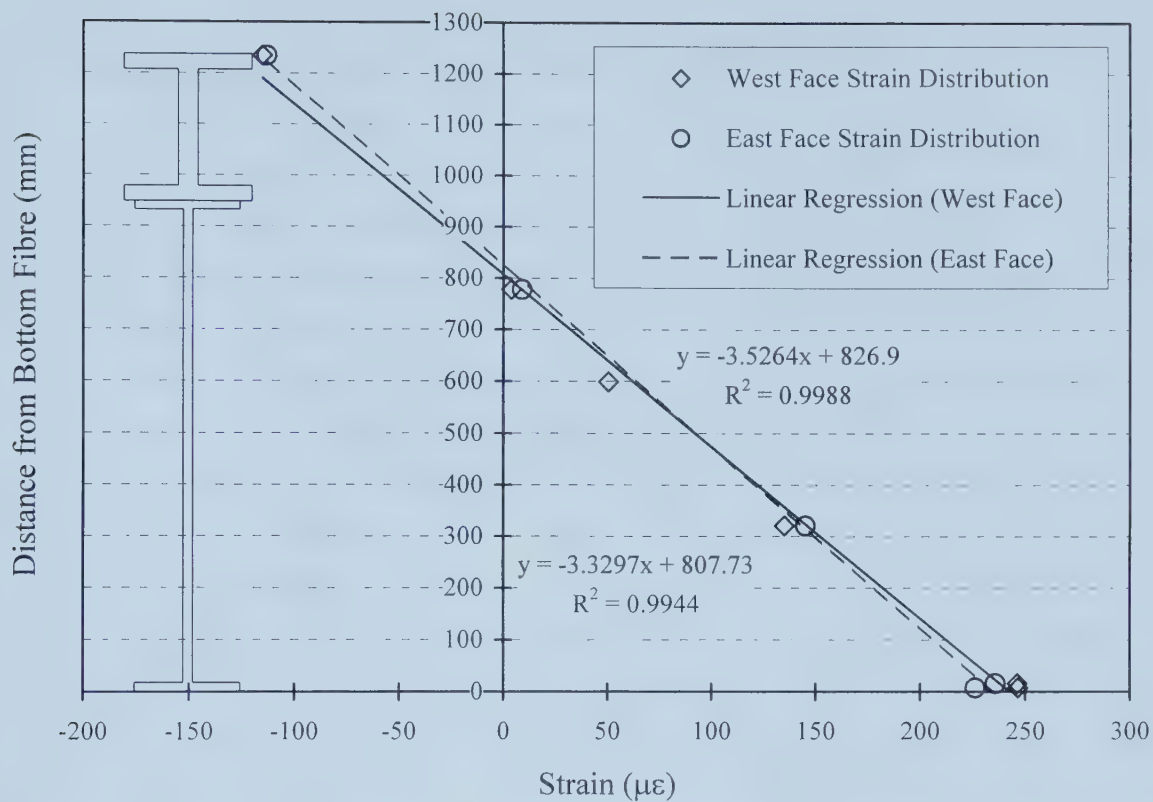
Figure 4–7 Strain Distribution at Midspan of Test Specimen 3 (P_{static}= 150 kN/actuator)
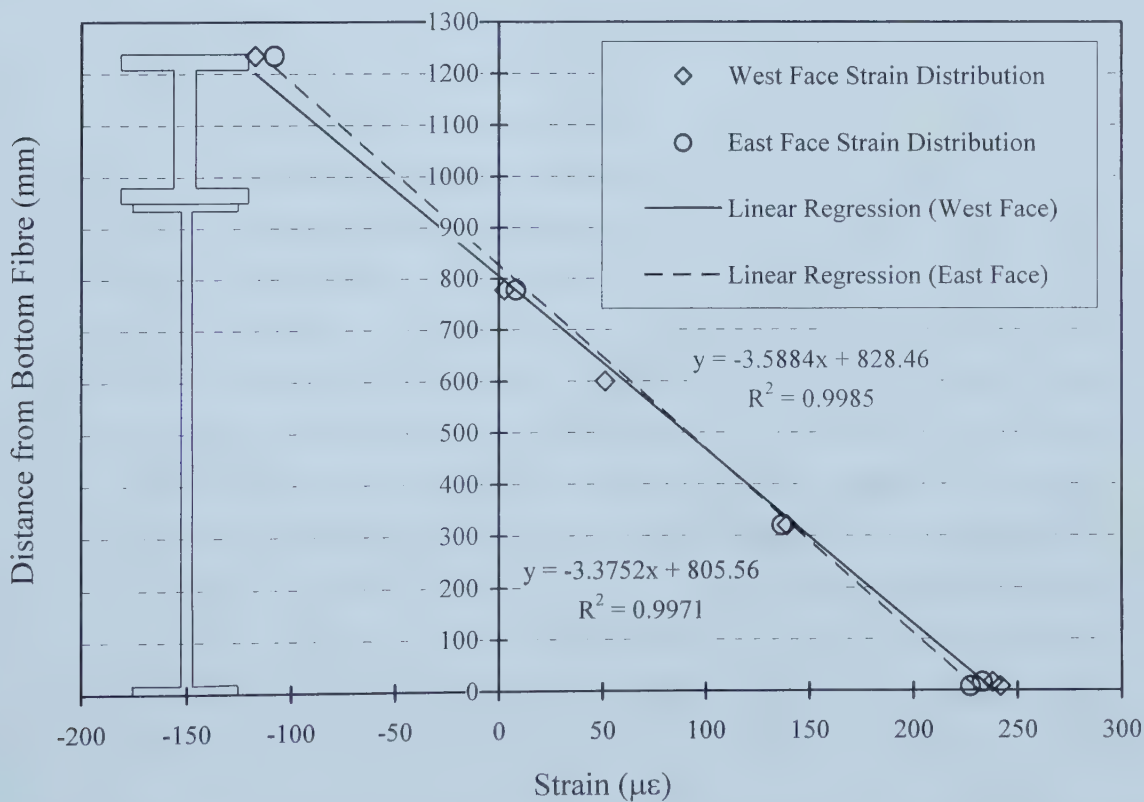
Figure 4–8 Strain Distribution at Midspan of Test Specimen 4 (P_{static}= 147 kN/actuator)
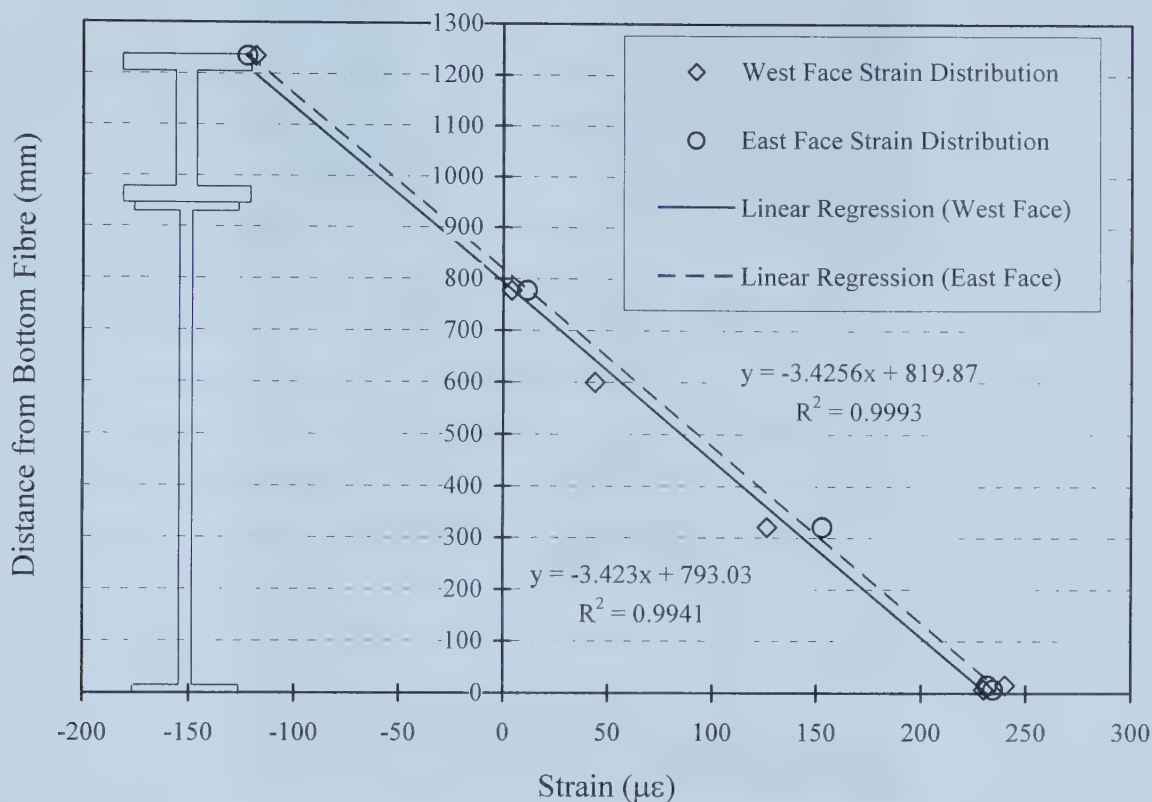
Figure 4–9 Strain Distribution at Midspan of Test Specimen 5 (P_{static}= 152 kN/actuator)

Equations on figure:

$y = -3.4256x + 819.87$
$R^2 = 0.9993$

$y = -3.423x + 793.03$
$R^2 = 0.9941$
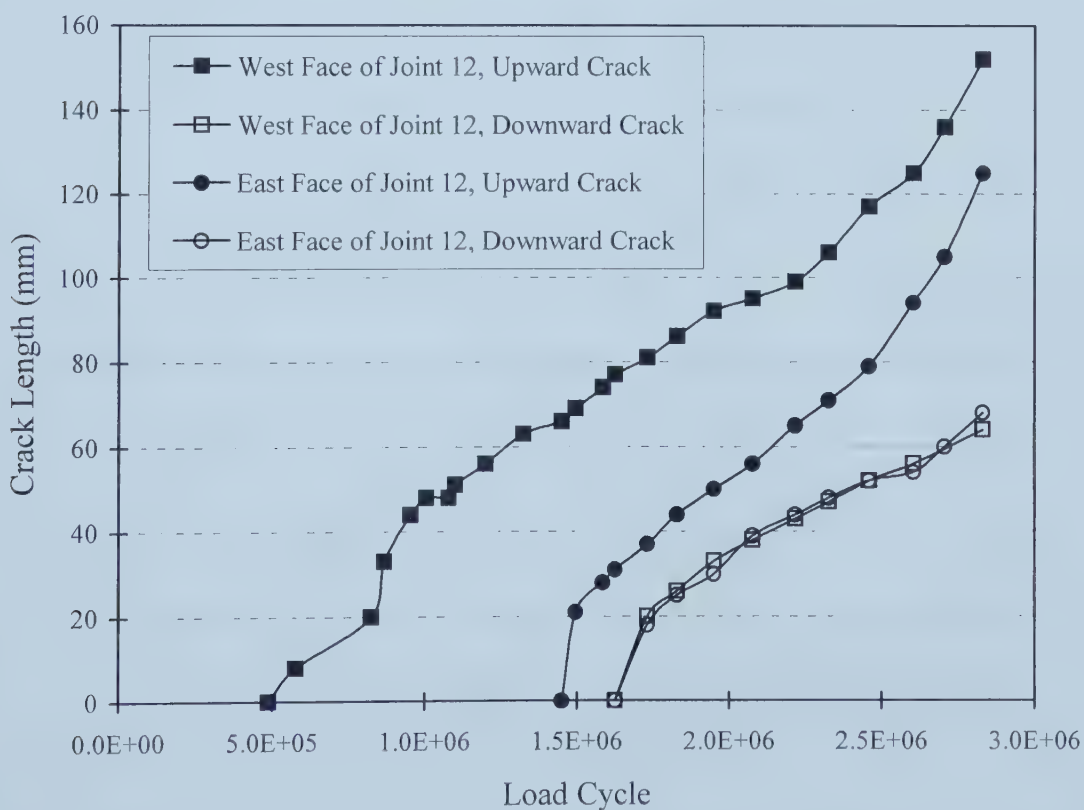
Figure 4–10 Joint 12 Crack Length vs. Load Cycle, Specimen 1

88
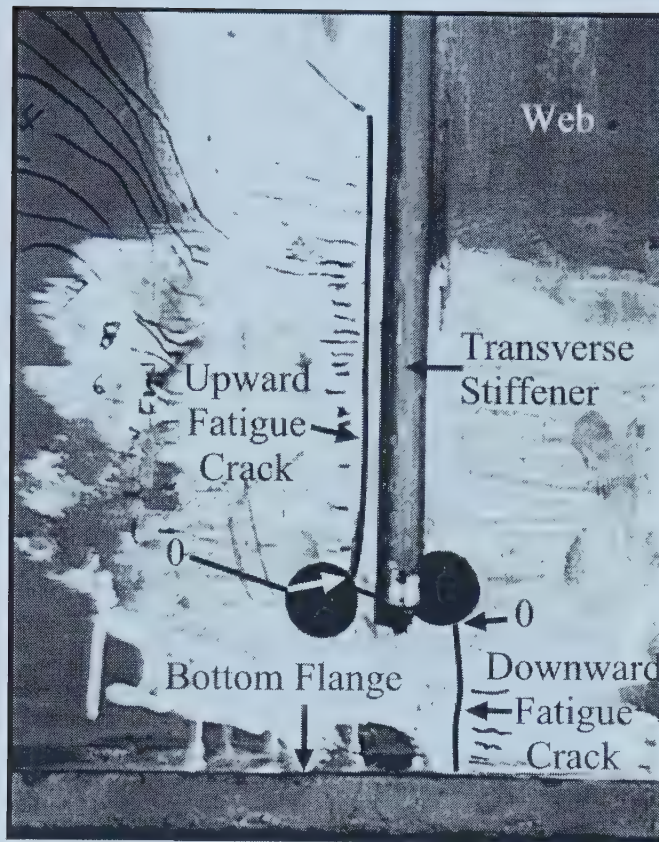
Figure 4–11 Fatigue Crack on West Face of Joint 12, Specimen 1
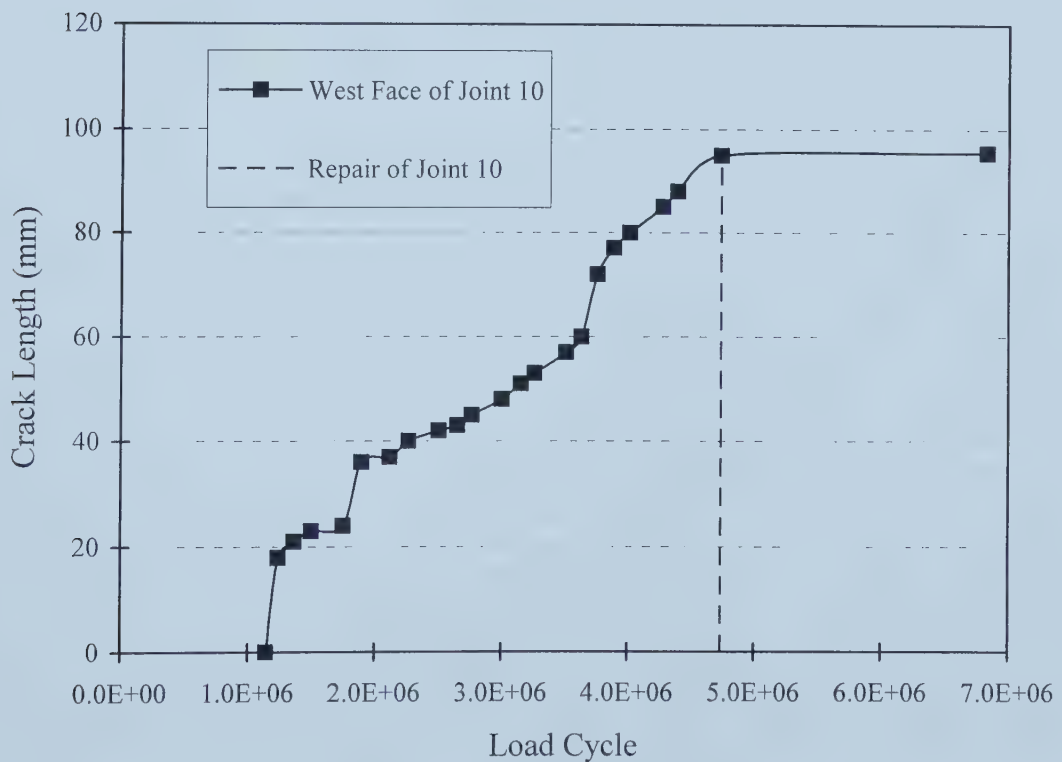
Figure 4–12 Joint 10 Crack Length vs. Load Cycle, Specimen 2
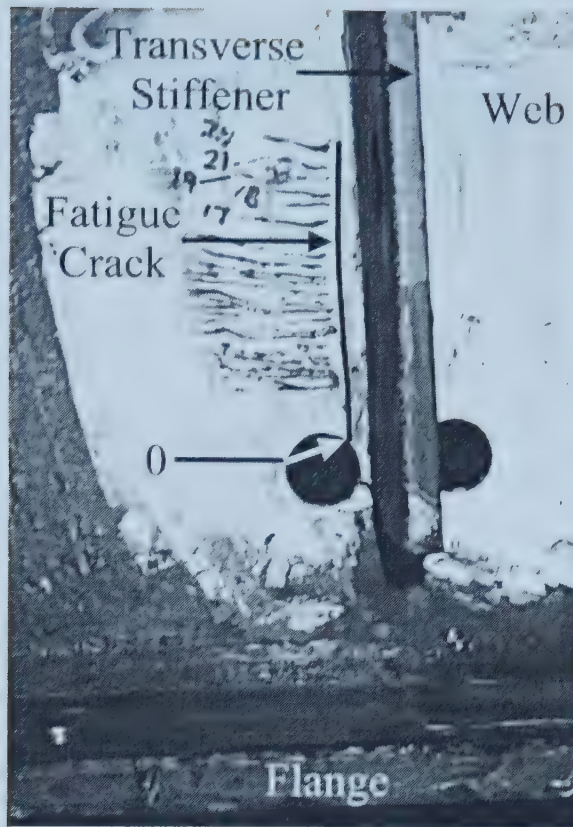
Figure 4–13 Fatigue Crack on West Face of Joint 10, Specimen 2
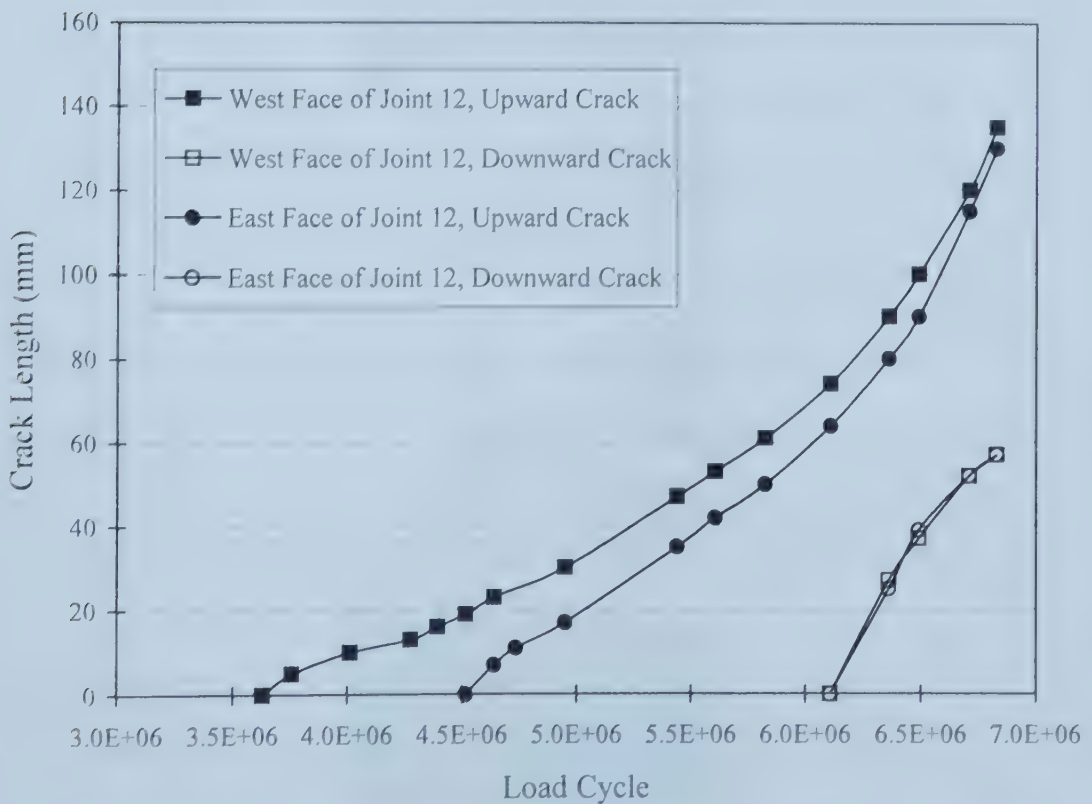
Figure 4–14 Joint 12 Crack Length vs. Load Cycle, Specimen 2

Figure 4–15 Fatigue Crack on West Face of Joint 12, Specimen 2
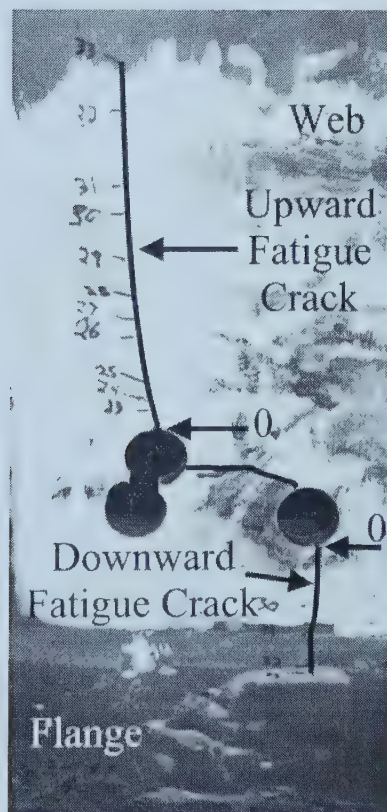
Figure 4–16 Fatigue Crack on East Face of Joint 12, Specimen 2

Figure 4–17 Fatigue Crack on West Face of Joint 12, Specimen 3
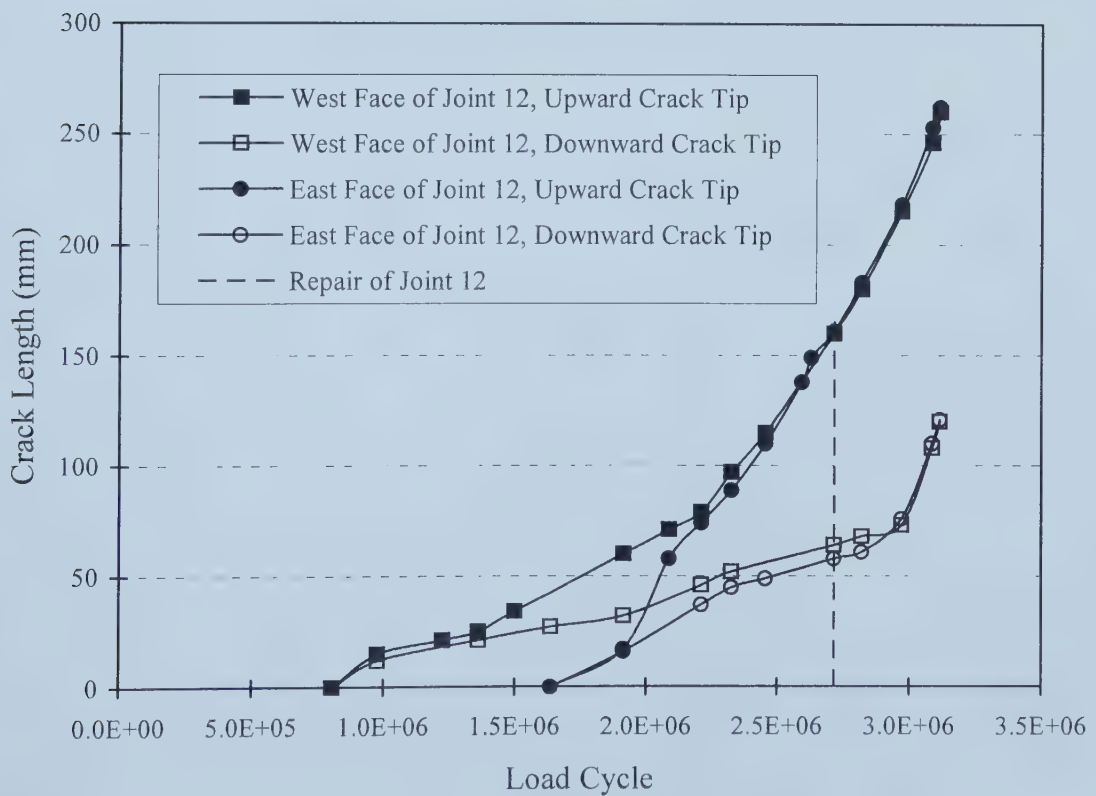
Figure 4–18 Joint 12 Crack Length vs. Load Cycle, Specimen 3
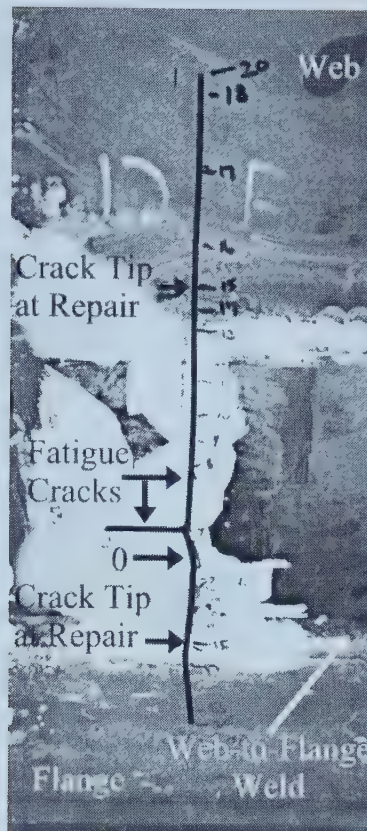
Figure 4–19 Fatigue Crack on East Face of Joint 12, Specimen 3
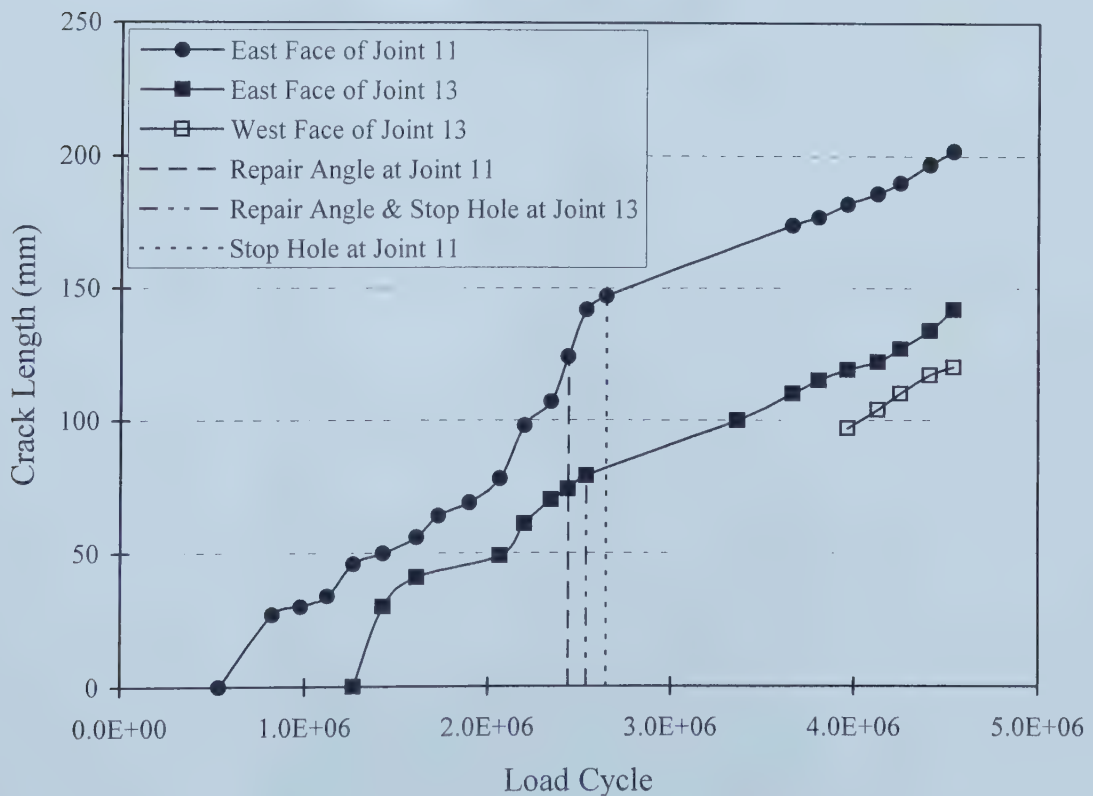
Figure 4–20 Crack Length vs. Load Cycle, Specimen 4
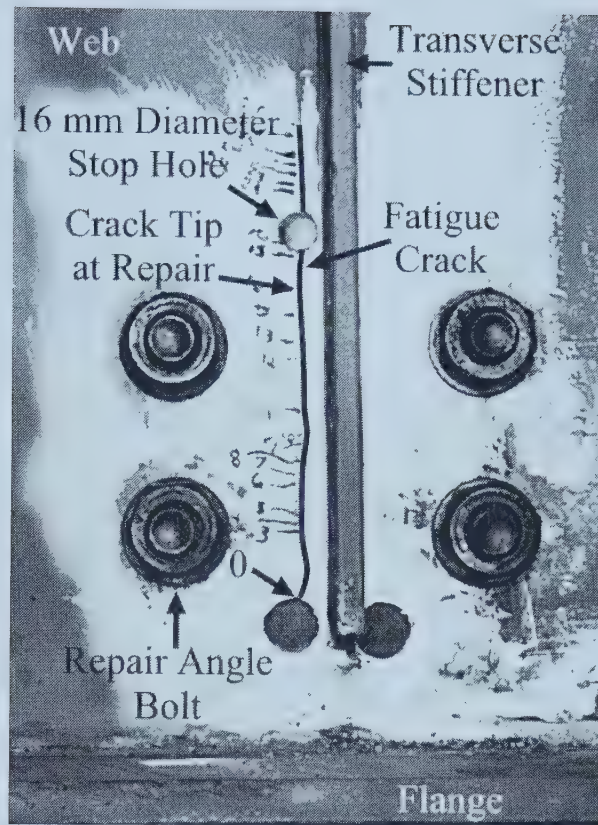
Figure 4–21 Fatigue Crack on East Face of Joint 11, Specimen 4
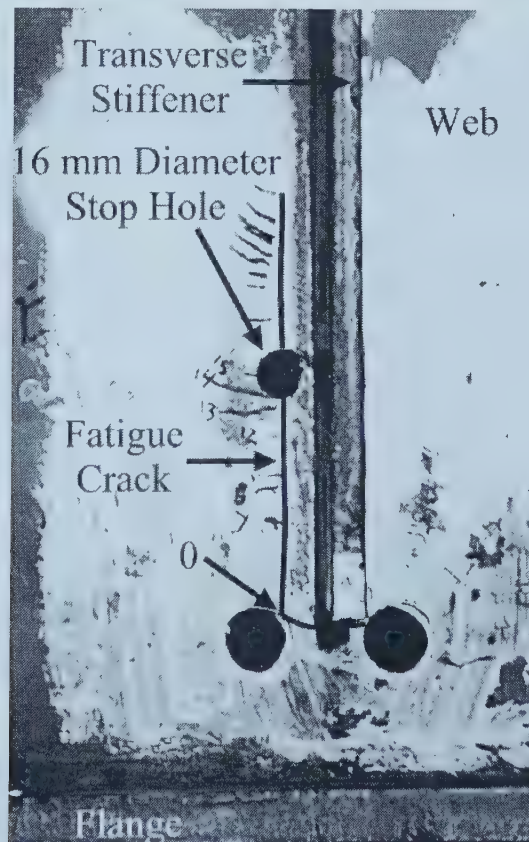
Figure 4–22 Fatigue Crack on East Face of Joint 13, Specimen 4
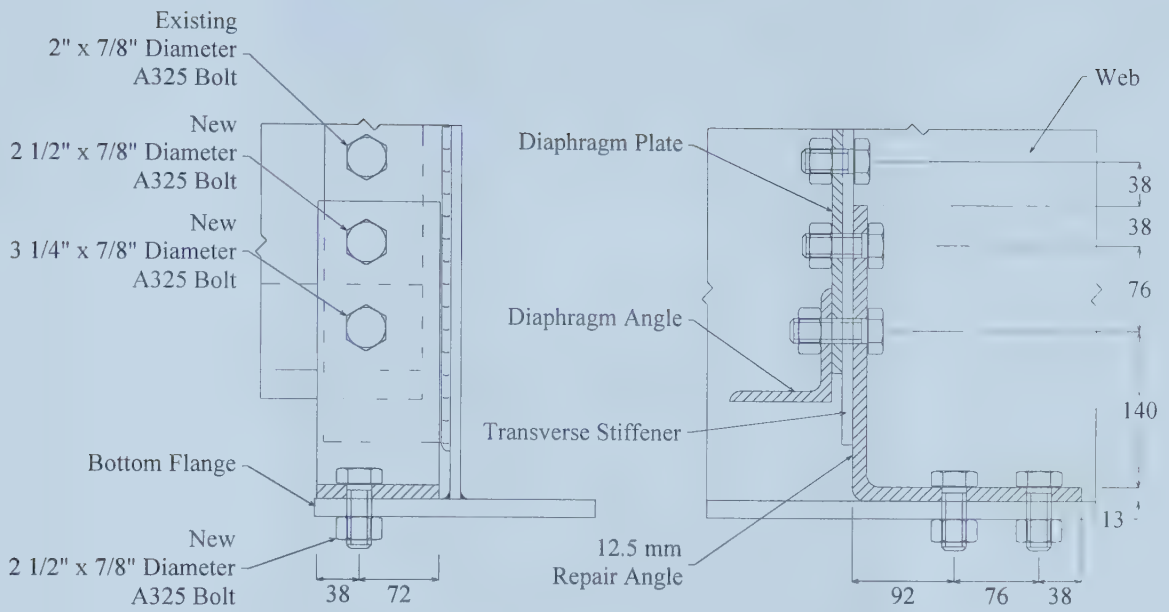
Figure 4–23 Typical Dimensions and Orientation of Stiffener-to-Flange Repair Angle
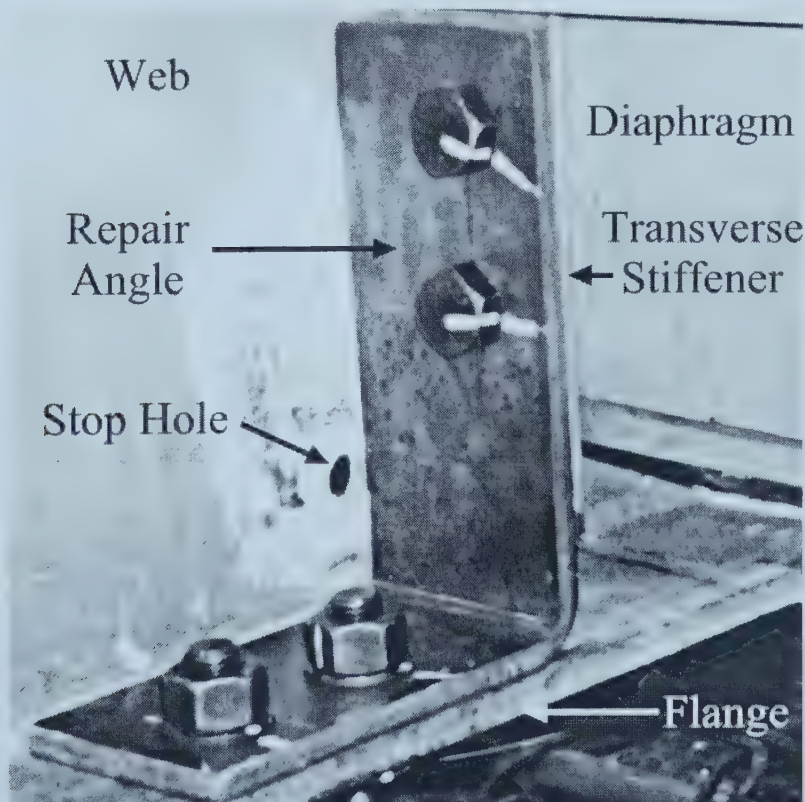
Figure 4–24 Repair Angle at Joint 10, Specimen 2
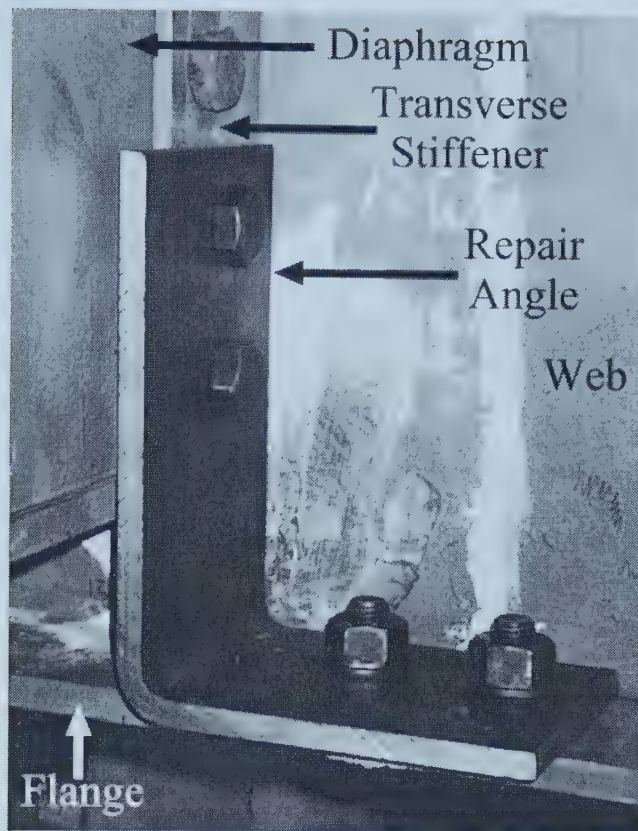
Figure 4–25 Repair Angle at Joint 12, Specimen 3

All dimensions in mm unless noted otherwise
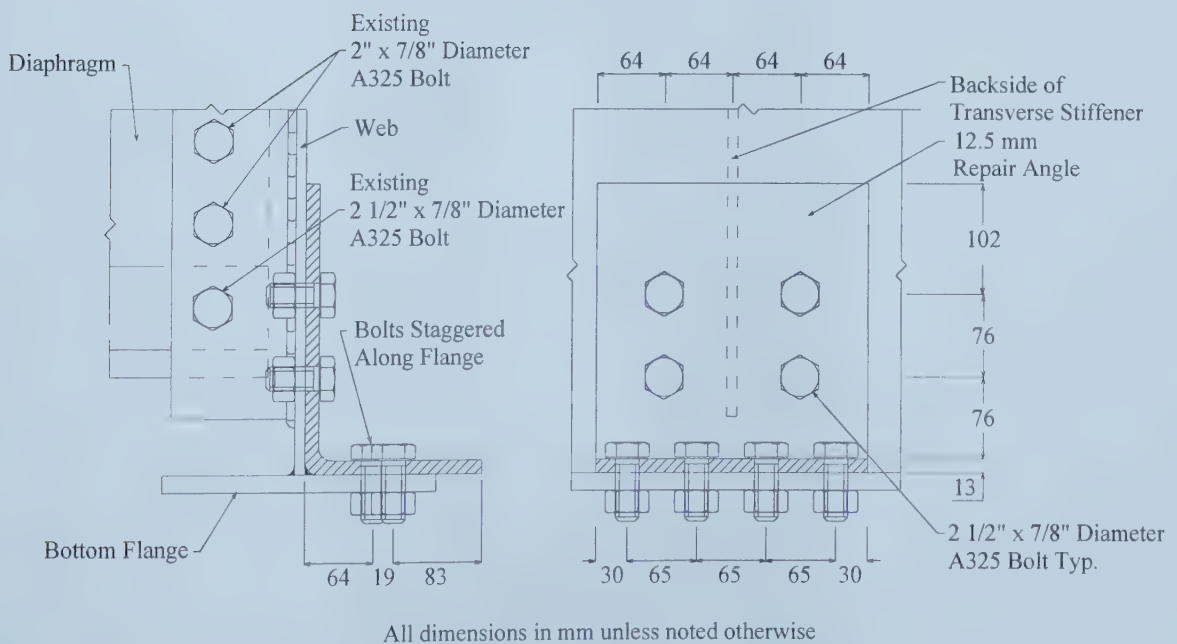
Figure 4–26 Typical Dimensions and Orientation of Web-to-Flange Repair Angle

Figure 4–27 Repair Angle at Joint 11, Specimen 4
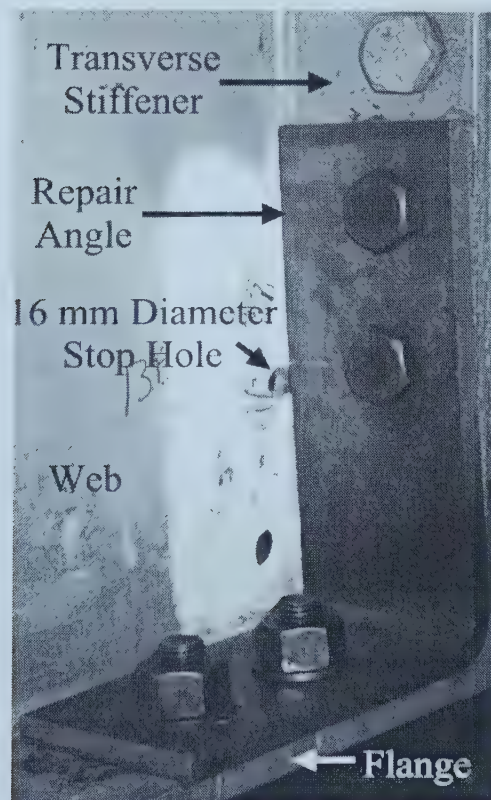
Figure 4–28 Repair Angle at Joint 13, Specimen 4
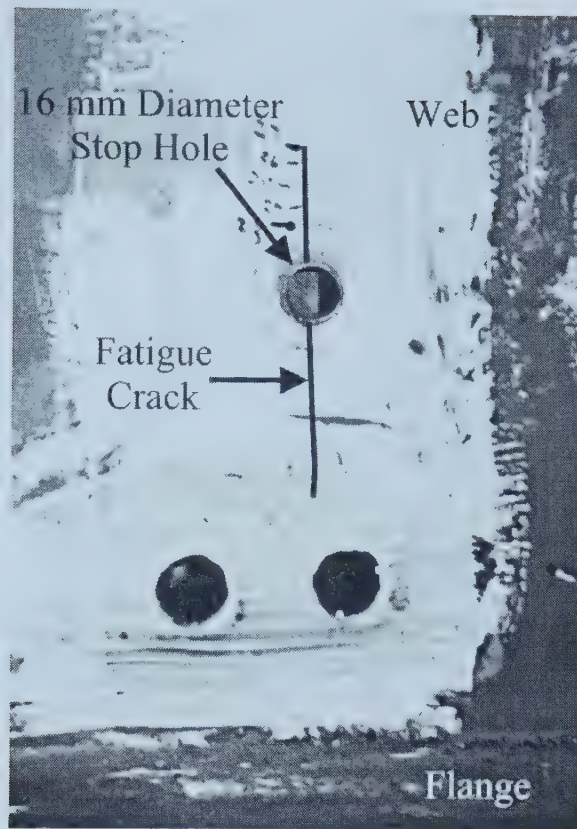
Figure 4–29 Fatigue Crack on West Face of Joint 13, Specimen 4
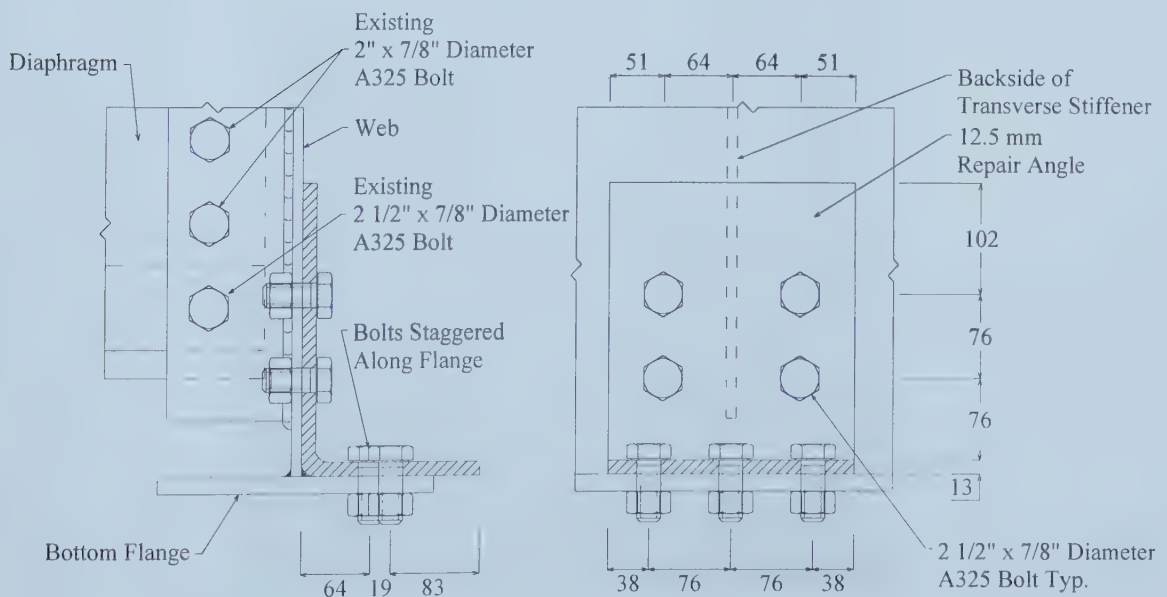
All dimensions in mm unless noted otherwise

Figure 4–30 Typical Dimensions and Orientation of Second Web-to-Flange Repair Angle
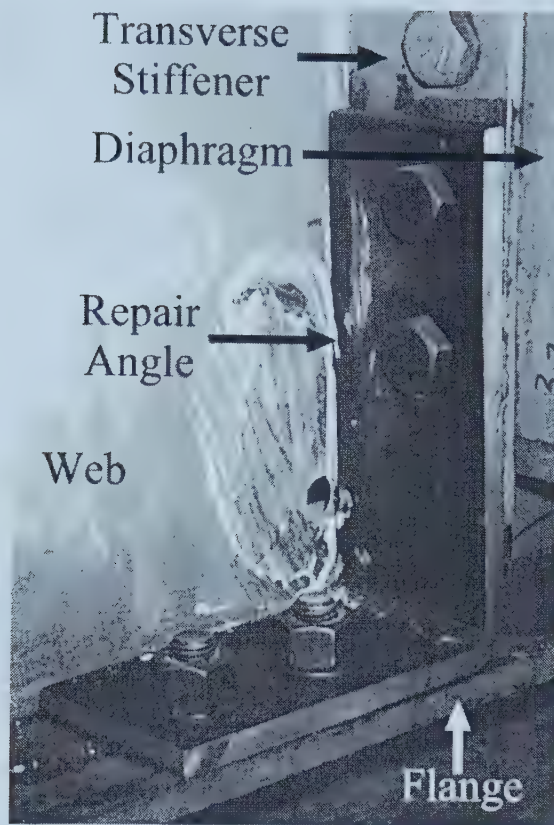
Figure 4–31 Repair Angle at Joint 10, Specimen 5

Figure 4–32 Repair Angle at Joint 11, Specimen 5
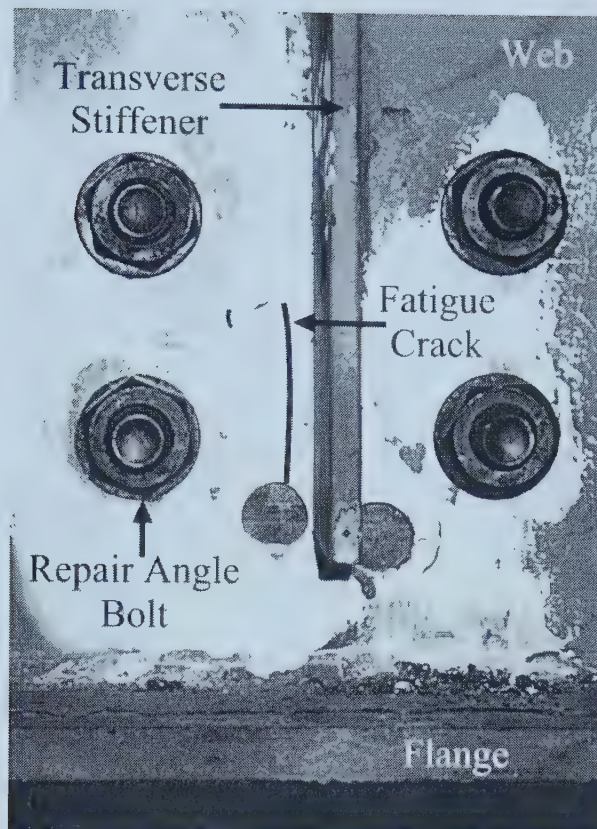
Figure 4–33 Fatigue Crack on East Face of Joint 11, Specimen 5
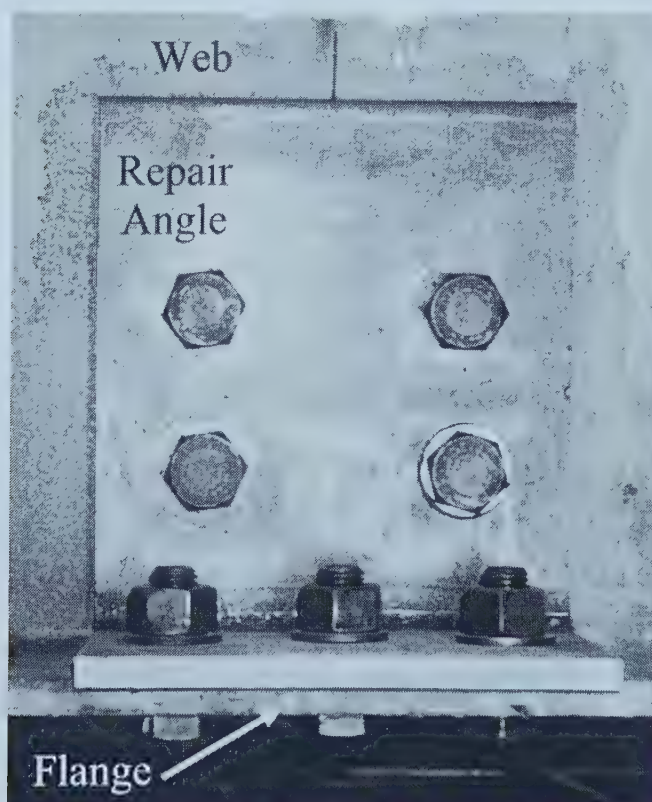
Figure 4–34 Repair Angle at Joint 12, Specimen 5
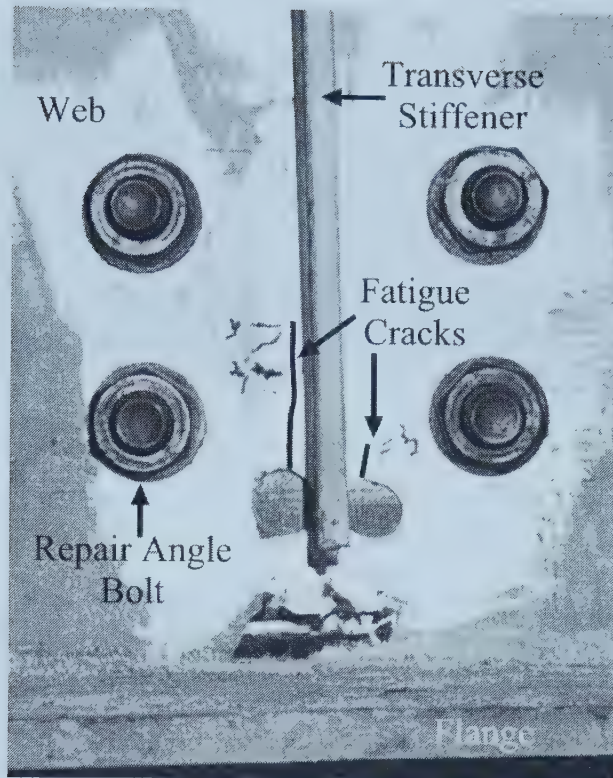
Figure 4–35 Fatigue Crack on West Face of Joint 12, Specimen 5
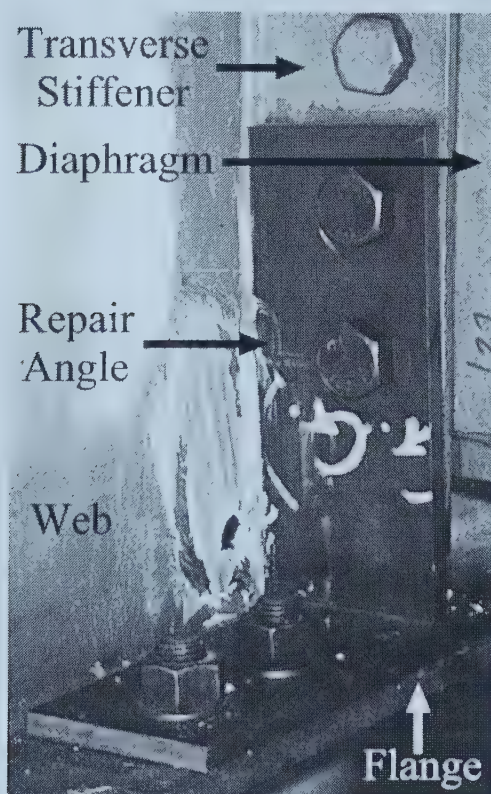
Figure 4–36 Repair Angle at Joint 13, Specimen 5

Girder 1 Girder 2 Girder 3 Girder 4 Girder 5

(a) +20° C

Girder 1 Girder 2 Girder 3 Girder 4 Girder 5

(b) –25° C

Girder 1 Girder 2 Girder 3 Girder 4 Girder 5
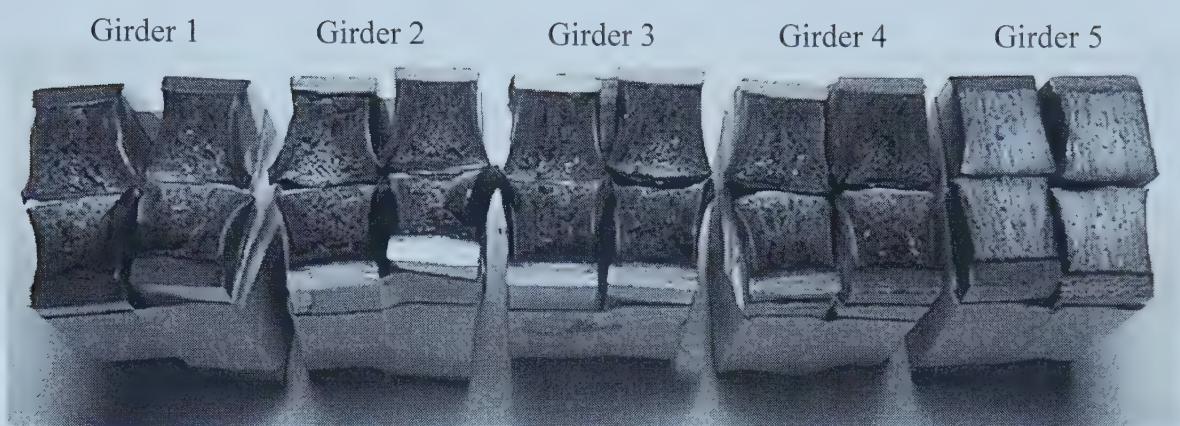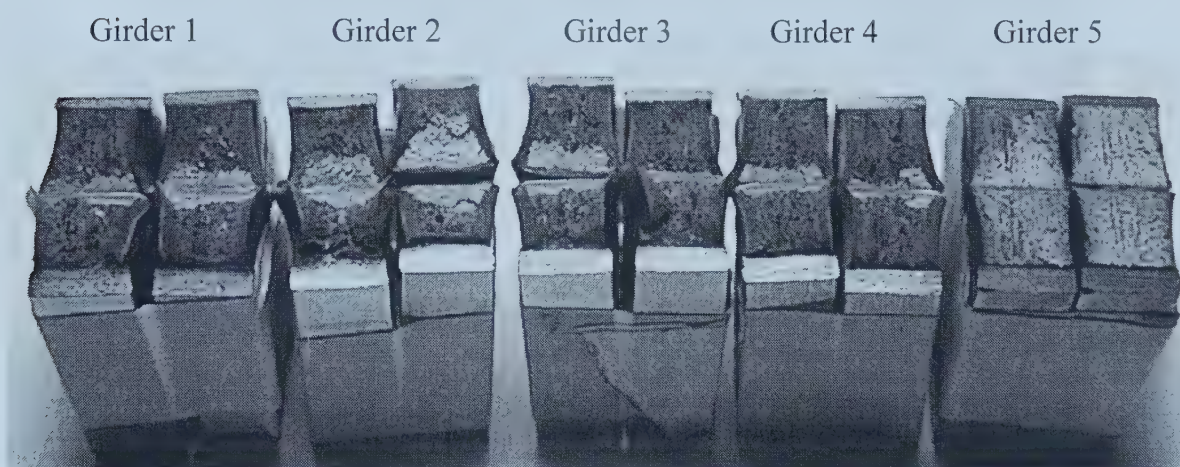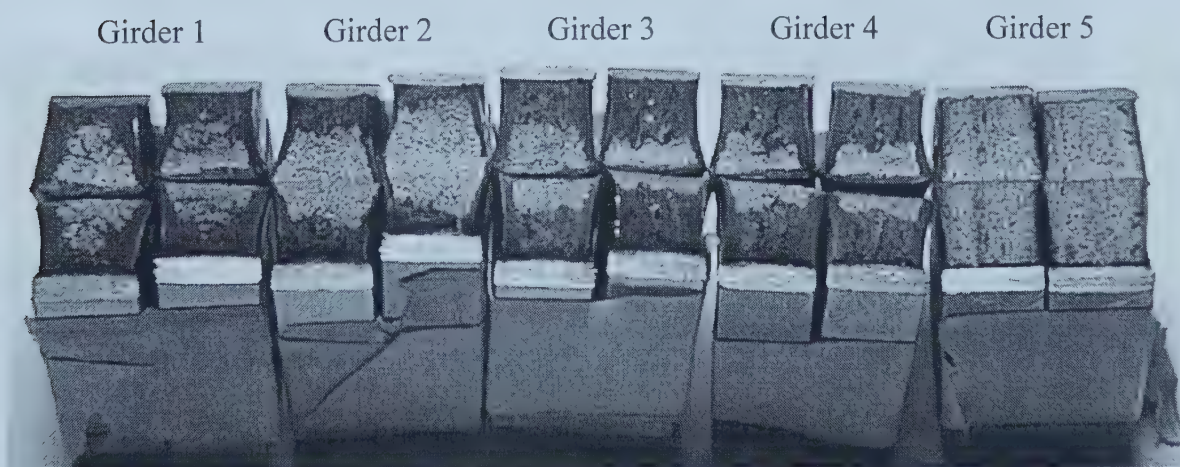
(c) –50° C

Figure 4–37 Fracture Surface Appearance of Charpy V-Notch Specimens

Figure 4–38 Corrosion of Upward Fatigue Crack Surface at Joint 12, Specimen 1
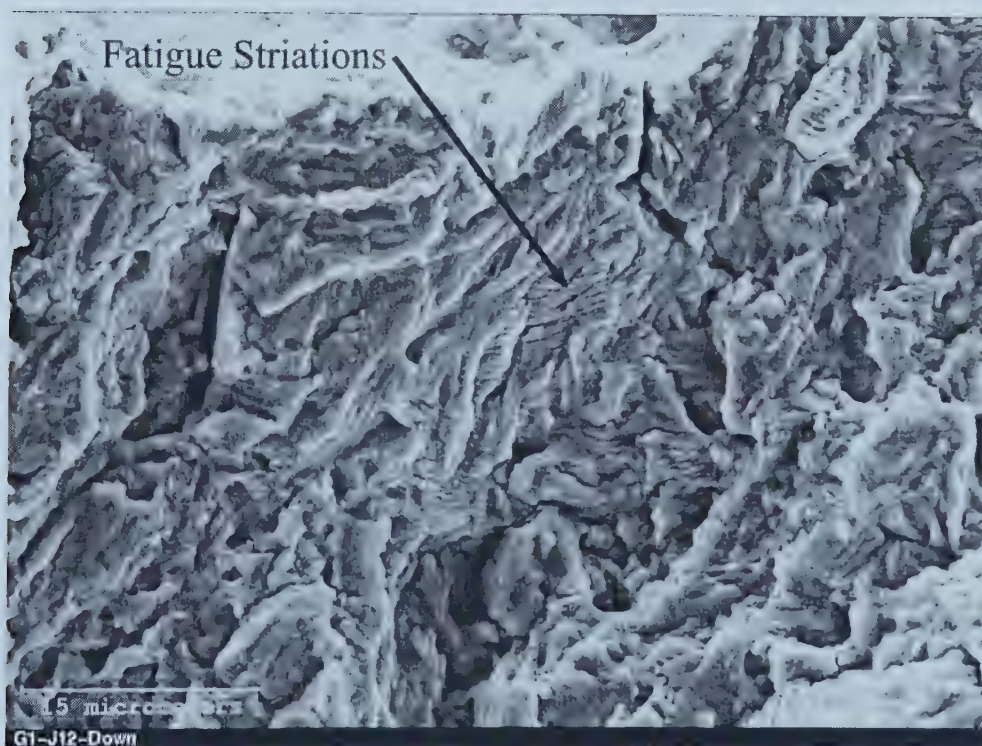
Figure 4–39 Fatigue Striations on Downward Fatigue Crack Surface at Joint 12, Specimen 1
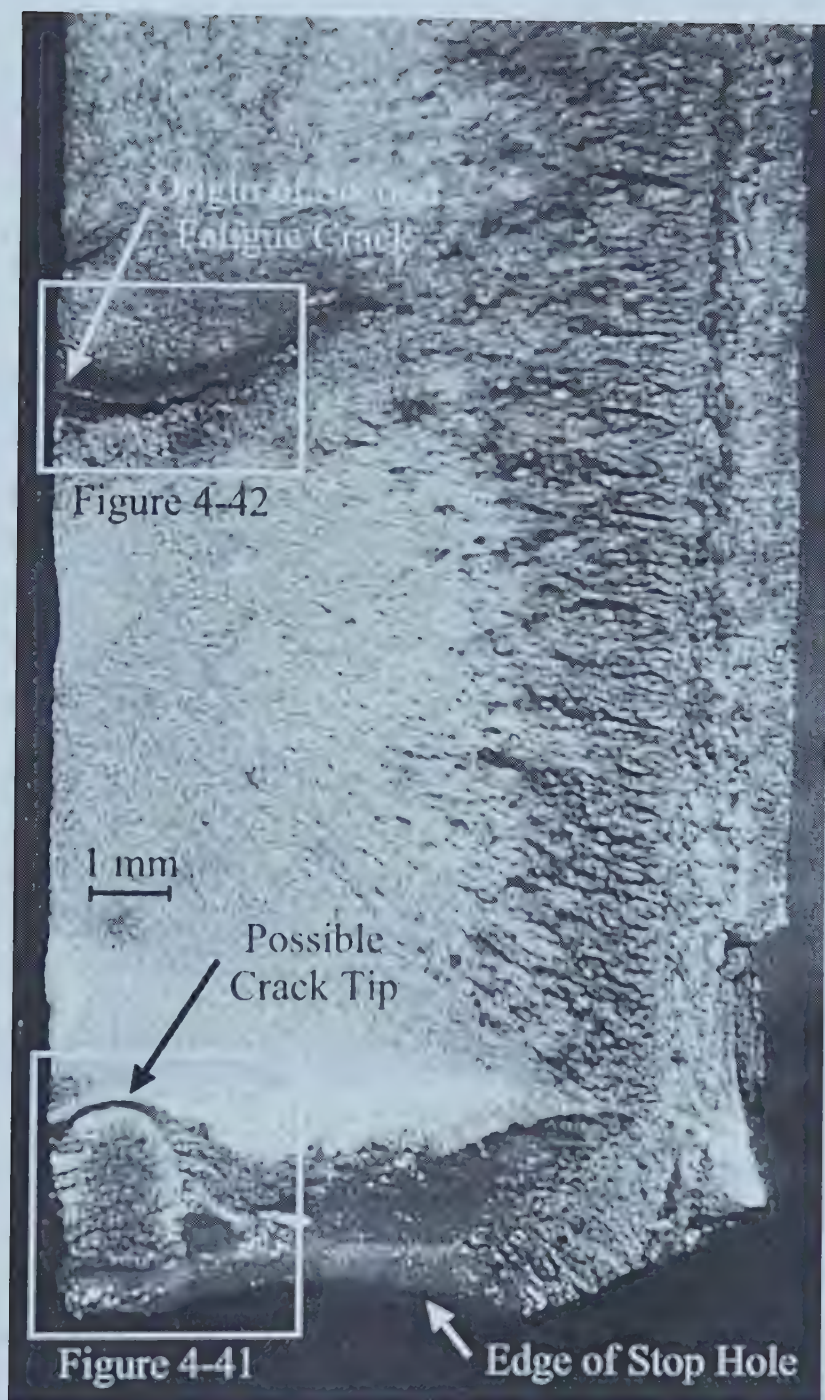
Figure 4–40 Upward Fatigue Crack Surface at Joint 10, Specimen 2

Labels within figure: 850 micrometers, Possible Crack Tip, Edge of Stop Hole, Corrosion, 850 micrometers, G2-J10-Up
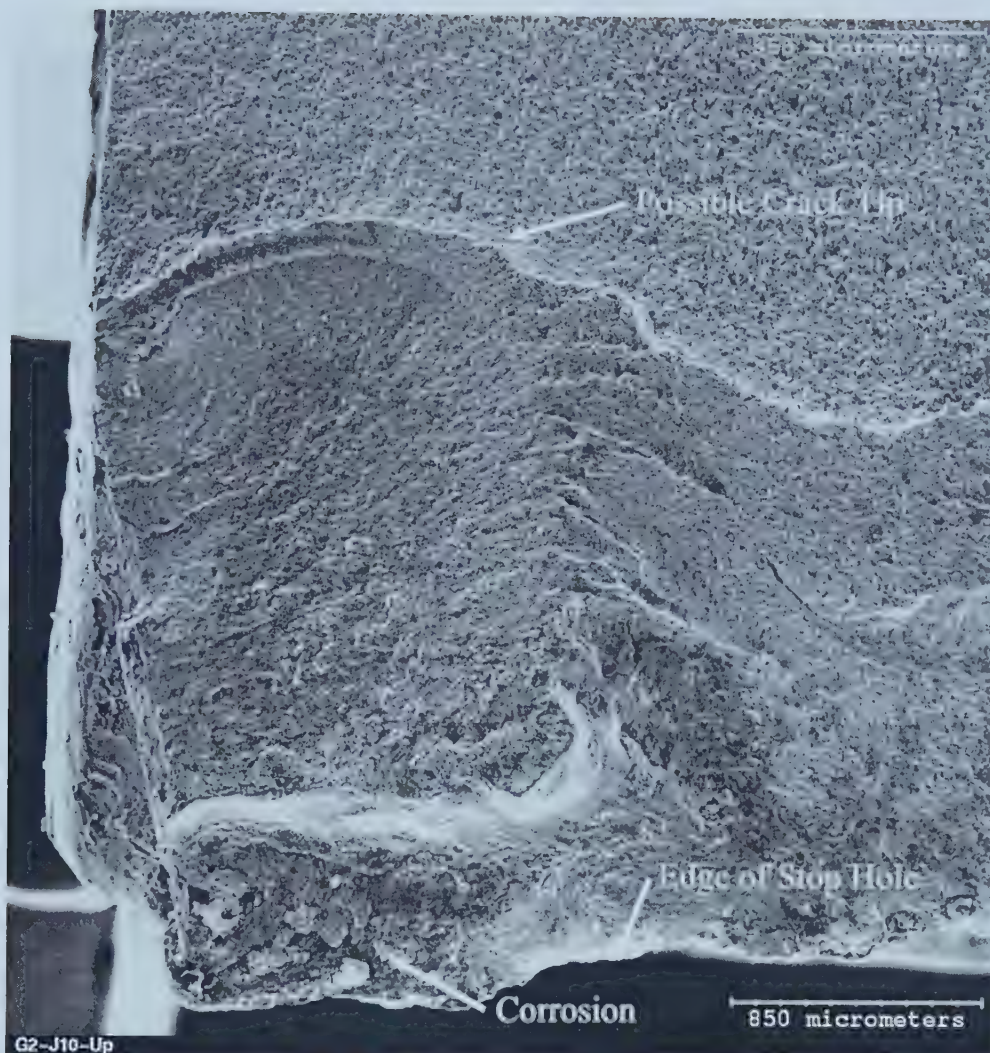
Figure 4–41 Upward Fatigue Crack Surface at Edge of Stop Hole
at Joint 10, Specimen 2
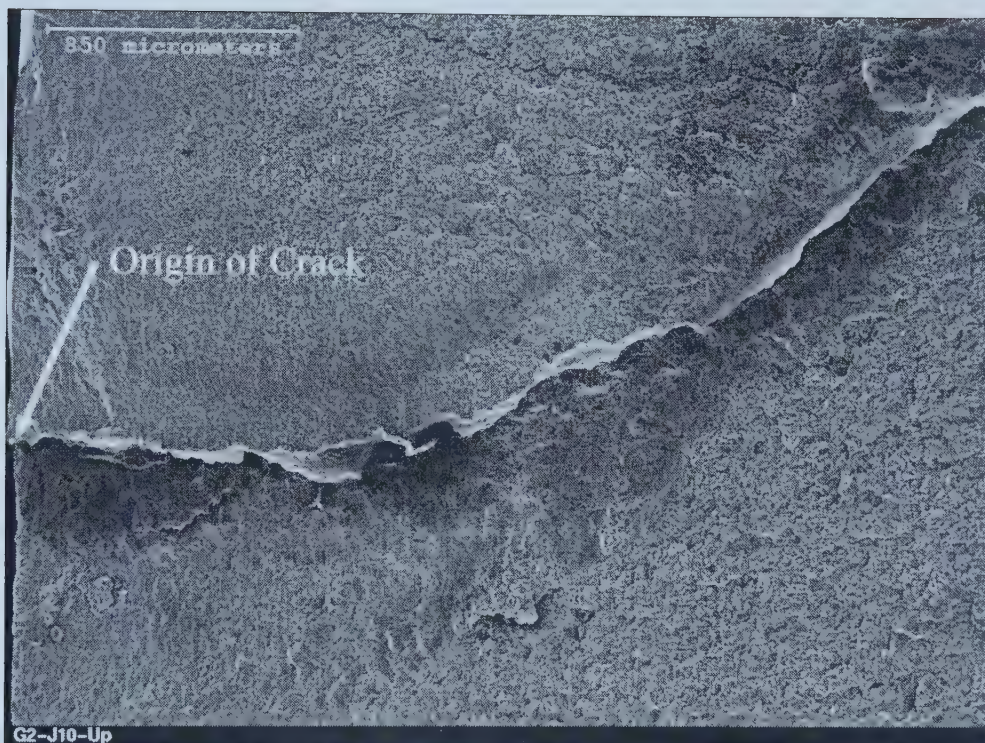
Figure 4–42 Upward Fatigue Crack Surface 11 mm from Edge of Stop Hole at Joint 10, Specimen 2

5. FINITE ELEMENT ANALYSIS

5.1 Introduction

The behaviour of the web gap region was examined using the structural analysis program S-Frame®. This chapter will describe the development of the finite element models and their validation using the strain and displacement measurements obtained from the test specimens. The results of a parametric study will also be discussed.

Two types of finite element models were developed to investigate the behaviour of the web gap region. The first type was developed to predict the global response of the test specimens. In these models, the full test specimens, including all the diaphragms and their supports, were included in the models. The second type focused on the local behaviour in the web gap region. In this case only the web gap region was included and the results from the global analyses were used as boundary conditions for the model of the web gap region. These models are referred to as substructure models. The finite element analysis of the test specimens was validated using the measured displacement and strains presented in Chapter 4.

The validated finite element models were then used to investigate the effect of the length of the web gap, the change in thickness of the bottom flange, and the presence of stop holes on the stresses in the web gap region.

5.2 Description of the Finite Element Models

A typical finite element model of a test specimen used to predict the measured global response in the laboratory is shown in Figure 5–1. Models were made of the three test specimens (1, 3, and 5) that were instrumented with strain rosettes at joint locations with no stop holes. To investigate the local behaviour of the web gap region, joint substructure models were developed, as shown in Figure 5–2. A total of 12 joint substructure models were developed, one model for each of the four joints located between the load actuators (Joints 10 to 13) from each of the three test specimen models.

Dimensions of test specimens 3, 4, and 5 are summarized in Table 5–1. The average measurements shown in Table 5–1 were used in both the test specimen models and the substructure models for specimens 3 and 5. The average web, flange, and stiffener thickness, flange width and girder height for specimen 3 were also used for the models of specimen 1 because measurements were not available for this specimen. This is partially justified by the small variation in dimensions observed among the three specimens listed in Table 5–1.

The reinforcing beam and the diaphragm angles were modelled using beam elements placed so that their axis would coincide with the centroidal axis of these elements in the test specimens. The beam element is a 2-node element with six degrees of freedom per node—three displacement degrees of freedom and three rotational degrees of freedom. The web and flanges of the test girder, the transverse stiffeners, and the diaphragm web plates were modelled with the S-Frame quadrilateral shell element. The shell element is a 4-node element with six degrees of freedom at each node. The thickness of the shell element is assumed to be constant over the entire element and the element stresses are calculated at the centre of the element (S-Frame, 1999).

The reinforcing beam and the diaphragm angles were tied to the girder and diaphragm webs by using rigid links between the nodes of the beam elements and the corresponding nodes of the shell elements. Rigid links between the diaphragm angle members and the shell elements of the web plate were added at all seven nodes along the top and the bottom of the plate. The bolts connecting the diaphragm to the stiffener were modelled as rigid links connecting the appropriate nodes in the stiffener and diaphragm. The variable spacing of the bolts connecting the reinforcing beam to the top flange of the girder did not match the element mesh. Hence rigid links were used to connect the girder and the reinforcing beam at each transverse stiffener and at midpoint between each transverse stiffener (see Figure 5–3).

Over 3 000 quadrilateral shell elements were used in each test specimen model, the exact number varied in accordance with the mesh refinement required at the stop holes. The models included the stop holes and through-thickness cracks that were observed in the

specimens at the beginning of the tests (see Tables 4–1, 4–3, and 4–5). Figure 5–4 shows a typical refined mesh near the web gap region. Although part-through-thickness cracks could not be modelled in the finite element analysis, initial through-thickness cracks between the drilled stop holes were modelled by leaving a small gap (0.5 mm) between quadrilateral shell elements at the approximate location of the crack.

The mesh in the substructure model was refined near the stiffener, around stop holes, and at the bottom of the web gap. The refined mesh near the web gap of the substructure model is shown in Figure 5–5. The total number of shell elements in the refined mesh substructure varied as a reflection of the stop holes. Typically, over 1 900 quadrilateral shell elements were used in each joint substructure model. The height of the joint substructure model (160 mm) was equal to the distance from mid-thickness of the bottom flange to the centre of the bottom bolt hole in the stiffener, and the width of the model was 418 mm. Since, the substructure model was developed directly from the model of the full test specimen described above, certain node locations along the boundary of the joint substructure model corresponded to nodes in the test specimen model. These interface nodes in the substructure model are identified in Figure 5–2. The displacements at the interface nodes, obtained from an analysis of the overall specimen model, were used as boundary conditions and loading of the refined mesh models. A typical section of test specimen model used to develop the substructure model is shown in Figure 5–6.

The supports used in the laboratory at the ends of the girder provided translational restraint in the vertical and out-of-plane directions and rotational restraint about the longitudinal axis of the girder. Figure 5–7 shows the restraints used at the ends of the girders in the test specimen models. The lateral bracing present to prevent lateral displacement of the test specimens was accommodated by preventing the lateral displacement at the nodes corresponding to the position of the lateral bracing in the test specimen. Out-of-plane translation and rotation about the longitudinal axis were restrained at the loaded nodes. The HSS spring supports at the end of the diaphragms were modeled using spring elements. The spring stiffnesses in each of the spring elements were initially set to values obtained from the span lengths of the HSS supports as shown in Tables 4–7, 4–12, and 4–18. Results from the finite element analyses of the

three test specimen models did not yield diaphragm rotations that were consistent with the values observed in the laboratory. Therefore, the spring support stiffnesses in the finite element models were adjusted to give differential displacements that were consistent with the measured values. The presence of part-through-thickness cracks in the web gap, which could not be incorporated in the finite element model, may have had a significant effect on the differential displacement.

The interface nodes in the joint substructure models were fully restrained in all the rotational and translational degrees of freedom. In order to model the flange-to-web junction of the girder in the substructure models, the shell elements forming the flange were placed at mid-thickness of the flange. Accounting for the flange thickness, the shell elements that make up the web included a row of elements whose height was equal to half the thickness of the bottom flange. Three degrees of freedom from the nodes at the bottom of the web were slaved to the corresponding degrees of freedom in the bottom flange. The slaved degrees of freedom were the vertical translation, rotation about the axis of the flange-to-web junction, and rotation in the plane of the web.

The average modulus of elasticity obtained from tests of the girder web material was used for all the elements in a given finite element model. The values of the modulus of elasticity used were 198 500 MPa, 200 000 MPa, and 200 000 MPa for test specimens 1, 3, and 5, respectively. These values are presented in Table 4–25.

The maximum static loads applied to the test specimens were applied as nodal forces on the reinforcing beam elements, as shown in Figure 5–3. The maximum static loads of 193 kN, 196 kN, and 152 kN per actuator were applied to the models of test specimens 1, 3, and 5, respectively. The substructure models were loaded by applying the resulting displacements and rotations of the interface nodes from the test specimen models as support displacements and rotations at the interface nodes in the joint substructure model.

5.3 Model Validation

5.3.1 Bottom Fibre Strain and Differential Displacements

As described above, finite element models of test specimens 1, 3, and 5 were developed to investigate the global response of the test specimens. Results from the models that utilised the actual stiffness of the diaphragm supports indicated that the composite action between the reinforcing beam and the girder was satisfactorily achieved; the neutral axis positions from the finite element analysis were within 2% of the values obtained from the laboratory tests. The predicted midspan bottom fibre strains were greater than the measured values by 5% for test specimen 1 to 10% for test specimen 5. As mentioned previously, the differential displacements were not consistent with the measured differential displacements. The stiffness of the diaphragm supports was therefore adjusted to yield differential displacements within 5% of the measured differential displacements (see Tables 4–6, 4–11, and 4–17). Tables 5–2 to 5–4 list the spring stiffnesses used, and the resulting vertical displacements and differential displacements at each diaphragm position for test specimens 1, 3, and 5, respectively. The change in diaphragm support stiffness resulted in a 2% increase in bottom fibre strain.

Since the cross-section dimensions were not obtained for test specimen 1, the effect of the web thickness and flange thickness on the bottom fibre strains and differential displacements were examined. The effect of an increase in web thickness of 0.05 mm, and an increase in flange thickness of 0.2 mm were both investigated. Although the increases in plate thickness were small, they were representative of the full range of measurements of the specimen dimensions (see Table 5–1). The model of test specimen 1, with the laboratory spring stiffness values, was used for the investigation. The small increase in web thickness had no significant effect on the bottom fibre strains or the differential displacements. The increase in flange thickness did decrease the bottom fibre strains and the differential displacements, but only marginally. The bottom fibre strain decreased by only 0.7% and the differential displacements decreased by an average of 1.6%. Therefore, the use of the average dimensions of specimen 3 for the finite element models of specimen 1 appears to be justified.

Another possible source for the observed discrepancy of the bottom fibre strain at midspan between the finite element analysis and the measured values is the actual connection of the reinforcing beam to the girder. The connection of the reinforcing beam to the girder required shims to close the gap between the top flange of the girder and the bottom flange of the reinforcing beam. The gap between the two flanges ranged from 0 to 13 mm, probably due to the permanent deformation of the girder while in service (Fraser *et al.*, 2000). This imperfection of the girder and the varying gap between the flanges were not modelled in the finite element analysis. A uniform gap of 10 mm between the test girder and the reinforcing beam was added to the model of test specimen 3, with laboratory spring stiffness values, to investigate the gap effect. The presence of the gap decreased the bottom fibre strain by about 1%, compared to the original model with no gap. The spring stiffnesses were then modified to obtain the correct differential displacements. The amount of required adjustment to the spring stiffness was similar to the amount required for the finite element model that did not have a gap between the reinforcing beam and the girder. Therefore, the use of the model without the uniform 10 mm gap appears satisfactory. The effect on the stresses in the web gap region will be discussed below.

5.3.2 Web Gap Stresses

The results from the finite element analyses of the three test specimens were used for the displacement boundary conditions for the substructure models described in Section 5.2. Since only one joint location in each of the laboratory tests was instrumented with strain rosettes, only these joints are used as a basis of comparison with the test results. These substructure models are Joint 11 in test specimen 1 (T1J11), Joint 12 in test specimen 3 (T3J12), and Joint 12 in test specimen 5 (T5J12). A comparison of the vertical stresses (in-plane stresses perpendicular to the axis of the specimen) obtained from the finite element analyses with those obtained from the strain rosette readings are shown in Figures 5–8 to 5–10. The stress values from the strain rosettes presented in the figures were calculated from the strain measurements. The stresses from the finite element analysis are shown along the lines 1–2, 1'–2', and 3–4. Along line 1–2 are the stresses on one side of the stiffener on both the west and east face of the web, whereas the

stresses on the other side of the stiffener on both the west and east face of the web are along line 1'–2'. Line 3–4 represents the stresses directly below the transverse stiffener.

Figures 5–8 to 5–10 show that there is reasonable agreement between the measured and calculated vertical stresses near the bottom of the web gap. The calculated vertical strains above the web gap were smaller than the measured values. A possible reason for the discrepancy between the predicted and measured strains is due to the large strain gradients that exist in the web gap region, shown in Figures 5–11 and 5–12. A small difference between the strain points in the numerical model and in the test specimens can therefore result in a significant difference in strain. Also, the finite element model does not include the stiffener-to-web and the web-to-flange fillet welds. The welds tend to increase the stiffness of the web in the gap region, thus causing greater strains for a given web gap distortion. Therefore, the strain gauge data is sensitive to the location of the strain gauge.

As mentioned previously, the effect of the gap between the reinforcing beam and girder on the web gap stresses was investigated. The results obtained from the test specimen model with the uniform 10 mm gap between the reinforcing beam and the girder were used as boundary conditions for T3J12. A comparison of the vertical stresses in the web gap region between the original T3J12 model and the one with the 10 mm gap boundary conditions indicates that the effect of the uniform 10 mm gap on the web gap stresses is minimal, as shown in Figure 5–13. Therefore, the use of finite element models without the gap between the reinforcing beam and the girder is validated.

5.3.3 Web Gap Distortions

The out-of-plane distortions from the experimental program are compared with the corresponding results from the substructure models in Table 5–5. In order to produce an out-of-plane distortion that can be compared with the measured distortion (refer to Figure 3–17), the predicted distortions are taken as the difference in out-of-plane displacement between the node in the web at the bottom of the web gap and the node at the bottom corner of the stiffener.

For the only joint with no crack, Joint 13 from specimen 3, there was good correlation between the analytical and the experimental distortions. The web gap distortions at the three joints with part-through-thickness cracks did not have as good a correlation as the joint with no crack. The predicted distortions at Joint 12 in specimen 1 and at Joint 10 in specimen 3 were approximately 0.4 mm smaller than the experimental results because the part-through-thickness crack was not modelled. However, the discrepancy between the predicted and experimental results for Joint 13 in specimen 1 is not known. A possible reason that the measured distortion at Joint 10 in specimen 1 was significantly smaller than the predicted distortion is that the through-thickness crack was modeled as a 0.5 mm gap between shell elements. The gap does not take into account any possible friction or bearing force transfer between the two crack surfaces.

5.3.4 Crack Initiation Sites

A comparison of primary crack initiation sites in the test specimens with the locations of maximum stresses in the web gap region predicted from the finite element analysis was only performed on test specimens 1 and 3 since test specimen 5 was repaired prior to fatigue testing.

As discussed in Chapter 4, the significant fatigue cracks were located at Joint 12 in both specimens 1 and 3. From the substructure models for the first test specimen, the maximum stress in the web gap region occurred at Joint 11, however. The calculated maximum tensile stress at Joint 11 was 153 MPa as compared to the maximum tensile stress of 134 MPa at Joint 12. A similar observation can be made for test specimen 3, where the calculated maximum tensile stress at Joint 11 was 177 MPa and the maximum tensile stress at Joint 12 was 143 MPa.

Although the finite element model predicts lower stresses at the joints where fatigue cracks started than at joints where no fatigue cracks were observed, the difference in peak stress at Joints 11 and 12 is not very large. An important factor that affects fatigue crack initiation, which was not considered in the finite element analysis, is the presence of local stress raisers such as the stiffener-to-web fillet welds, and local flaws that may have existed in the fillet welds. Although these are important features of the test specimens, it

was not practical to include them in the analysis. It is possible that these stress raisers would more than offset the difference in stresses calculated between joints 11 and 12. In summary, based on this analysis it is difficult to correlate the maximum web gap stresses of the test specimens to the fatigue crack initiation sites.

5.4 Results Of Analysis

The results from the finite element analysis of the test specimen and substructure models are presented below. The results include the investigation of the effect of three parameters on the behaviour of the web gap region, namely, the thickness of the bottom flange, the web gap length and the presence of stop holes. The analysis also investigated the rotation of the diaphragm, web gap distortion, and maximum stresses in the web gap region.

5.4.1 Effect of Increased Bottom Flange Thickness on Web Gap Behaviour

Lateral displacement and twisting of the bottom flange could affect the stresses in the web gap region. The thickness of the bottom flange was therefore increased (from 16.2 mm) in order to determine the effect of bottom flange stiffness on web gap stresses.

The analysis of Joint 12 in test specimen 3 indicates that the gap distortion decreased from 0.081 mm to 0.043 mm as the bottom flange thickness was increased from 16.2 mm to 38.0 mm. Figure 5–14 shows the out-of-plane deformation of the web for the models with the 16.2 mm bottom flange and the 38.0 mm bottom flange. The 16.2 mm thick bottom flange does not provide rigid support to the bottom of the web gap, of course. However, the web rotation at the flange to web junction and the out-of-plane displacement of the bottom flange were reduced considerably with the increase in flange thickness. Figure 5–14 also shows that the stiffener does not provide full rotational restraint to the top of the web gap.

The maximum tensile vertical and horizontal (in-plane stress parallel to the axis of the specimen) stresses in the web gap were 68 MPa and 94 MPa, respectively, for the 38.0 mm bottom flange. The 16.2 mm bottom flange had maximum tensile vertical and horizontal stresses of 102 MPa and 143 MPa, respectively. From the analytical

distortions, Equation 2–1 yields maximum stresses in the web gap region of 95 MPa and 179 MPa for the 38.0 mm and 16.2 mm bottom flanges, respectively. The stress predicted from beam theory is conservative compared to the maximum vertical stress for both bottom flange thicknesses. However, beam theory over predicts the horizontal stress by 26% for the 16.2 mm bottom flange but only 1% for the 38.0 mm bottom flange. Theses horizontal stresses develop due to the curvature of the web in the longitudinal direction, as shown in Figure 5–15. It should be noted that the stress calculated by simple beam theory is vertical and the horizontal stress is not accounted for.

5.4.2 Effect of Gap Length on Web Gap Stresses

As mentioned in Chapter 2, an increase in web gap length is considered as a possible rehabilitation method for distortion-induced fatigue cracks. The increase in web gap length could not be examined in the experimental program. Therefore, the finite element models will be used to provide insight into the effectiveness of cutting back the stiffener as a rehabilitation option.

The substructure model of Joint 12 from test specimen 3 (T3J12) was used to examine the effects of various gap lengths on the maximum stresses in the web gap region. To change the length of the stiffener, a row of shell elements was added or subtracted from the stiffener in the substructure model. The change in length of the web gap depended on the height of the existing shell elements in the web. For a zero gap length, the bottom nodes of the stiffener were not attached to the nodes in the bottom flange, thereby allowing for a zero gap length with no connection between the stiffener and the bottom flange. All new substructure models were loaded with the same support displacements and rotations that were used in the original substructure model.

Figures 5–15 and 5–17 show the maximum vertical and horizontal stresses, respectively, in the web gap region for gap lengths varying from 0 to 102 mm. The figures indicate that an increase of the gap length from 51 mm (as in the specimens tested) to 102 mm produces a 50% reduction in vertical stress both at the top and bottom of the web gap and a 70% reduction in horizontal stress at the top of the web gap. The horizontal stresses at

the bottom of the web gap are not significantly affected by a change in web gap length because the horizontal stresses are governed by the in-plane bending of the girder.

For short gap lengths, less than 21 mm, the stresses in the web gap region are found to increase with an increase in web gap length. Figures 5–16 and 5–17 indicate that web gap stresses are maximum when the web gap length is in the range of 10 mm to 25 mm. The effectiveness of a web gap length increase as a rehabilitation does not appear adequate for girders with small web gaps, which are found in some bridges built prior to the use of the 1983 AASHTO Bridge Specifications.

Table 5–6 lists a comparison of the web gap stresses for various web gap lengths with the maximum stress calculated using Equation 2–1 and the analytical distortions. The finite element analysis distortions are taken as the change in out-of-plane displacement of the nodes in the web at the top and bottom of the web gap. The beam model predicts conservative results for the vertical stresses for the investigated gap lengths. However, the amount of conservatism decreases with decreasing gap length. As mentioned previously, the horizontal stresses in the web gap are larger than the vertical stresses and the beam model predicts unconservative stresses compared to the maximum horizontal stresses in the web gap region for small gap lengths.

Current AASHTO (1998) and CSA-S6 (CSA, 2000) requirements for transverse stiffeners connected to diaphragms state that the stiffener must be attached to both flanges. To assess the effect of attaching the stiffened to the bottom flange, the model of Joint 12 from specimen 3 with a zero web gap opening was modified, connecting the nodes along the bottom of the stiffener to the corresponding nodes of the bottom flange. The results from this model were then compared to the results of the T3J12 model with zero gap length and no connection of the stiffener to the bottom flange. The maximum vertical stress in the web decreased from 34 MPa to 13 MPa near the stiffener-to-flange junction. The maximum horizontal stress (48 MPa) was similar to the maximum horizontal stress at the bottom of the web for the unattached stiffener, because the horizontal stresses are governed by in-plane bending of the girder. Therefore, the connection of the transverse stiffener to the bottom flange significantly decreased the

vertical stresses in the web near the stiffener-to-flange connection. Vertical and horizontal stresses for the stiffener connected to the bottom flange are presented in Figures 5–18 and 5–19, respectively.

A comparison of the analysis results for the attached stiffener case with the 51 mm gap detail gives an indication of the change in behaviour of the web gap region associated with the repairs used in the laboratory. A comparison of Figures 5–18 and 5–19 with Figures 5–11 and 5–12 indicate a significant stress decrease (approximately 90%) at the top of the 51 mm web gap when the web gap is bridged. Although horizontal stresses also decreased (approximately 50%) the decrease is not as significant as the decrease in the vertical stresses.

5.4.3 Effect of Stop Holes on Web Gap Stresses

As expected, the substructure model analyses showed that the stress distribution in the web gap region was altered by the presence of a through-thickness crack extending between stop holes. The finite element model T3J10 was used to examine the effect of the stop holes. It should be noted that, as in the test specimen, one stop hole in this substructure model was located 6 mm higher above the bottom flange and 3 mm further from the stiffener than the other stop hole. The model was modified by the addition of a 0.5 mm separation between the shell elements below the stiffener to model the through-thickness crack. Another model was developed without a through-thickness crack or stop holes in order to investigate the web gap stresses at the joint location prior to cracking. For comparison, the boundary conditions in both joint models were the same as those used in the original T3J10 model.

The vertical and horizontal stresses for the specimen with stop holes joined by a through-thickness crack are presented in Figures 5–20 and 5–21, respectively. The stress distribution from T3J10 with no stop holes was similar to the stress distribution at Joint 12 of specimen 3, shown in Figures 5–11 and 5–12. A comparison of the results from the two modified T3J10 models indicates that a large change in the maximum vertical stress occurred at the base of the web gap. The presence of the through-thickness

crack extending between stop holes decreased the maximum vertical compressive stress at the bottom of the web gap from 100 MPa down to 46 MPa.

Figures 5–20 and 5–21 show that large stresses occur at both the top and bottom of the stop holes. The large vertical and horizontal stresses present at the top of the stop holes appear to validate the observation that fatigue cracks initiated past the stop holes. These large stresses at the top of the stop holes were similar to the location of the initiation of upward fatigue cracks observed during laboratory fatigue testing. Although the presence of welds and weld flaws often dictates the location of fatigue crack initiation, modelling of the stiffener to web fillet welds and weld flaws was beyond the scope of this study.

The stresses at the bottom of the stop holes were consistent with the observed fatigue cracks that propagated downwards from the stop holes in some of the specimens tested. The observed fatigue cracks that propagated downwards began as through-thickness cracks. The analysis supports this observation, since large horizontal stresses occur at the bottom of the stop holes, whereas the vertical stresses at the bottom of the stop hole are relatively small. The downward fatigue crack initiation sites were not at the very bottom of the stop holes; however, the initiation of the cracks may have been influenced by local imperfections on the surface of the stop hole.

The analysis supports the experimental observations that stop hole drilling is an ineffective rehabilitation for distortion-induced fatigue cracks. This corroborates the suggestion of Lai (1997) that Equation 2–2 is not valid for fatigue cracks caused by out-of-plane web distortions since only Mode I is considered in the equation.

5.4.4 Differential Displacement and Web Gap Distortion

One of the objectives of the finite element study was to investigate the possibility of predicting the web gap distortion accurately using calculated or measured differential displacements between adjacent girders. The calculated web gap distortion is taken as the product of the diaphragm rotation and the distance from the base of the stiffener to the point of rotation along the length of the stiffener. The diaphragm rotation is simply obtained as the differential displacement between two adjacent girders divided by the

length of the diaphragm. The difficulty in the problem is that the location of the point of rotation of the diaphragm is not well defined. This is investigated following.

Results from the test specimen models were used to obtain the point of rotation of the stiffeners. Table 5–7 lists the points of rotation from the test specimen models for the joints in the constant moment region. Figure 5–22 shows the out-of-plane displacement of the stiffeners at joints 10 to 13 of test specimen 3. The difference in location of the points of rotation illustrated in Figure 5–22 is explained by the fact that the top flange of the girder was braced laterally near joints 10 and 13. The lateral restraint forced the rotation of the stiffener to take place about a point near the height of the lateral brace. Away from the braced point, however, the point of rotation is generally located below the brace point since the top flange is free to move laterally. In practice the point of rotation would be at the top of the stiffener, since the concrete slab would provide continuous lateral support to the top of the girder. The unusual displacements over the bottom 100 mm of the stiffener can be explained by the change in out-of-plane stiffness from the diaphragm to the stiffener, which occurred 101 mm above the bottom of the stiffener.

The points of rotation in Table 5–7 and the differential displacements from Tables 5–2, 5–3, and 5–4 for Joint 11 from test specimen 1, Joint 12 from test specimen 3, and Joint 12 from test specimen 5, respectively, were used to predict web gap distortions of 0.226 mm, 0.236 mm, and 0.183 mm, respectively. These predicted distortions are approximately 250% greater than distortions obtained from the finite element analysis, shown in Table 5–7.

5.4.5 Prediction of Stresses in Web Gap Region

As discussed in Chapter 2, simple beam theory is used frequently to calculate the maximum stress in the web gap region. Results from three substructure models will be used to investigate the ability of simple beam theory to predict maximum stresses in the web gap region. The designation of the web gap detail as a fatigue Category C' detail will also be investigated.

Table 5–8 lists the comparison of the stresses obtained from the finite element analysis with the stresses calculated with Equation 2–1 using both the predicted and analytical web gap distortions. Both the maximum vertical and horizontal stresses from the finite element analysis are presented because before cracking of the web the stresses that govern the crack initiation stage, at the toe of the weld located at the base of the stiffener, would be the vertical stresses. However, once the crack becomes vertical, along the toe of the vertical welds, the horizontal stresses become important.

The stresses calculated from the predicted web gap distortions are very conservative as compared to the finite element analysis results. The stresses calculated manually were more than 430% greater than the maximum vertical stresses and more than 325% greater than the maximum horizontal stresses from the analysis. For a given distortion the calculated stresses were marginally conservative compared to the finite element analysis stresses. The rotation and lateral displacement of the bottom flange, and the flexibility of the stiffener are the reasons that the calculated stresses are approximately 75% greater than the maximum vertical stresses predicted by the finite element analysis.

To assess the designation of the web gap detail as Category C', the stresses calculated from beam theory in Table 5–8 for specimens 1 and 3 were used to determine the fatigue life. The stresses calculated from the predicted distortion yield a fatigue life of less than 100 000 cycles for both specimens. The stresses calculated using the distortion obtained from the finite element analysis yield a fatigue life of approximately 300 000 cycles for the specimens. Since the laboratory fatigue life of both specimens was greater than 2.5 million cycles, the Category C' designation appears to be very conservative. Even the maximum stresses obtained from the finite element analysis yield a fatigue life of approximately 800 000 cycles.

The stresses calculated from Equation 2–1 using the predicted web gap distortion were significantly larger than maximum tensile stress from the finite element analysis. Therefore, the predicted distortion yields a very conservative fatigue life prediction for the tested specimens and the fatigue Category C' designation is adequate. From the parametric study the amount of conservatism of the beam equation, using the analytical

distortions, was small for small gap lengths and thick bottom flanges. Hence, the use of predicted web gap distortions and the Category C' designation may result in less conservative fatigue life predictions for bridge girders with short web gaps, and flanges and stiffeners that provide rigid support to the top and bottom of the web gap.

5.5 SUMARY

Finite element models were developed and validated using the laboratory tests results presented in Chapter 4. The validated finite element models were used to conduct a parametric study in which some factors affecting the behaviour of the web gap region were investigated. The parametric study examined the effects of the change in thickness of the bottom flange, the change in length of the web gap, and the presence of through-thickness cracks joining stop holes on the stresses in the web gap region. The findings from the finite element analysis and the parametric study can be summarized as follows:

1. The transverse stiffener and the bottom flange did not provide rigid support to the top and bottom of the web gap. For a given gap distortion, the simple beam theory predicts larger stresses than obtained from the finite element analysis.

2. The web gap distortions and stresses calculated directly from the corresponding differential displacements were very conservative. Therefore, the use of the Category C' designation for the web gap detail provided very conservative estimates of the fatigue life for the specimens tested.

3. An increase in bottom flange thickness from 16.2 mm to 38.0 mm resulted in web gap behaviour similar to beam theory. The maximum web gap stress predicted was approximately equal to the maximum horizontal stress from the finite element analysis of the thick bottom flange for the same web gap distortion.

4. Changing the web gap length from 51 mm to 102 mm significantly decreased the maximum stresses in the web gap region. However, for short web gaps (less than 21 mm) an increase in web gap length did not significantly affect the web gap stresses.

5. From the analytical web gap distortion, beam theory predicted a maximum stress that was approximately 90% of the maximum horizontal stress obtained from the finite element analysis for a web gap length of 21 mm.

6. The analysis of a through-thickness crack extending between stop holes determined that there are large vertical and horizontal stresses at the top of the stop holes. The large stresses were consistent with the observation that the upward fatigue cracks initiated past the stop holes in the tested specimens.

7. Large horizontal stresses found at the bottom of the stop holes for the web gap with a through-thickness crack extending between stop holes were consistent with the downward through-thickness fatigue cracks observed in the specimens tested.

Table 5–1

Test Specimen Dimensions

Specimen	Dimension	Average (mm)	Standard Deviation (mm)	Range (mm)
3	Flange Thickness	16.15	0.04	0.16
	Web Thickness	9.60	0.02	0.05
	Flange Width	254	0.7	3
	Girder Height	949	0.6	4
4	Flange Thickness	16.13	0.07	0.22
	Web Thickness	9.62	0.02	0.05
	Flange Width	254	0.8	4
	Girder Height	948	0.7	5
5	Flange Thickness	16.15	0.08	0.22
	Web Thickness	9.60	0.02	0.05
	Flange Width	254	0.7	3
	Girder Height	949	0.8	3

Table 5–2

Diaphragm Supports Stiffness and Predicted Displacements, Test Specimen 1
(193 kN/actuator)

Joint*	Spring Stiffness (N/mm)	Vertical Displacement (mm)	Differential Displacements Designation	Displacement (mm)
3	800	-3.55		
			Δ_{9-3}	-0.09
9		-3.64		
4	800	-4.86		
			Δ_{11-4}	-0.31
11		-5.16		
5	1680	-3.78		
			Δ_{13-5}	-0.53
13		-4.31		
6	1260	-1.03		
			Δ_{15-6}	-0.10
15		-1.13		
8		-1.13		
			Δ_{8-17}	-0.11
17	1100	-1.02		
10		-4.32		
			Δ_{10-18}	-0.54
18	1145	-3.78		
12		-5.16		
			Δ_{12-19}	-0.40
19	875	-4.76		
14		-3.63		
			Δ_{14-20}	-0.28
20	1250	-3.35		

* Refer to Figure 3–4 for joint location.

Table 5–3

Diaphragm Supports Stiffness and Predicted Displacements,
Test Specimen 3
(196 kN/actuator)

Joint*	Spring Stiffness (N/mm)	Vertical Displacement (mm)	Differential Displacements Designation	Displacement (mm)
3	1265	-3.48		
			Δ_{9-3}	-0.22
9		-3.70		
4	785	-4.95		
			Δ_{11-4}	-0.31
11		-5.27		
5	1050	-4.03		
			Δ_{13-5}	-0.38
13		-4.41		
6	3125	-0.81		
			Δ_{15-6}	-0.34
15		-1.15		
8		-1.15		
			Δ_{8-17}	-0.35
17	3740	-0.80		
10		-4.40		
			Δ_{10-18}	-0.49
18	1350	-3.91		
12		-5.27		
			Δ_{12-19}	-0.31
19	715	-4.96		
14		-3.71		
			Δ_{14-20}	0.00
20	676	-3.71		

* Refer to Figure 3–4 for joint location.

Table 5–4

Diaphragm Supports Stiffness and Predicted Displacements,
Test Specimen 5
(152 kN/actuator)

Joint*	Spring Stiffness (N/mm)	Vertical Displacement (mm)	Differential Displacements	
			Designation	Displacement (mm)
3	975	-2.84		
			$\Delta_{9\text{-}3}$	-0.04
9		-2.88		
4	830	-3.87		
			$\Delta_{11\text{-}4}$	-0.23
11		-4.10		
5	950	-3.04		
			$\Delta_{13\text{-}5}$	-0.39
13		-3.42		
6	3600	-0.61		
			$\Delta_{15\text{-}6}$	-0.29
15		-0.90		
8		-0.89		
			$\Delta_{8\text{-}17}$	-0.34
17	3600	-0.55		
10		-3.42		
			$\Delta_{10\text{-}18}$	-0.35
18	1010	-3.07		
12		-4.10		
			$\Delta_{12\text{-}19}$	-0.26
19	825	-3.84		
14		-2.89		
			$\Delta_{14\text{-}20}$	-0.02
20	830	-2.86		

* Refer to Figure 3–4 for joint location.

Table 5–5

Web Gap Distortion Comparison

Test Specimen	Joint*	FEA Web Gap Distortion** (mm)	Experimental Web Gap Distortion[†] (mm)	Type of Crack at Joint
	10	0.24	0.10	Through-thickness
1	12	0.12	0.16	Part-through-thickness
	13	0.18	0.09	Part-through-thickness
3	10	0.16	0.21	Part-through-thickness
	13	0.12	0.11	No crack

* Refer to Figure 3–4 for joint location.

** Calculated from node displacements at bottom of web gap and bottom of transverse stiffener (Includes change in width of stiffener).

[†] Only joints with web gap distortion measurements are presented.

Table 5–6

Beam Theory and Finite Element Analysis Stresses for Various Web Gap Lengths

Gap Length (mm)	FEA Web Gap Distortion* (mm)	Beam Theory Stress (MPa)	Vertical Stress		Horizontal Stress	
			FEA Maximum Tensile Stress (MPa)	Beam Theory FEA	FEA Maximum Tensile Stress (MPa)	Beam Theory FEA
21	0.071	156.3	136.7	1.14	178.7	0.87
51	0.081	179.3	102.1	1.76	142.6	1.26
102	0.050	110.4	49.6	2.23	98.0	1.13

* Calculated from node displacements in web at bottom and top of web gap.

Table 5–7

Stiffener Points of Rotation and Web Gap Distortions from
Finite Element Analysis

Specimen	Joint*	Point of Rotation[†] (mm)	Web Gap Distortion** (mm)
	10	941	0.232
	11	722	0.094
1	12	710	0.107
	13	927	0.158
	10	950	0.139
	11	738	0.097
3	12	743	0.081
	13	979	0.100
	10	964	0.063
	11	709	0.079
5	12	699	0.074
	13	956	0.131

* Refer to Figure 3–4 for joint location.

** Calculated from node displacements in web at bottom and top of web gap.

[†] Measured from bottom of transverse stiffener.

Table 5-8

Beam Theory and Finite Element Analysis Stresses Comparison

Test Specimen and Joint	Predicted Web Gap Distortion (mm)	Beam Theory[1] Stress (MPa)	FEA Web Gap Distortion (mm)	Beam Theory[2] Stress (MPa)	Vertical Stress			Horizontal Stress		
					FEA Maximum Tensile Stress (MPa)	$\frac{\text{Beam Theory}^1}{\text{FEA}}$	$\frac{\text{Beam Theory}^2}{\text{FEA}}$	FEA Maximum Tensile Stress (MPa)	$\frac{\text{Beam Theory}^1}{\text{FEA}}$	$\frac{\text{Beam Theory}^2}{\text{FEA}}$
T1, J11	0.226	496.1	0.094	206.4	115.0	4.31	1.79	152.5	3.25	1.35
T3, J12	0.236	523.4	0.081	179.3	102.1	5.13	1.76	142.6	3.67	1.26
T5, J12	0.183	405.1	0.074	164.1	93.7	4.32	1.75	123.7	3.28	1.33

Note: Beam Theory[1] refers to calculations performed with the predicted distortions

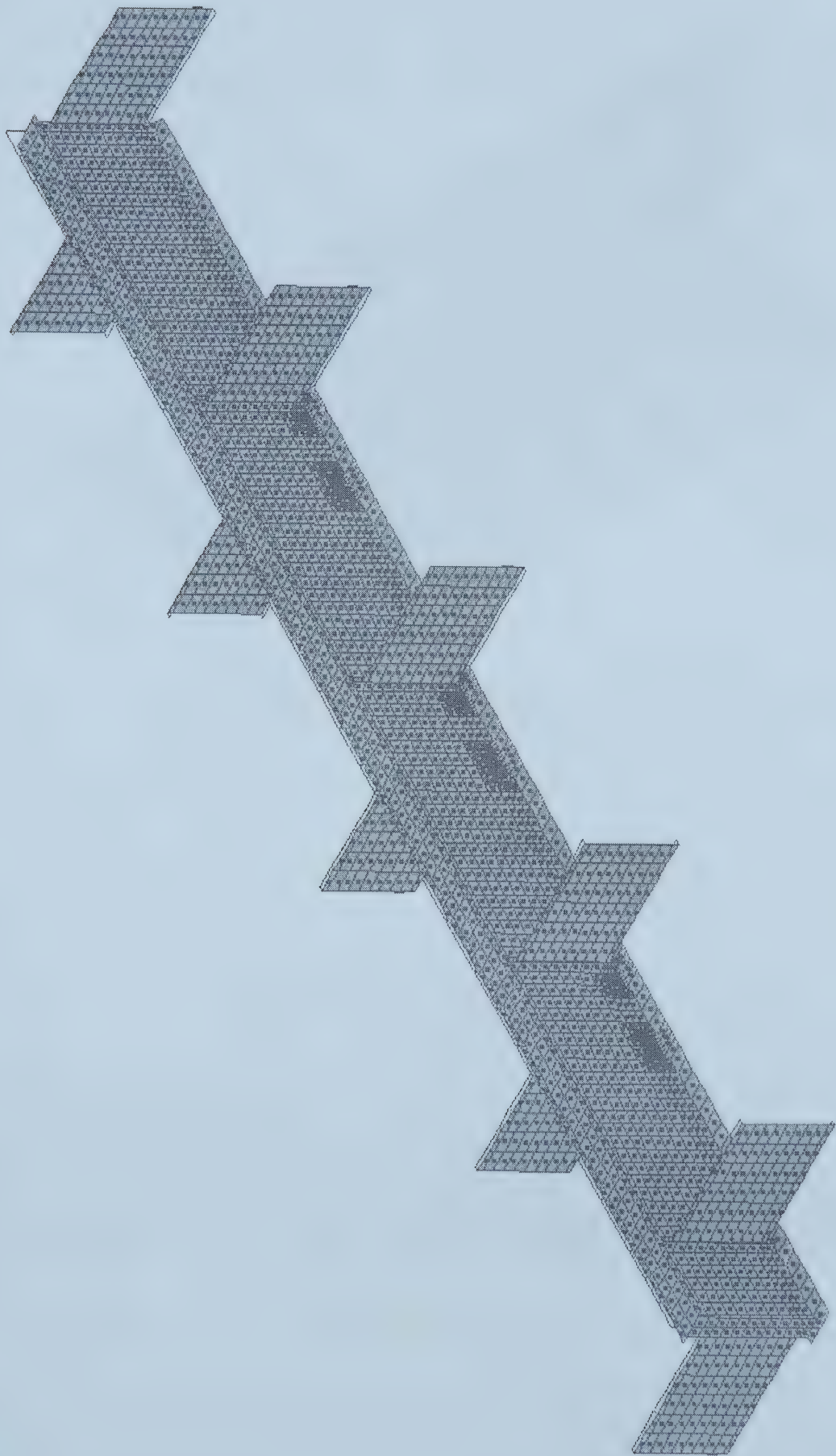Beam Theory[2] refers to calculations performed with the FEA distortions

130

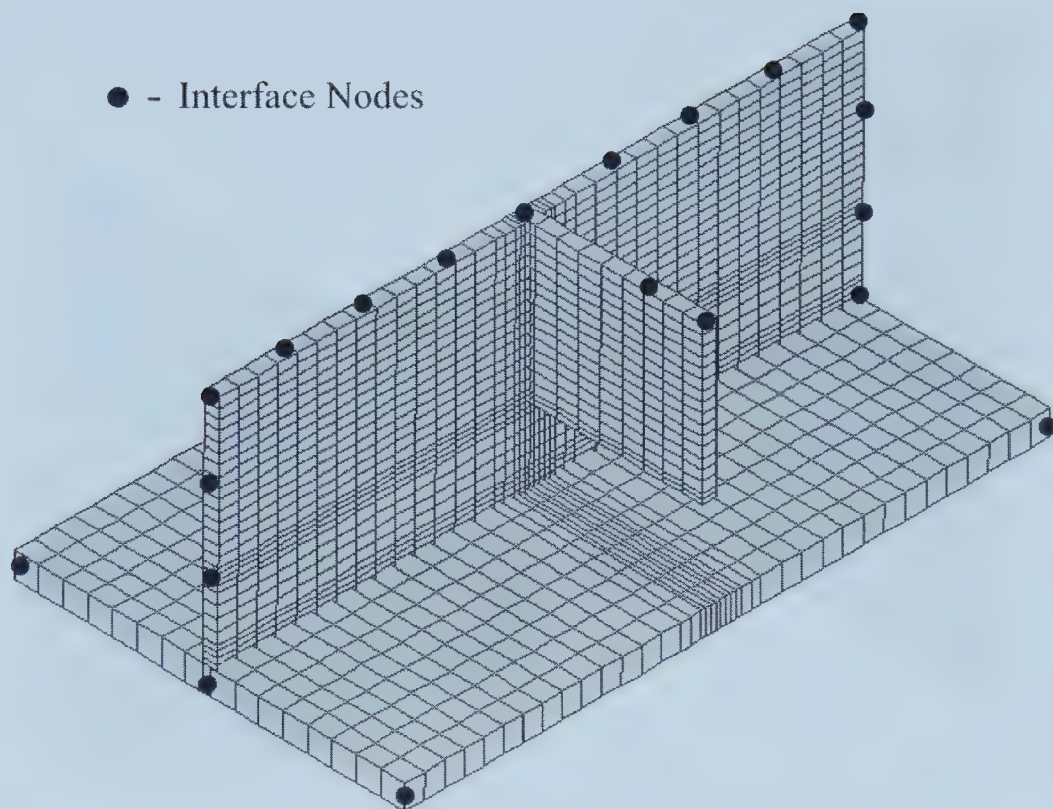**Figure 5–1** Typical Finite Element Model of Test Specimen

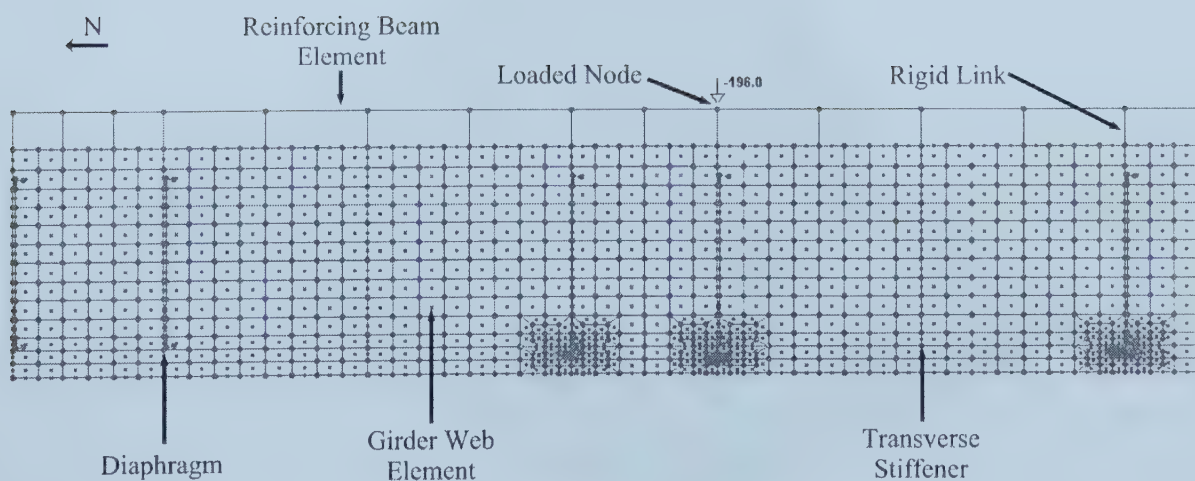**Figure 5–2** Web Gap Substructure

Figure 5–3 Partial Elevation of Typical Test Specimen Model
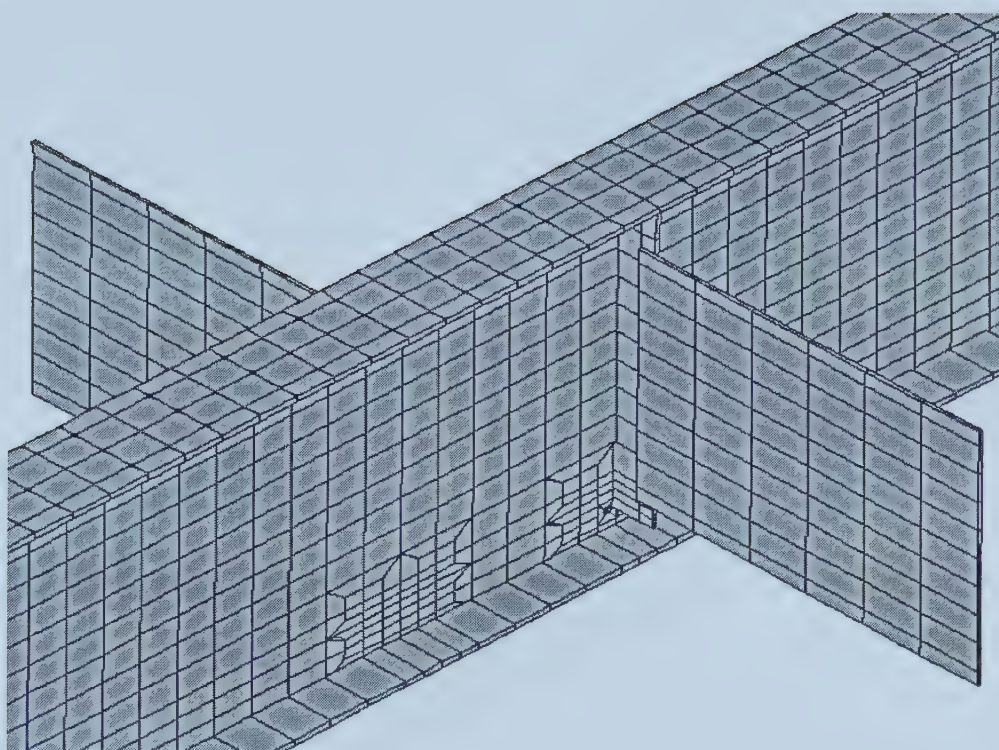(from North End to Midspan)

Figure 5–4 Typical Refinement of Test Specimen Model
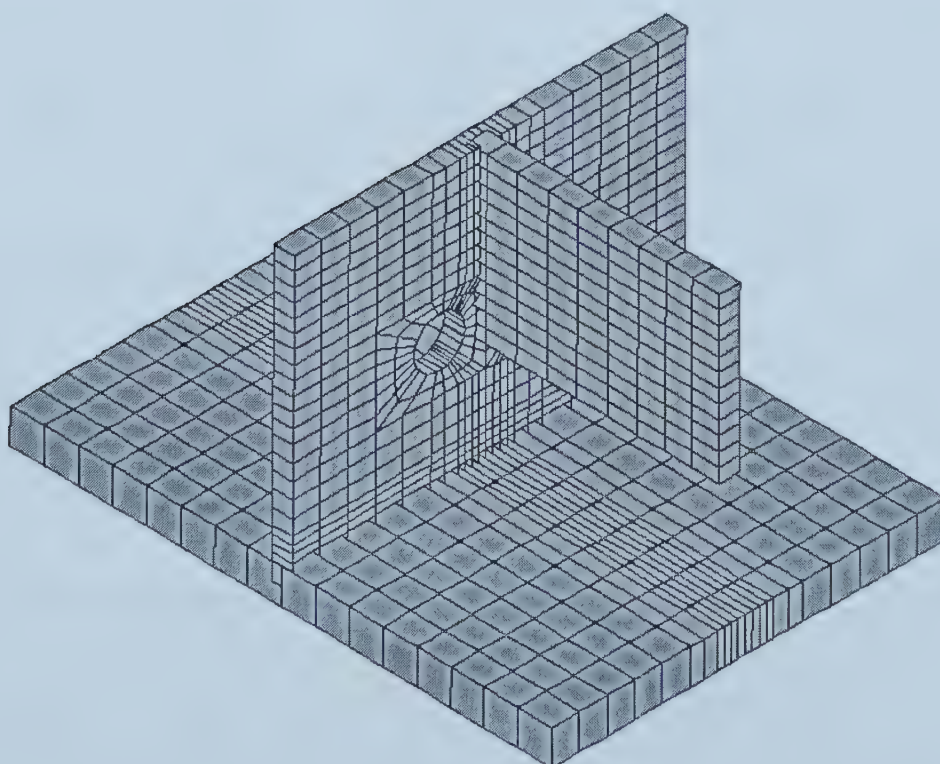(Reinforcing Beam Not Shown)

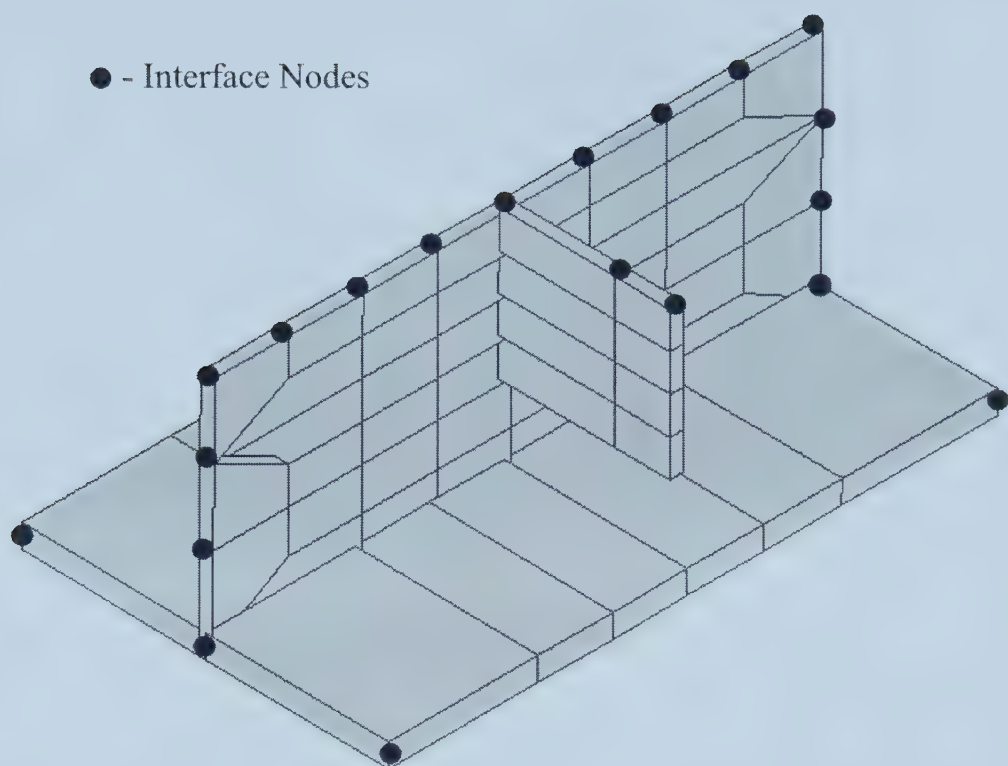**Figure 5–5** Refined Mesh of Web Gap with Stop Holes

133

Figure 5–6 Coarse Mesh of Web Gap Substructure before Mesh Refinement
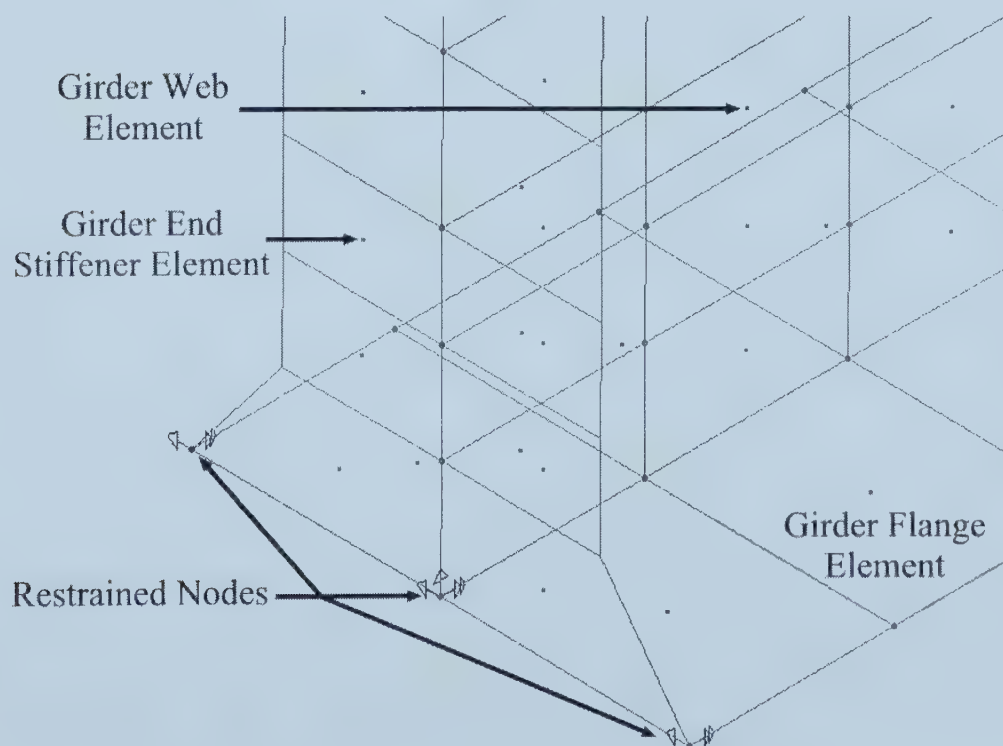

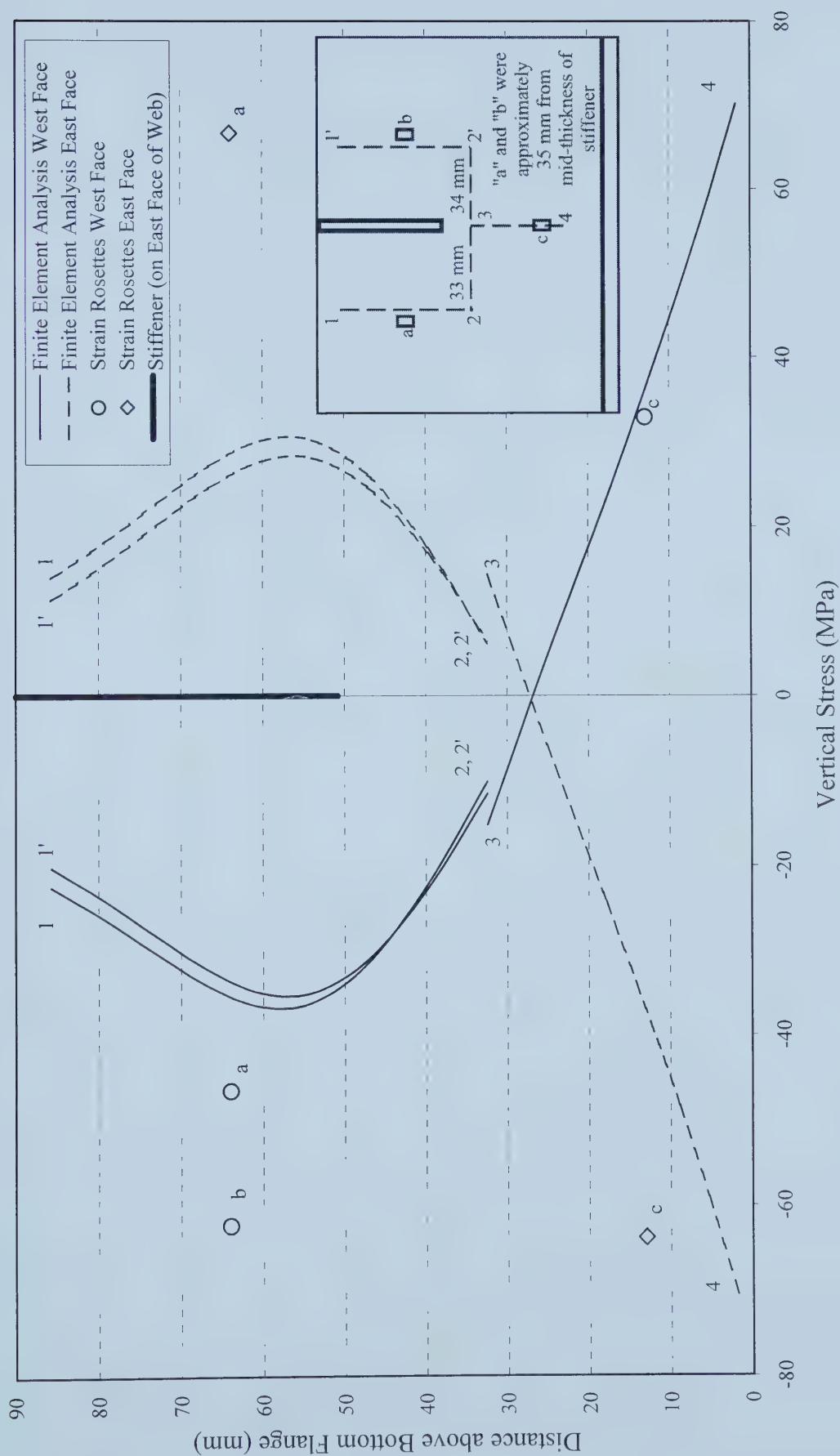**Figure 5–7** Restrained Degrees of Freedom at Girder End Support

Figure 5–8 Vertical Stress Comparison in Web Gap Region of Joint 11, Specimen 1
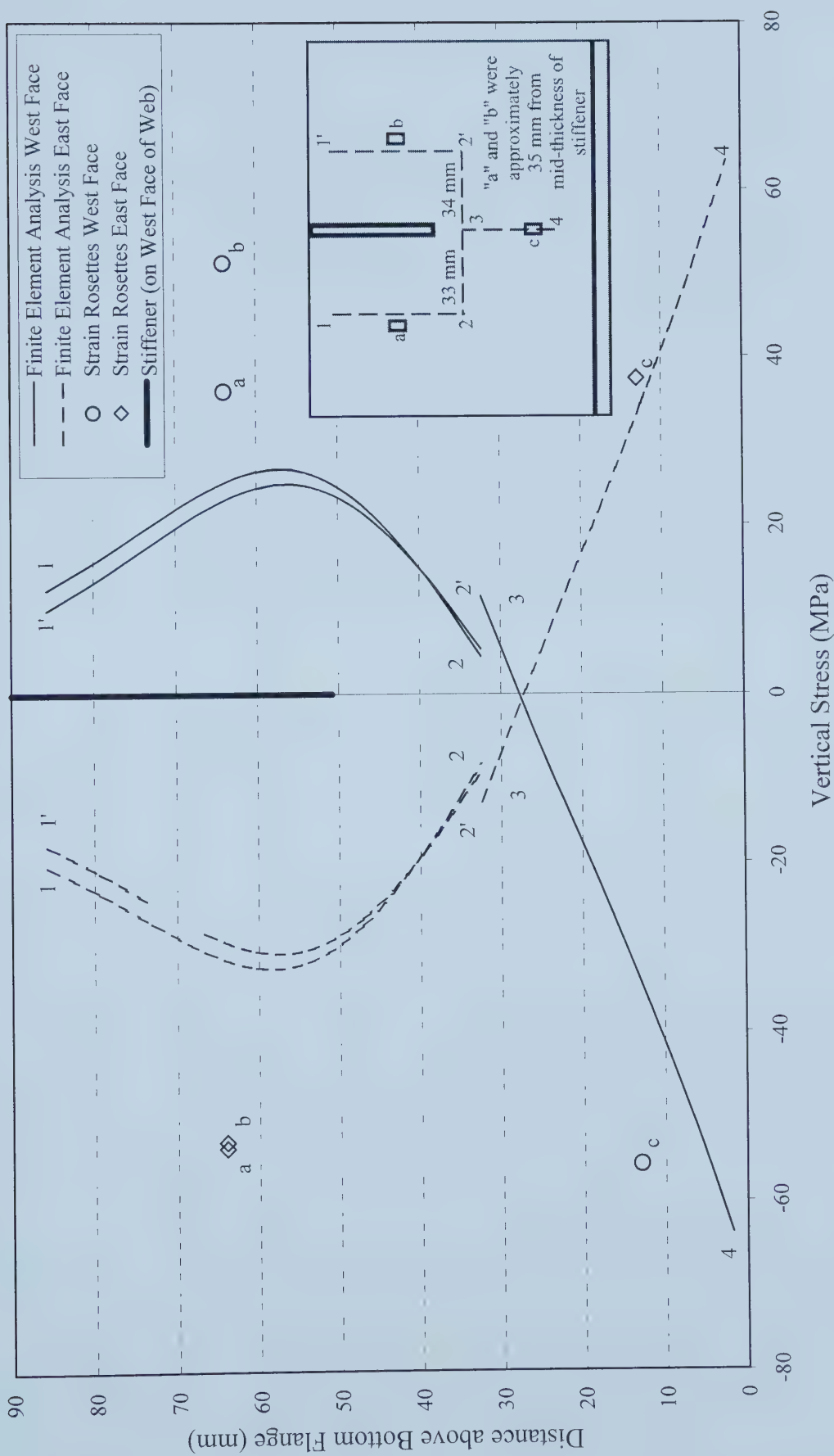
135

Figure 5-9 Vertical Stress Comparison in Web Gap Region of Joint 12, Specimen 3
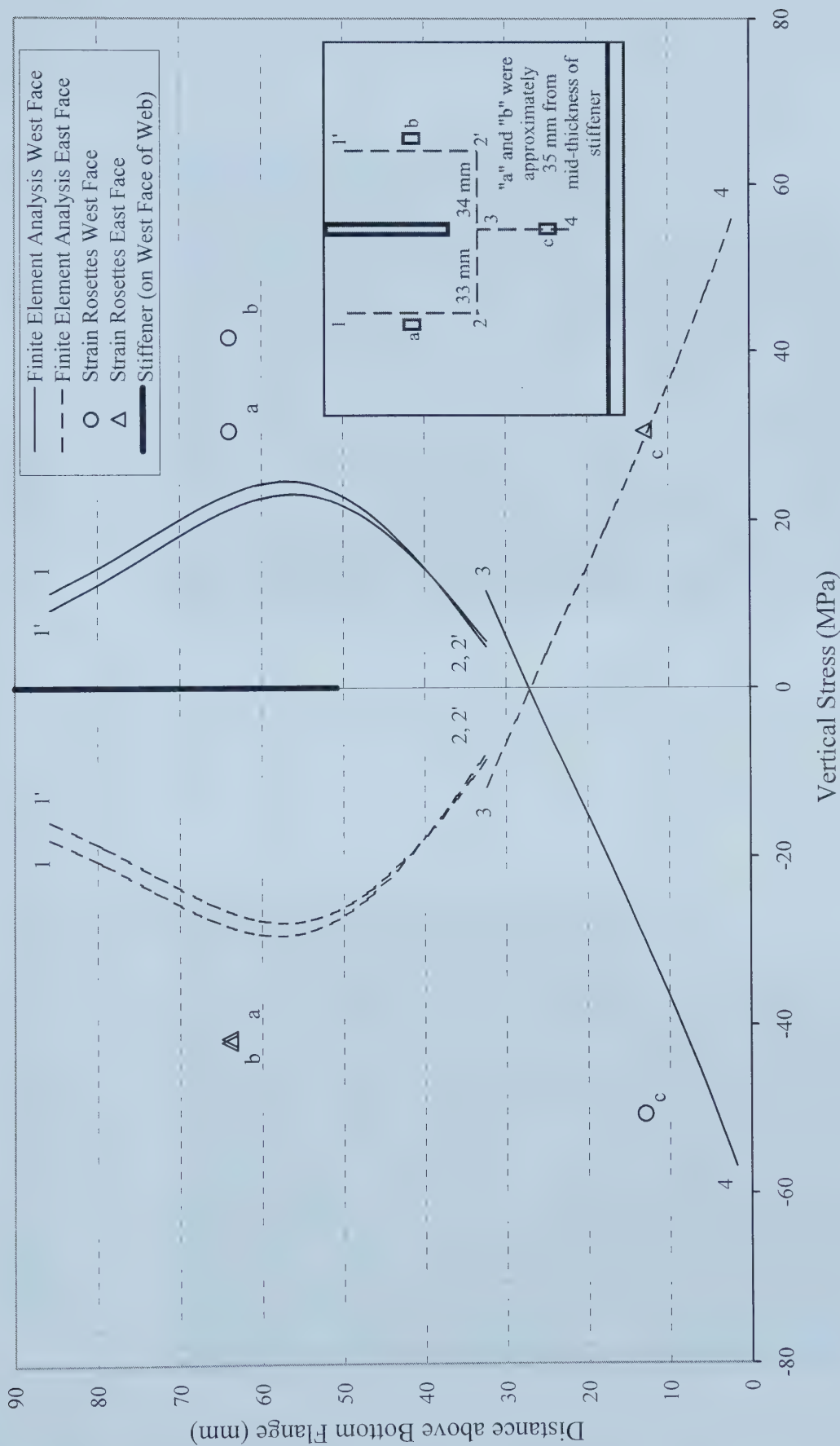
136

Figure 5–10 Vertical Stress Comparison in Web Gap Region of Joint 12, Specimen 5

137
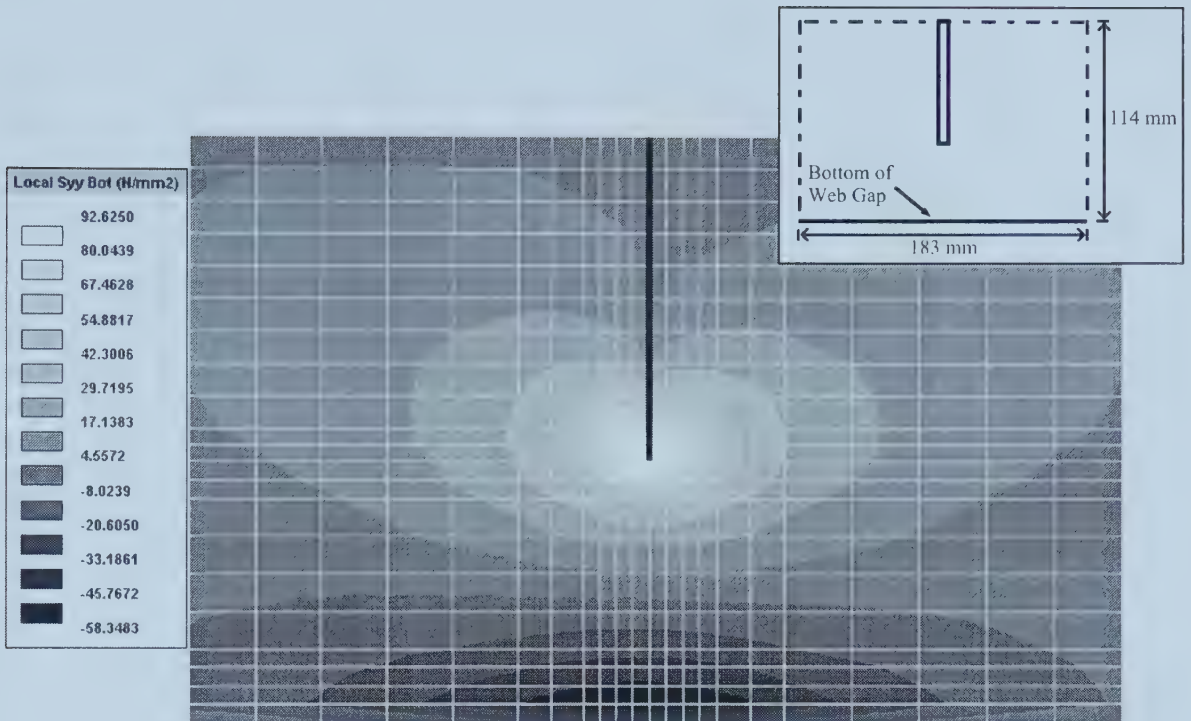
Figure 5–11 Vertical Stresses in Web Gap Region at Joint 12, Test Specimen 3
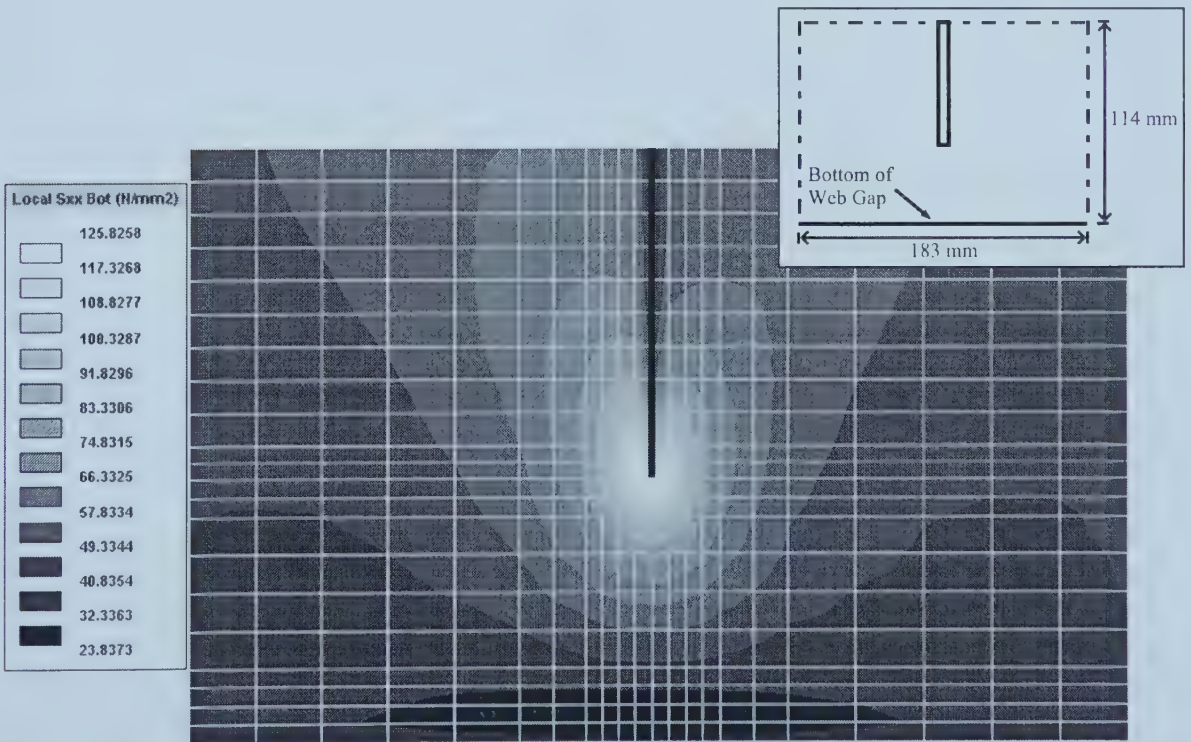
Figure 5–12 Horizontal Stresses in Web Gap Region at Joint 12, Test Specimen 3

138
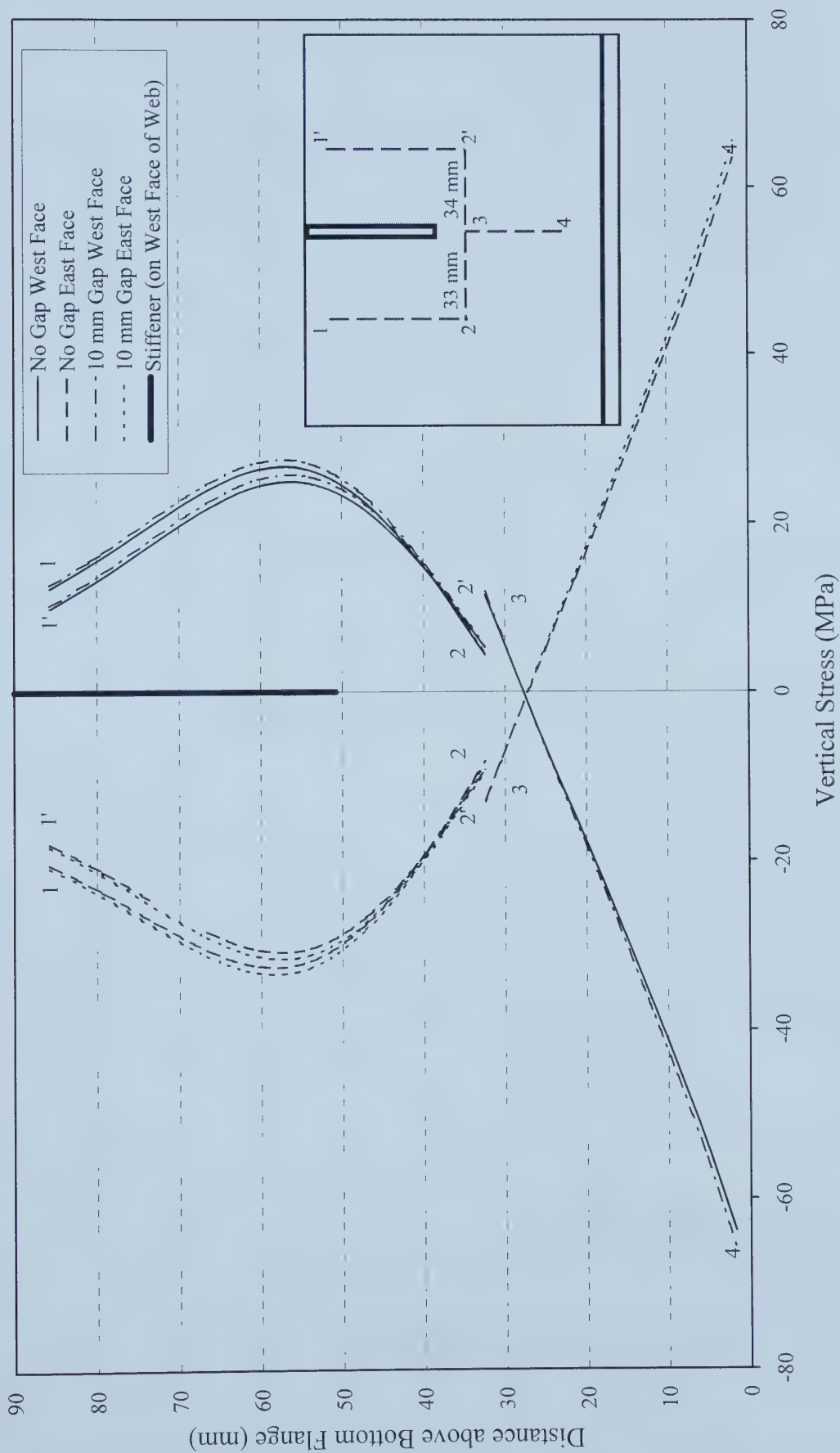
Figure 5–13 Vertical Stress Comparison in Web Gap Region to Determine Effect of 10 mm Gap Between Reinforcing Beam and Girder

Legend (graph):
- No Gap West Face
- No Gap East Face
- 10 mm Gap West Face
- 10 mm Gap East Face
- Stiffener (on West Face of Web)

Y-axis: Distance above Bottom Flange (mm)

X-axis: Vertical Stress (MPa)

Inset labels: 33 mm, 34 mm

139
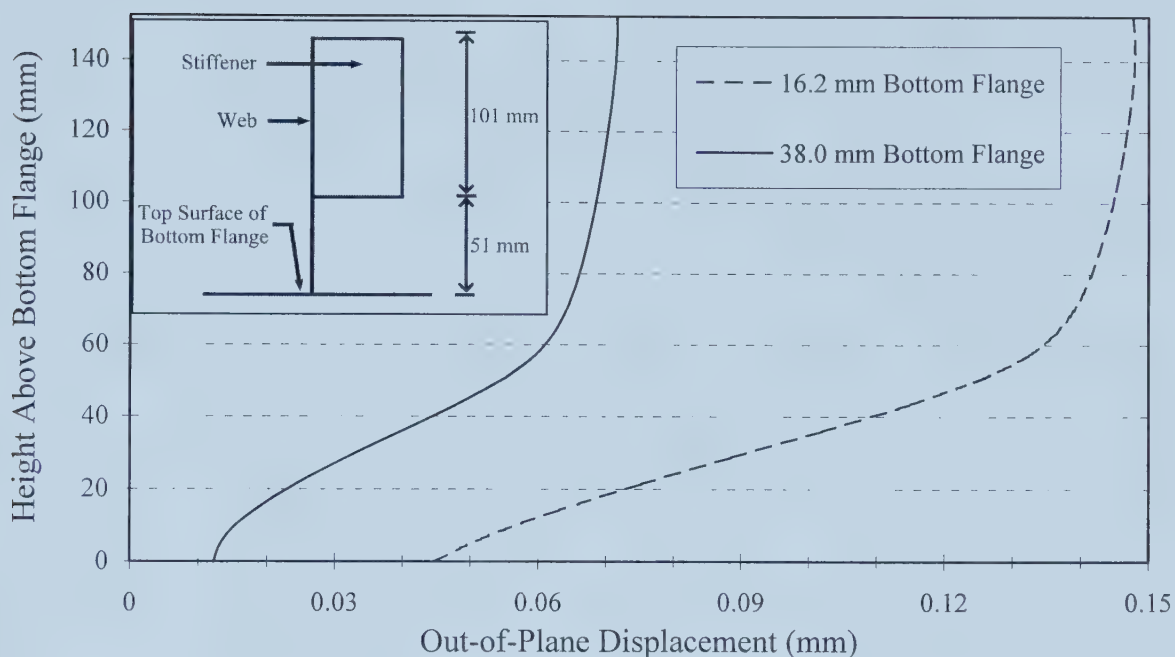
Figure 5–14 Out-of-Plane Web Displacement Comparison for T3J12 with 38.0 mm Bottom Flange and 16.2 mm Bottom Flange
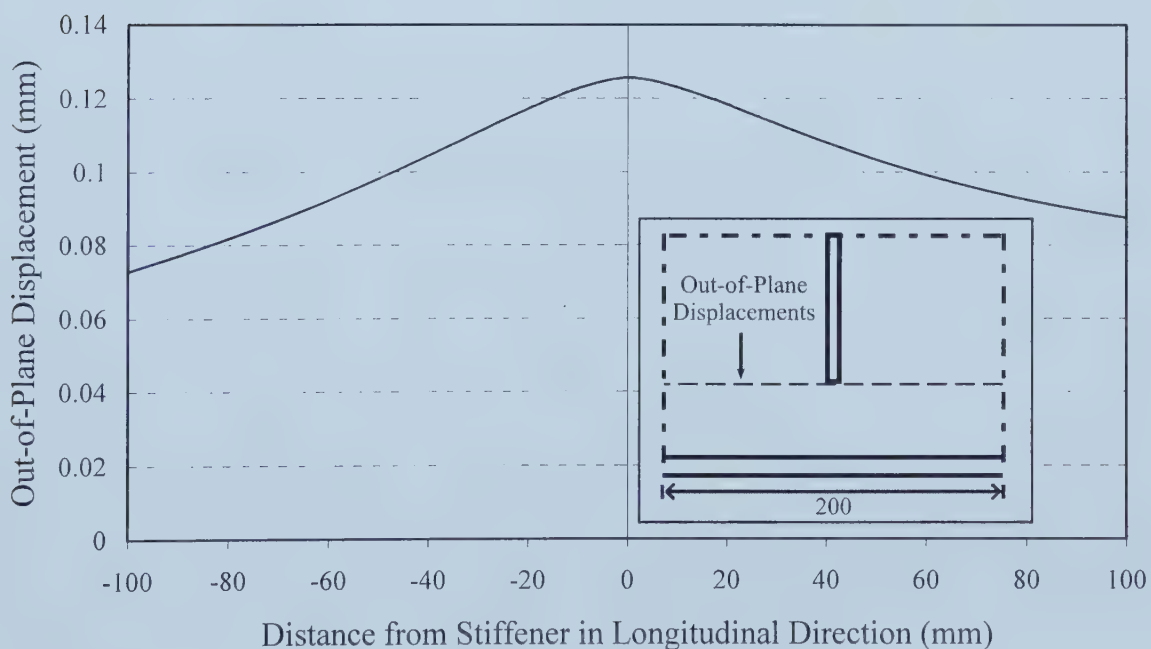
Figure 5–15 Out-of-Plane Displacement of Web Along Longitudinal Axis, T3J12
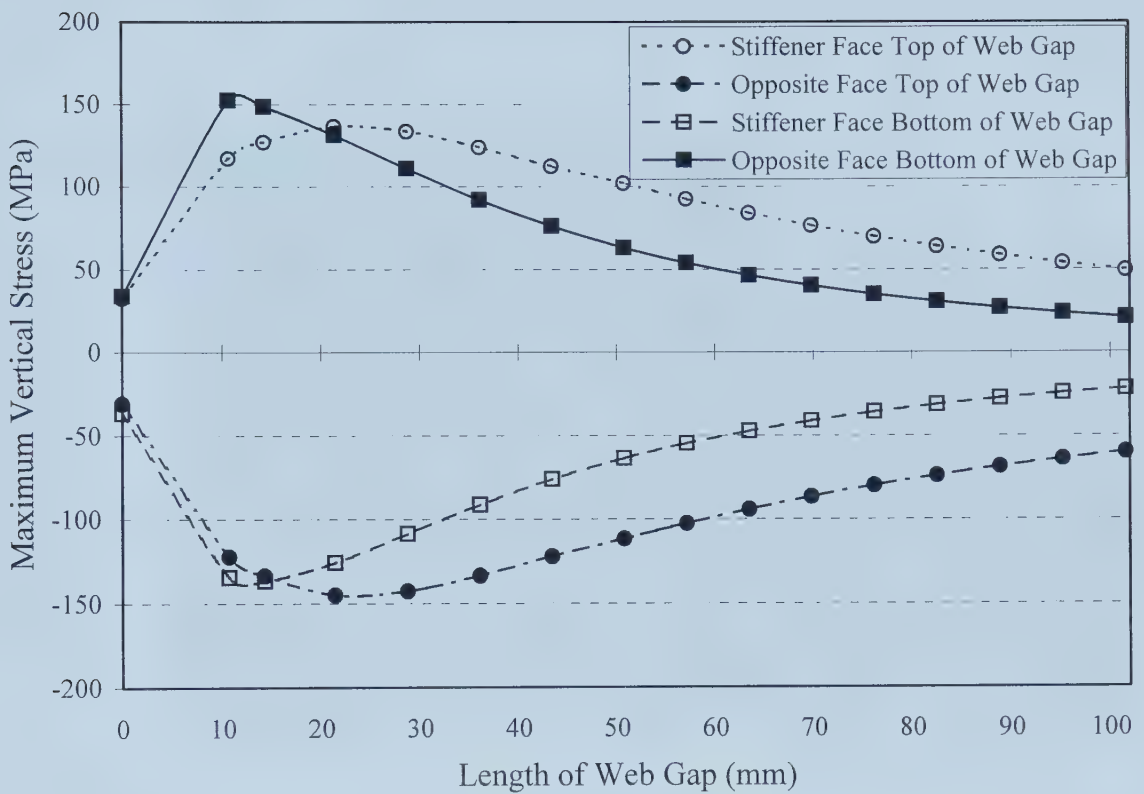
Figure 5–16 Maximum Vertical Stress vs. Web Gap Length
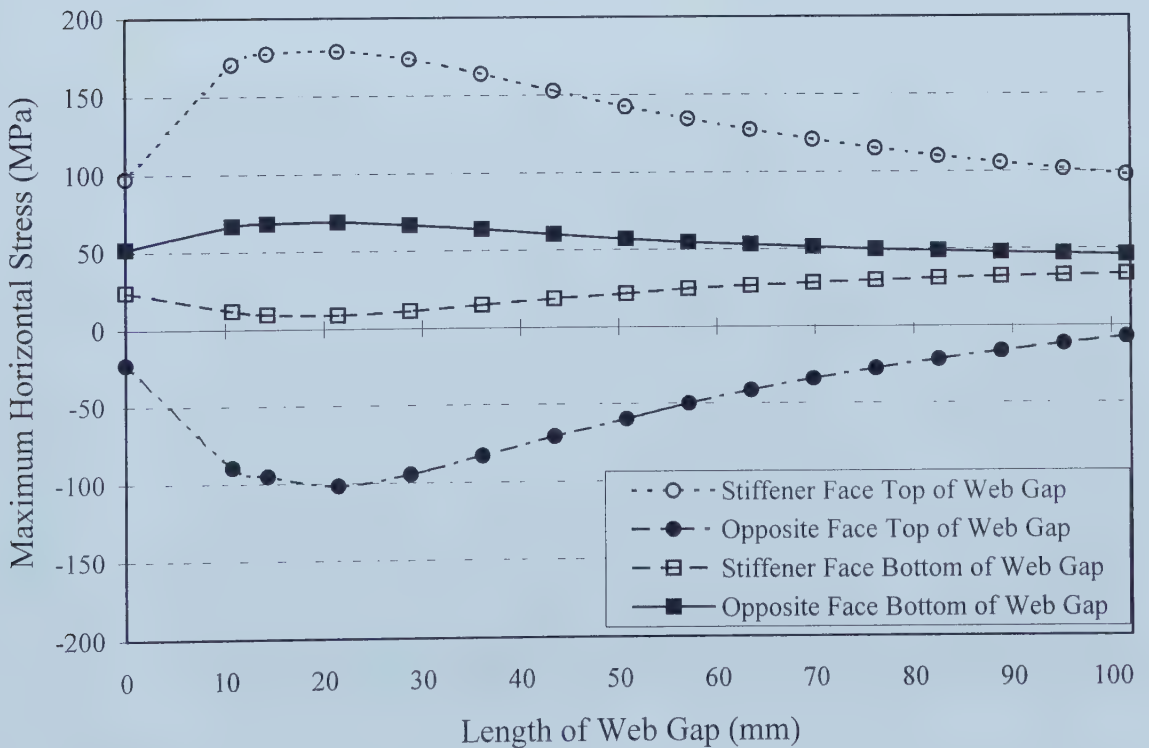
Figure 5–17 Maximum Horizontal Stress vs. Web Gap Length
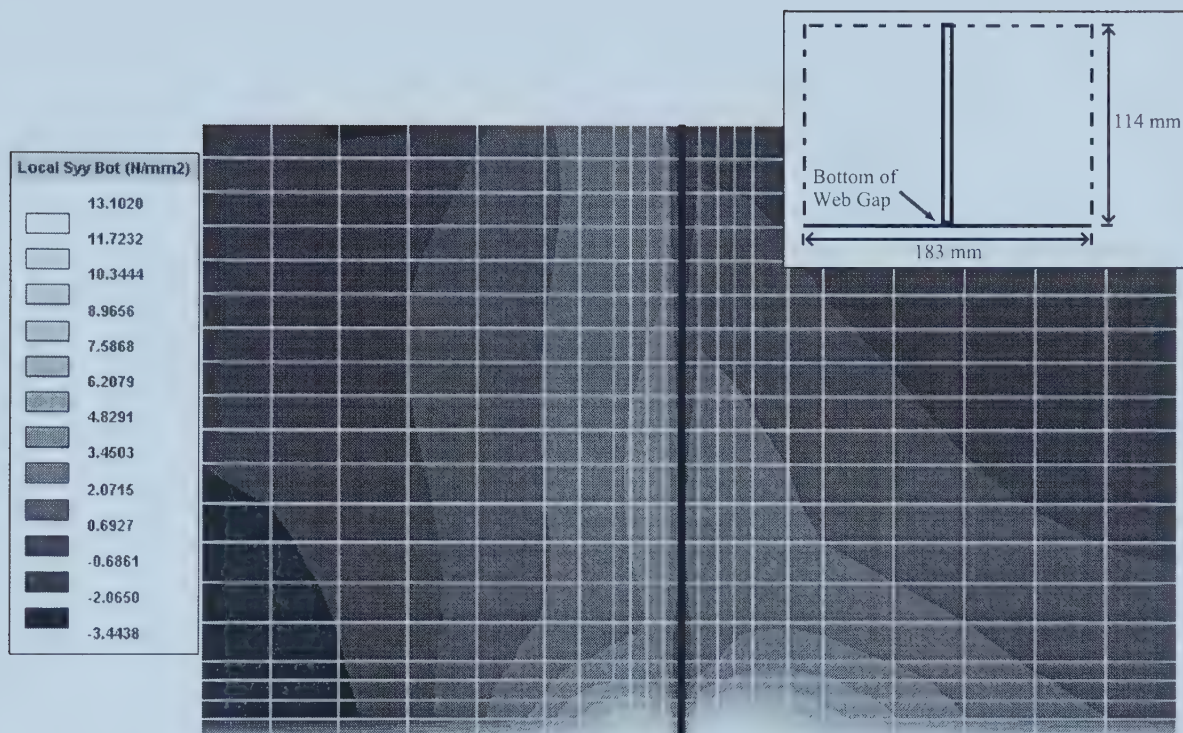
Figure 5–18 Vertical Stresses in Web Gap Region with Stiffener Attached to the Bottom Flange
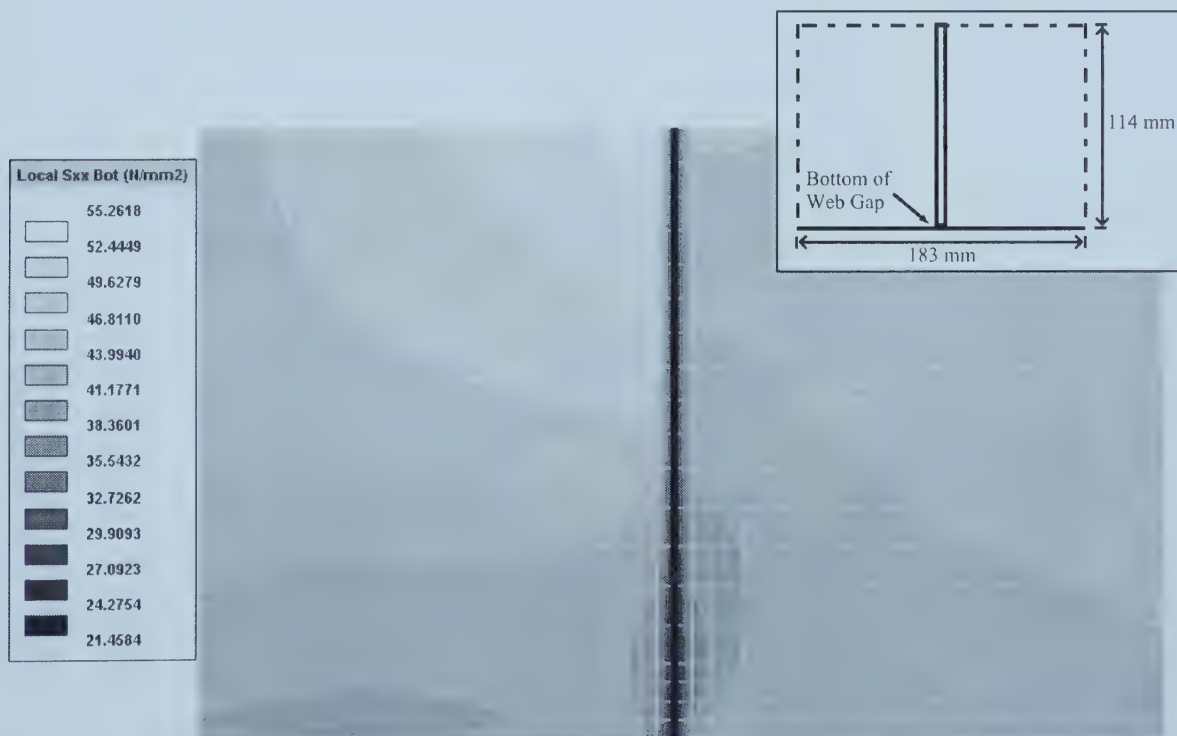
Figure 5–19 Horizontal Stresses in Web Gap Region with Stiffener Attached to the Bottom Flange
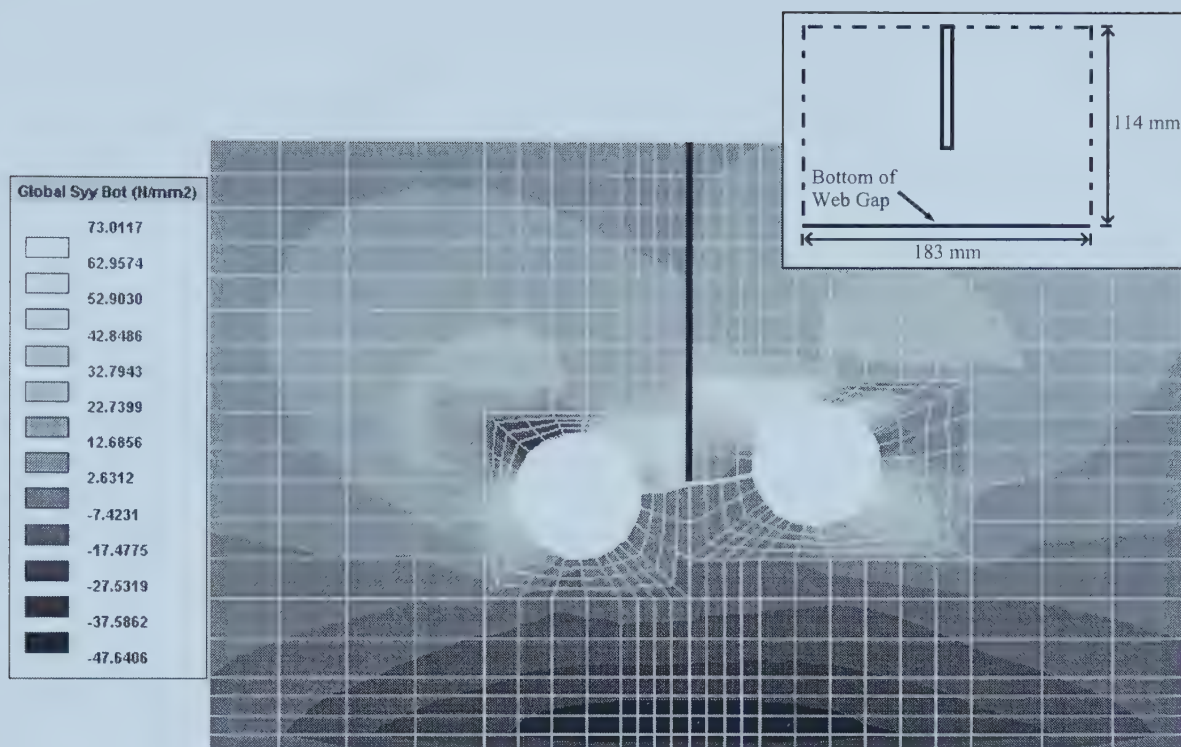
Figure 5–20 Vertical Stresses in Web Gap Region with Stop Holes and Through-Thickness Crack
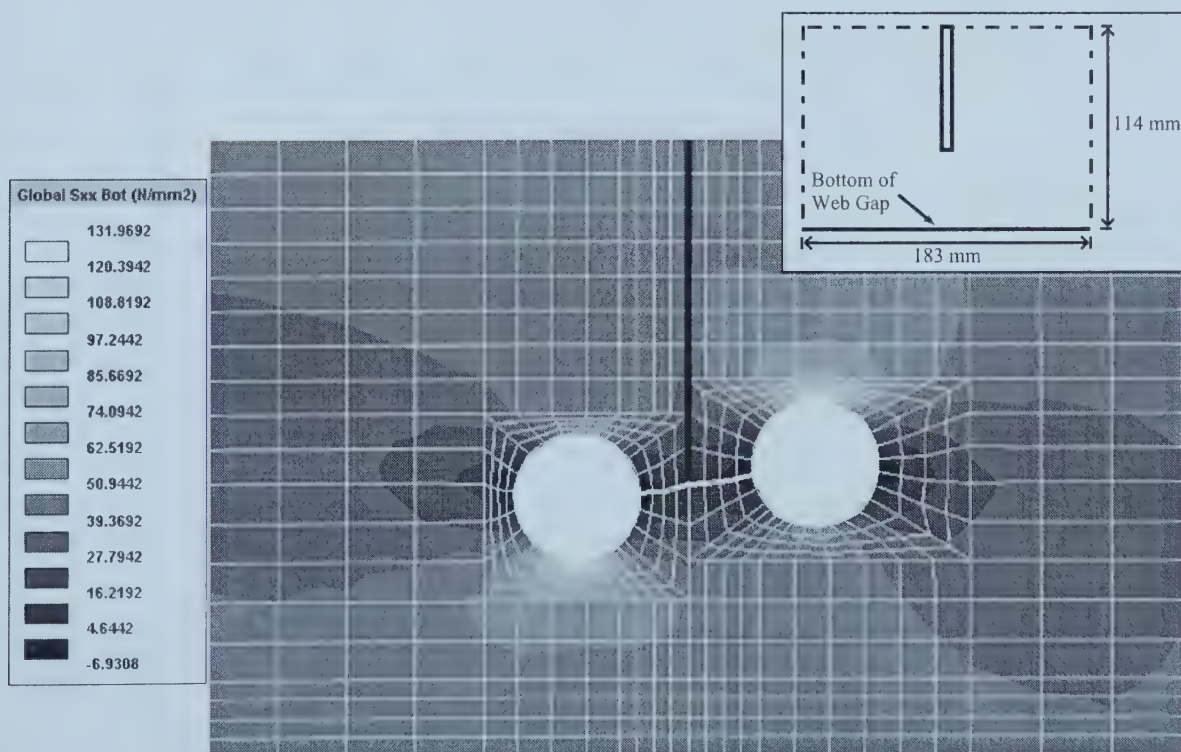
Figure 5–21 Horizontal Stresses in Web Gap Region with Stop Holes and Through-Thickness Crack
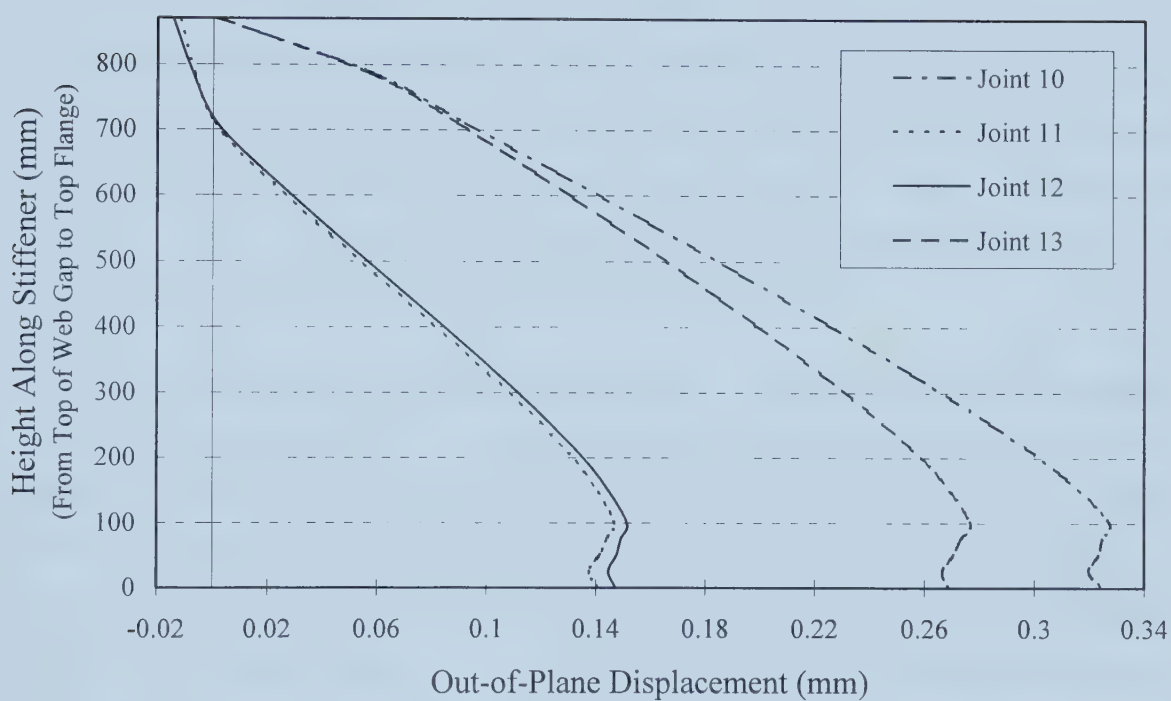
Figure 5–22 Out-of-Plane Displacement of Stiffeners in Test Specimen 3

6. SUMMARY, CONCLUSIONS AND RECOMMENDATIONS

6.1 Summary

The CN Mile 5.09 Edson Subdivision Bridge in Edmonton, Alberta is an example of a multi-girder bridge with distortion-induced fatigue cracking at the connections between the transverse stiffeners and the girder webs. The bridge, built in 1965, consists of two parallel four-span bridges (9.9 m–17.3 m–17.3 m–9.9 m) and each bridge has eight parallel steel girders interconnected by steel diaphragms and a composite concrete deck. Although the diaphragms are perpendicular to the bridge girders, they are staggered across the width of the bridge since the bridge is on a 28° RHF skew. The diaphragms are connected to the girders with transverse stiffeners that are welded to the girder web and top flange, but cut 51 mm short of the bottom tension flange.

After 33 years in service, the bridge was replaced in 1998, mostly because of clearance problems, but also because of the presence of more than 300 distortion-induced fatigue cracks. These cracks were all in the girder webs near the base of the transverse stiffeners. Field tests performed prior to the dismantling of the bridge were used to design the laboratory test setup for the experimental program carried out by Fraser *et al.* (2000) and for the experimental program undertaken in this report. The laboratory tests by Fraser *et al.* (2000) on three of the bridge girders indicated that the remaining fatigue life was approximately 4.2 million cycles for a 35 MPa bottom fibre stress range. The large distortion-induced fatigue cracks, up to 250 mm long, that developed in the three girders remained stable at –50°C and at stresses twice the maximum observed during field testing.

The experimental program presented in this report consisted of fatigue tests on five full-size bridge girders. Four of the tests were conducted to study the behaviour of the distortion-induced fatigue cracks in the web gap regions and to confirm the earlier finding by Fraser *et al.* (2000) concerning the stability of the large fatigue cracks at –50°C. Fatigue testing of the girders was performed at a stress range 40% greater than that observed during field testing, namely a 50 MPa bottom fibre stress range.

Repair angles were used to rehabilitate three of the girders after the fatigue cracks had reached a significant length. The fifth bridge girder tested in this program was repaired with stop holes and gap-bridging angles prior to testing. It was tested at a bottom fibre stress range of 35 MPa in order to assess the effectiveness of two different rehabilitation schemes when fatigue cracks are repaired when first detected.

A finite element model was developed from the results of the experimental program. A finite element analysis was performed to investigate the behaviour of the web gap region, including the effect of changes of the web gap length and the effect of the bottom flange thickness.

6.2 Conclusions

The following conclusions can be drawn from the test program:

1. The tested bridge girders had a remaining fatigue life of 2.6 million cycles at a 50 MPa bottom fibre stress range. This remaining fatigue life is approximately 1.5 million cycles less than the fatigue life observed by Fraser *et al.* (2000) for a bottom fibre stress range of 35 MPa.

2. Static and cyclic tests conducted on girders with large fatigue cracks in the web confirmed that at a temperature of $-50^{\circ}C$ the girders exhibited sufficient fracture toughness to be able to prevent unstable crack propagation even under stresses twice those measured in the field.

3. The ability of the girders to resist and transfer loads even with the presence of the large fatigue cracks in the girder web was confirmed.

4. A combination of Mode I and Mode III loading was responsible for crack initiation past the stop holes. Drilled stop holes were found to be ineffective at arresting distortion-induced fatigue cracks. The stop hole drilling method can only be effective when the distortion of the web gap is prevented.

5. Cracks can initiate at stop holes and propagate downward into the tension flange of the beam. These cracks can eventually lead to failure of the beam.

6. Rehabilitation of steel girders with distortion-induced fatigue cracks can be carried out effectively. In the program reported herein, a combination of an angle bolted to the transverse stiffener and the tension flange and drilled stop holes was effective when relatively small cracks were present. However, this rehabilitation scheme was not effective when large (150 mm) fatigue cracks were present.

7. Rehabilitation of the girders with an angle bolted to the web and to the tension flange was found to be unreliable.

8. It is difficult to locate the tip of distortion-induced fatigue cracks in the field. Therefore, visual inspections alone should not be relied upon to locate the crack tips.

The following conclusions can be drawn from the finite element analysis:

1. Simplified calculations based on a fix-ended beam model tend to overestimate the stresses in the web gap region.

2. The web gap distortion and resulting stresses in the web calculated from measured differential displacements were very conservative. These conservative stresses, combined with the use of a fatigue Category C' stress range versus number of cycles curve yielded very conservative estimates of the fatigue life for the tested specimens.

3. Increasing the web gap length from 51 mm to 102 mm by cutting back the stiffener significantly decreased the maximum stresses in this region. However, for short web gaps (less than 21 mm) an increase in web gap length did not have a significant effect on the web gap stresses. Therefore, improving the web gap detail by cutting back the stiffener should be used with caution.

4. Beam theory may predict less conservative web gap stresses as the stiffener and flange thickness increase. An example of this situation would be bridge girders with composite concrete decks and large transverse stiffeners.

5. The large stresses at the top of the stop holes were consistent with the upward fatigue crack initiation observed in the laboratory tests. Therefore, the equation proposed by Fisher (1980) to determine the size of stop holes should not be used for distortion-induced fatigue cracks. The combined Mode I and Mode III fatigue loading at the edge of the stop holes is not taken into account by the equation.

6.3 Recommendations for Further Research

Based on the experimental program and the numerical analysis presented, recommendations for further research are:

1. Further testing, including field tests, of the rehabilitations utilising repair angles and stop hole drilling should be carried out in order to confirm their effectiveness.

2. The propagation of distortion-induced fatigue cracks downward from the stiffener-to-web junction and into the bottom flange should be investigated further to determine an effective rehabilitation.

3. An investigation of the web gap behaviour and stability of distortion-induced fatigue cracks at low temperatures for materials with low toughness should be carried out.

REFERENCES

AASHTO, (1983). Specifications for highway bridges. Washington, D.C.

AASHTO, (1998). AASHTO LRFD bridge design specifications. Second edition. Washington, D.C.

American Railway Engineering Association (AREA), (1994). Manual for railway engineering. The American Railway Association, Chicago.

ASTM, (1997). ASTM Designation: A 370-97a – Standard test methods and definitions for mechanical testing of steel products. American Society for Testing and Materials, Philadelphia, PA.

Broek, D., (1989). The practical use of fracture mechanics. Kluwer Academic Publishers.

Canadian Standards Association (CSA), (2000). CAN/CSA-S6-00 – Canadian Highway Bridge Design Code. Toronto, Ontario.

Canadian Standards Association (CSA), (1994). CAN/CSA-S16.1-94 – Limit states design of steel structures. Canadian Standards Association, Rexdale, Ontario.

Castiglioni, C.A., Fisher, J.W., and Yen, B.T., (1988). Evaluation of fatigue cracking at cross diaphragms of a multigirder steel bridge. Journal of Constructional Steel Research, Vol. 9, pp. 95–110.

Fisher, J.W., (1978). Fatigue cracking in bridges from out-of-plane displacements. Canadian Journal of Civil Engineering, Vol. 5, No. 4, pp. 542–556.

Fisher, J.W. and Keating, P.B., (1989). Distortion-induced fatigue cracking of bridge details with web gaps. Journal of Constructional Steel Research, Vol. 12, pp. 215–228.

Fisher, J. W., Kulak, G. L., and Smith, I. F., (1998). A fatigue primer for structural engineers. National Steel Bridge Alliance, American Institute of Steel Construction, Chicago, IL.

Fraser, R.E.K., Grondin, G.Y., and Kulak, G.L., (2000). Behaviour of distortion-induced fatigue cracks in bridge girders. Structural Engineering Report, No. 235, Department of Civil and Environmental Engineering, University of Alberta, Edmonton, Alberta.

Gross, T.S., (1985). Frictional effects in Mode III fatigue crack propagation. Scripta Metallurgica, Vol. 19, No. 10, pp. 1185–1188.

Lai, L-Y, (1997). On drilling holes to arrest fatigue crack growth. Building to Last – Proceedings of the Structural Congress XV, Vol. 1, ed. Kempner and Brown. ASCE, New York, pp. 31–35

S-Frame for windows (S-Frame), (1999). Softek Services Limited. Richmond, BC.

Stallings, J.M., Cousins, T.E., and Stafford, T.E., (1999). Removal of diaphragms from three-span steel girder bridge. ASCE Journal of Bridge Engineering, Vol. 4, No. 1, pp. 63–70.

Tedesco, J.W., Stallings, J.M., and Tow, D.R., (1995). Finite element method analysis of bridge girder-diaphragm interaction. International Journal of Computers and Structures, Vol. 56, No. 2/3, pp. 461–473.

Tschegg, E.K. and Stanzl, S.E., (1988). The significance of sliding mode crack closure on Mode III fatigue crack growth. Basic Questions in Fatigue: Volume 1, ed. Fong and Fields. ASTM, Philadelphia, PA, pp. 214–232.

Appendix A

Specimen Behaviour at Significant Crack Length

Appendix A

Tables A–1 through A–5 show the results of the static test performed on specimen 1 at the end of fatigue testing and on specimens 2, 3, and 4 before repair. Figure 3–4 shows the joint locations referred to in these tables.

Table A–1

Specimen Behaviour before Repair

Test Specimen	Load per Actuator (kN)	Neutral Axis Position East Face (mm)	West Face (mm)	Girder End Reactions North (kN)	South (kN)	Midspan Bottom Fibre Stress (MPa)
1	193	817	824	163.8	167.6	63.4
2	188	845	823	167.1	167.9	61.4
3	196	807	808	175.8	178.1	64.0
4	194	827	808	170.9	169.2	61.9

Table A–2

Diaphragm End Support Details and Specimen Displacements
at Completion of Fatigue Testing, Test Specimen 1

(193 kN/actuator)

| Joint* | Length of Diaphragm End Support (mm) | Vertical Displacement (mm) | Differential Displacements | |
			Designation	Displacement (mm)
3	1150	-4.12		
			$\Delta_{9\text{-}3}$	-0.07
9		-4.18		
4	1060	-5.29		
			$\Delta_{11\text{-}4}$	-0.28
11		-5.57		
5	925	-4.36		
			$\Delta_{13\text{-}5}$	-0.13
13		-4.49		
6	855	-1.52		
			$\Delta_{15\text{-}6}$	-0.16
15		-1.68		
8		-2.00		
			$\Delta_{8\text{-}17}$	-0.08
17	870	-1.92		
10		-5.12		
			$\Delta_{10\text{-}18}$	-0.61
18	1115	-4.51		
12		-5.65		
			$\Delta_{12\text{-}19}$	-0.75
19	1060	-4.91		
14		-4.04		
			$\Delta_{14\text{-}20}$	-0.09
20	1160	-3.95		

* Refer to Figure 3–4 for joint location.

Table A–3

Diaphragm End Support Details and Specimen Displacements before Repair, Test Specimen 2

(188 kN/actuator)

Joint*	Length of Diaphragm End Support (mm)	Vertical Displacement (mm)	Differential Displacements	
			Designation	Displacement (mm)
3	1165	-4.00		
			$\Delta_{9\text{-}3}$	-0.07
9		-4.07		
4	1130	-4.79		
			$\Delta_{11\text{-}4}$	-0.58
11		-5.37		
5	992	-3.61		
			$\Delta_{13\text{-}5}$	-0.72
13		-4.32		
6	840	-1.35		
			$\Delta_{15\text{-}6}$	-0.25
15		-1.60		
8		-2.02		
			$\Delta_{8\text{-}17}$	-0.40
17	830	-1.62		
10		-5.04		
			$\Delta_{10\text{-}18}$	-0.81
18	1190	-4.23		
12		-5.57		
			$\Delta_{12\text{-}19}$	-0.21
19	1210	-5.36		
14		-3.94		
			$\Delta_{14\text{-}20}$	0.12
20	1170	-4.06		

* Refer to Figure 3–4 for joint location.

Table A–4

Diaphragm End Support Details and Specimen Displacements
before Repair, Test Specimen 3

(196 kN/actuator)

Joint*	Length of Diaphragm End Support (mm)	Vertical Displacement (mm)	Differential Displacements	
			Designation	Displacement (mm)
3	1420	-3.67		
			Δ_{9-3}	-0.29
9		-3.96		
4	1370	-4.88		
			Δ_{11-4}	-0.53
11		-5.41		
5	1220	-3.61		
			Δ_{13-5}	-0.75
13		-4.36		
6	915	-0.59		
			Δ_{15-6}	-0.99
15		-1.58		
8		-1.78		
			Δ_{8-17}	-0.44
17	945	-1.34		
10		-4.99		
			Δ_{10-18}	-0.50
18	1510	-4.49		
12		-5.30		
			Δ_{12-19}	-0.27
19	1330	-5.03		
14		-3.98		
			Δ_{14-20}	0.17
20	1450	-4.15		

* Refer to Figure 3–4 for joint location.

Table A–5

Diaphragm End Support Details and Specimen Displacements before Repair, Test Specimen 4

(194 kN/actuator)

Joint*	Length of Diaphragm End Support (mm)	Vertical Displacement (mm)	Differential Displacements	
			Designation	Displacement (mm)
3	1420	-3.99		
			Δ_{9-3}	0.15
9		-3.85		
4	1500	-5.26		
			Δ_{11-4}	-0.06
11		-5.31		
5	1215	-3.91		
			Δ_{13-5}	-0.42
13		-4.34		
6	940	-1.34		
			Δ_{15-6}	-0.26
15		-1.60		
8		-1.66		
			Δ_{8-17}	-0.58
17	920	-1.09		
10		-4.84		
			Δ_{10-18}	-0.76
18	1430	-4.08		
12		-5.40		
			Δ_{12-19}	-0.62
19	1335	-4.78		
14		-3.78		
			Δ_{14-20}	-0.08
20	1260	-3.70		

* Refer to Figure 3–4 for joint location.

Appendix B

Non-Significant Crack Growth Curves

Appendix B

Figures B–1 through B–4 show the crack growth curves for all non-significant fatigue cracks observed during each of the first four tests completed during the experimental testing program. Figure 3–4 shows the joint locations referred to in these figures.
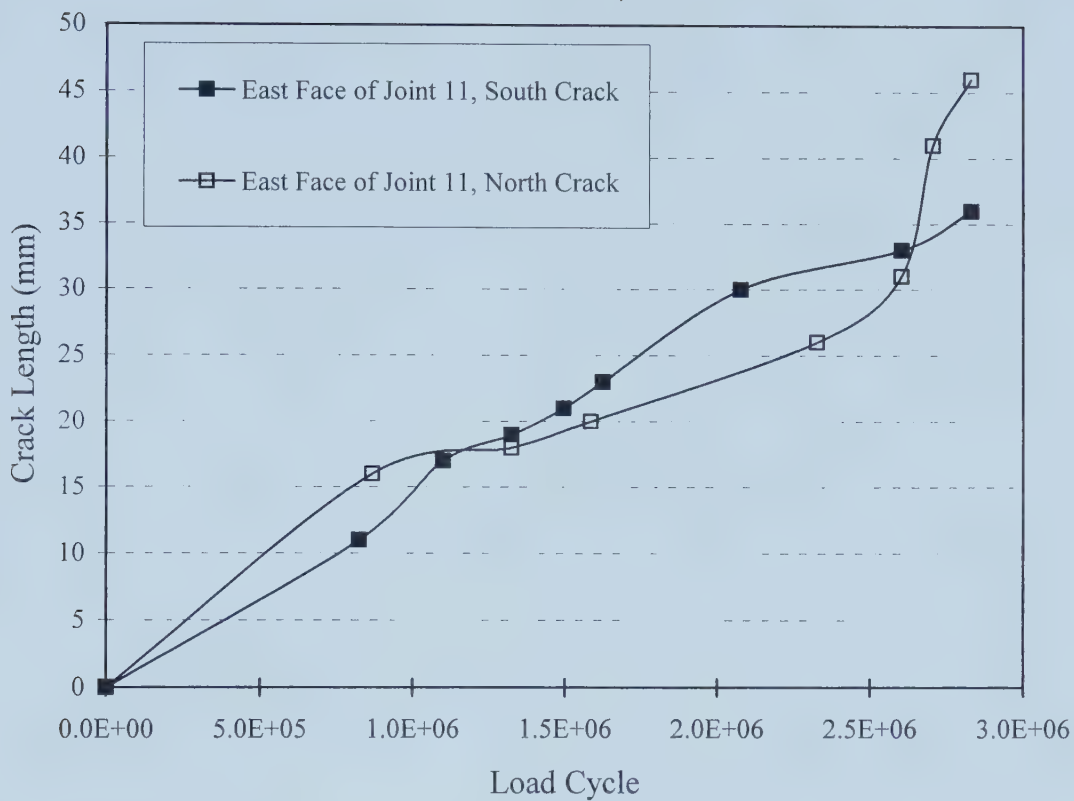
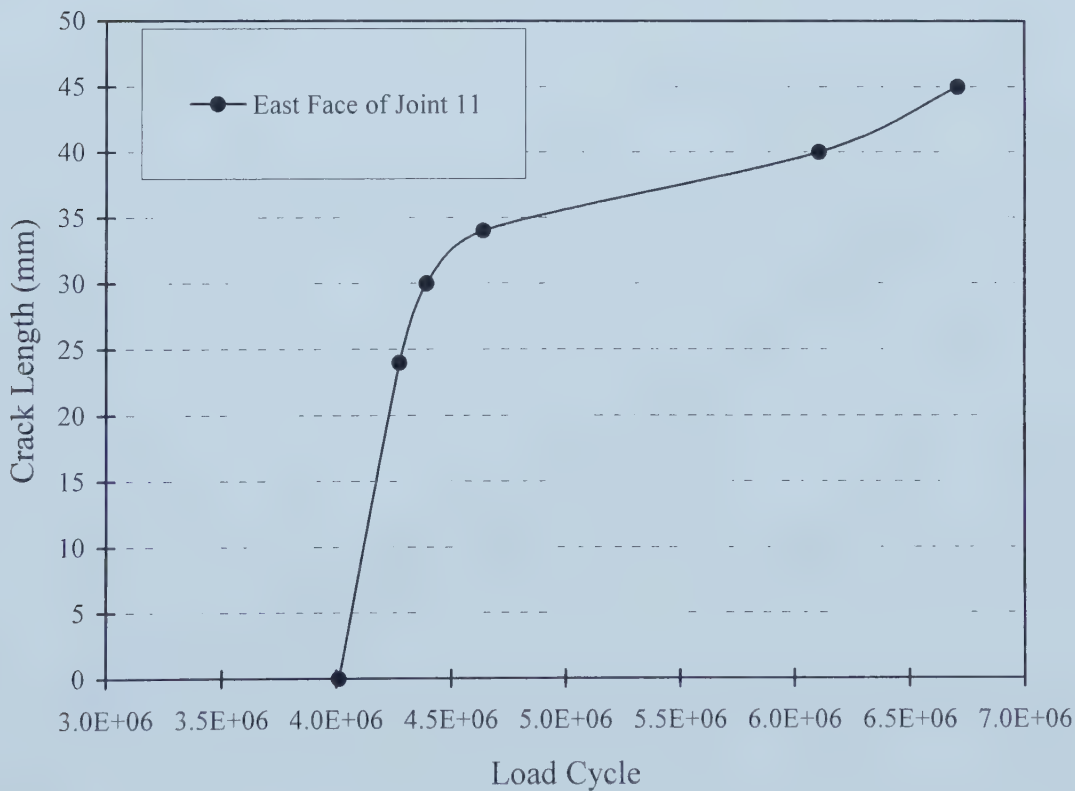**Figure B-1** Non-Significant Crack Length vs. Load Cycle, Specimen 1

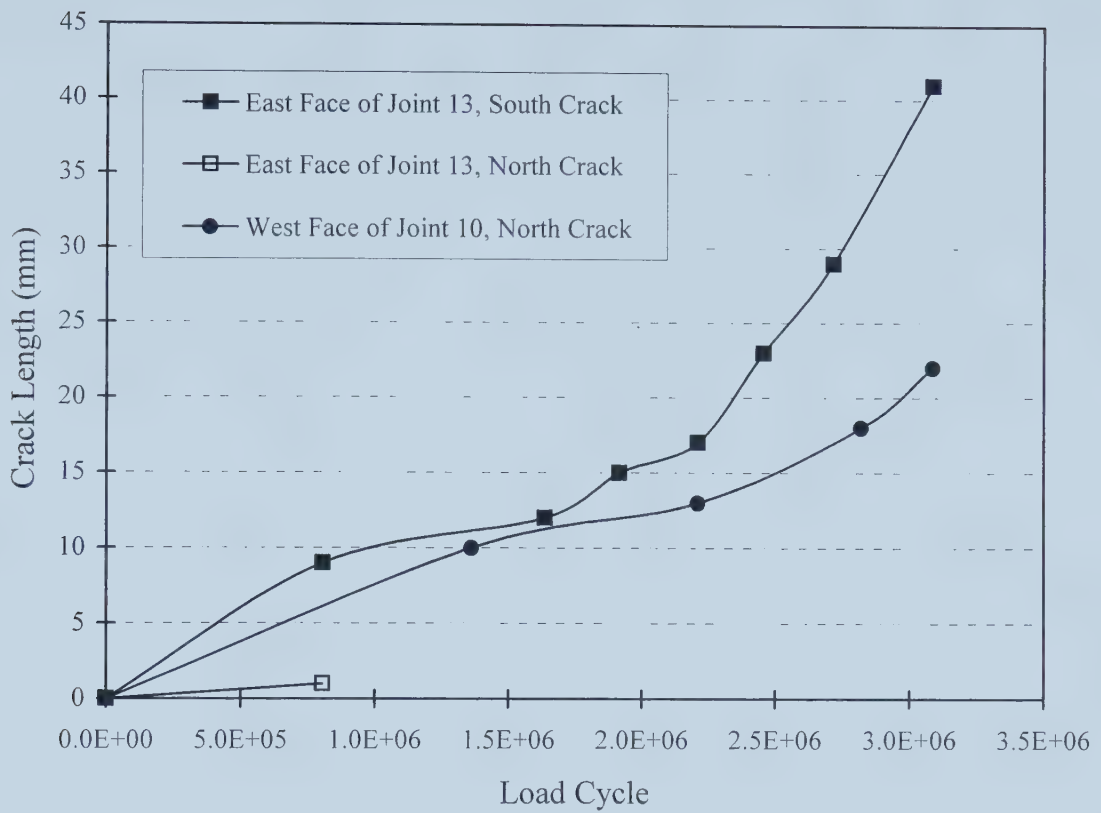**Figure B-2** Non-Significant Crack Length vs. Load Cycle, Specimen 2

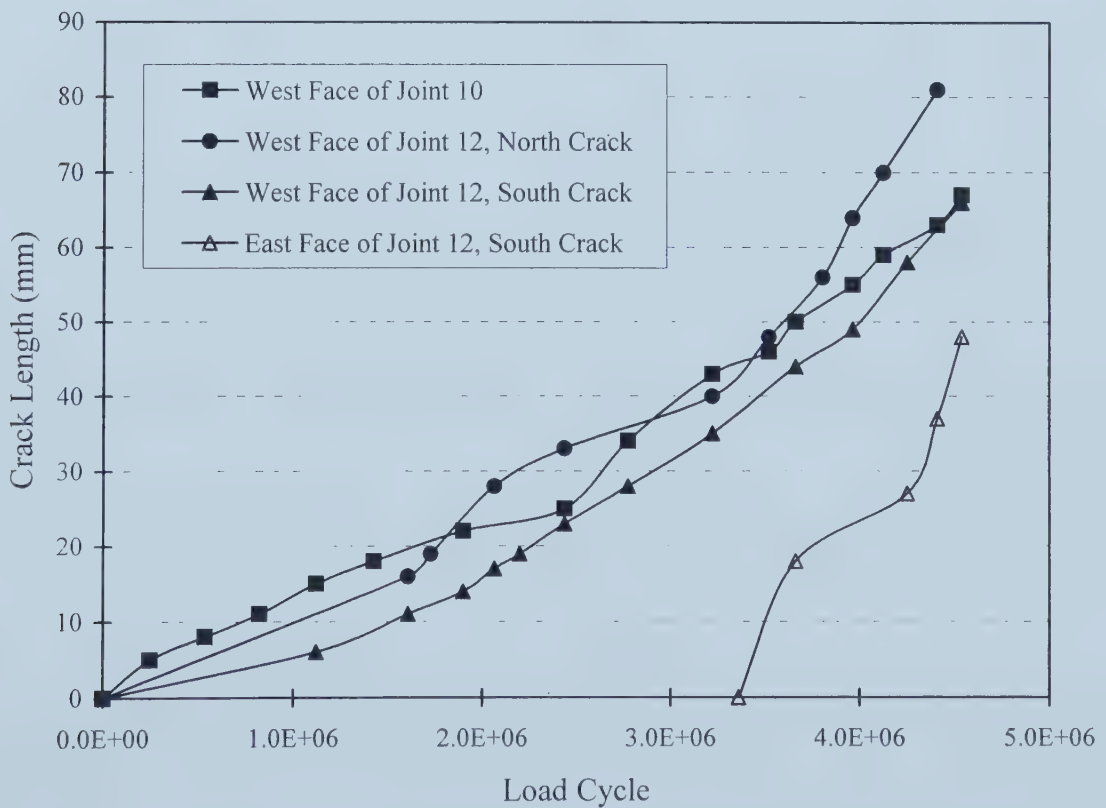**Figure B-3** Non-Significant Crack Length vs. Load Cycle, Test 3

Figure B-4 Non-Significant Crack Length vs. Load Cycle, Specimen 4